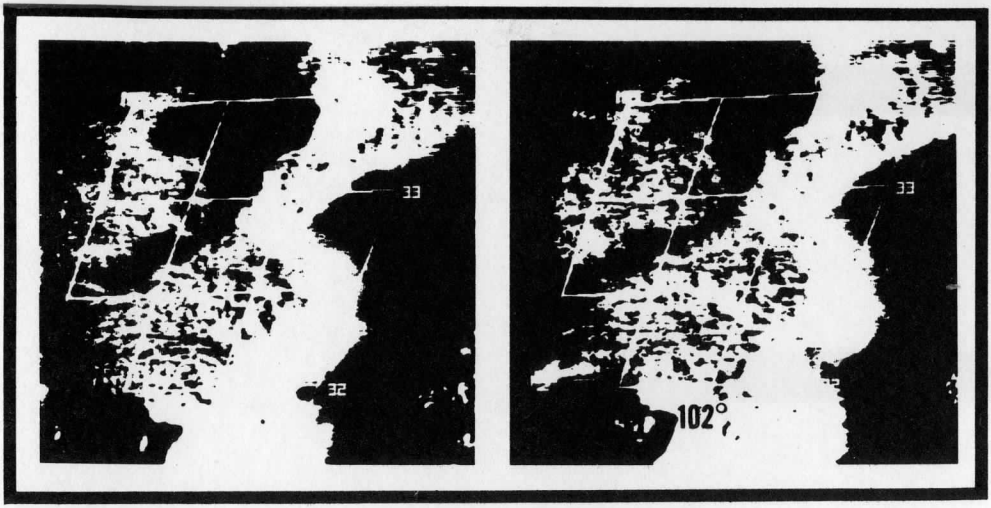

STUDIES OF THE ATMOSPHERE USING AEROSPACE PROBES

Scientific Report on NOAA
Grant 04-6-158-44087, 1978-79
Space Science and Engineering Center
University of Wisconsin - Madison
January 1980

COVER ILLUSTRATION

Gregory Krause, in Chapter III, examines the effects of variations in storm top heights using satellite imagery.

STUDIES OF THE ATMOSPHERE
USING AEROSPACE PROBES

STUDIES OF THE ATMOSPHERE
USING AEROSPACE PROBES
1978-1979

Report, NOAA Grant 04-6-158-44087

The research reported in this document has been supported
by the National Oceanographic and Atmospheric Administration.

January 1980

Published for the
Space Science and Engineering Center
by the
University of Wisconsin Press

Published 1980
The University of Wisconsin Press
114 North Murray Street
Madison, Wisconsin 53715

The University of Wisconsin Press, Ltd.
1 Gower Street
London WCIE, 6HA, England

First Printing

Printed in the United States of America

ISBN 0-299-97062-0

This work is a result of research sponsored by the NOAA National Environmental Satellite Service, Department of Commerce, under Grant No. 04-6-158-44087. The U. S. Government is authorized to produce and distribute reprints for governmental purposes notwithstanding any copyright notation that may appear hereon.

Correspondence concerning editorial matters should be addressed to:

Space Science and Engineering Center
University of Wisconsin
1225 West Dayton Street
Madison, Wisconsin 53706

Orders for copies of this report should be addressed to:

The University of Wisconsin Press

Principal Investigator: Verner E. Suomi
Program Manager: David Suchman

Contributors: Gail Dengel
Gregory Johnson
Gregory Drause
Larry Johnson
Carl Bullock
John A. Young

University of Wisconsin

Studies of the Atmosphere Using Aerospace Probes, 1978-79

Correction to page iv

Contributors: Gail Dengel
Gregory Johnson
Gregory Krause
Larry Johnson
Carl Bullock
John A. Young

CONTENTS

Scanner's note:

This page is blank.

CHAPTER I

A FALSE STEREOGRAPHIC TECHNIQUE FOR SEPARATION OF MULTIPLE CLOUD LAYERS

Gail A. Dengel

ABSTRACT

A technique for producing three dimensional false stereographic displays from simultaneous visible and infrared geostationary satellite images is described and applied to the problem of separating multiple layers of low level clouds. While the apparent heights of the clouds will contain errors, the relative separation between layers results in a more meteorologically sensible picture of the cloud fields.

This improved vertical discrimination combined with the high temporal resolution afforded by the geostationary satellite permits more vertically detailed estimates of wind fields from cloud tracking than could be produced from visible imagery alone. Case study results indicate that wind sets at 50 mb height intervals are possible in regions where suitable cloud fields exist.

I. INTRODUCTION

Satellite images are two dimensional representations of the three dimensional atmosphere. The vertical dimension which is so vital to meteorological studies is at best only implied. In visible images, clouds which exist at varying altitudes are seen projected onto the surface of the earth. This creates considerable confusion regarding the vertical structure. The only height information available comes from the observer's knowledge of different cloud types and the range of heights normally associated with them. Thus, a band of cirrus is recognized as existing at much higher altitudes than a patch of cumulus clouds, even though they may appear adjacent on a satellite picture. While this is adequate for efforts in which only gross separation of cloud layers is needed, it is useless in other endeavors which require a fine distinction between clouds of similar variety at different heights. More information is required.

Satellites equipped with an infrared channel are capable of providing additional height data. Brightness on an IR image is inversely related to temperature, which generally decreases with height. The brighter features are colder and therefore higher in the atmosphere. However, slight variations in temperature are difficult for the eye to detect due to the small contrast between gray shades. A computer can enhance very fine distinctions between digital brightness values to increase the contrast in an image. Efforts have been made to utilize this computer capability, thereby making it possible for the

viewer to detect much more vertical detail than in an image without enhancement. Enhancement may be accomplished in two ways. Black and white enhancement involves increasing the number of gray shades corresponding to a given range of temperatures, thereby improving the contrast. Color enhancement assigns different colors to the various temperature ranges.

Using data from NOAA 2, Pichel et al. (1973) developed a method for incorporating height information from the IR channel into visible channel imagery by producing an artificial stereo display. The IR brightness value is used to assign a height level "h" to each picture element of the visible image. A stereo pair is then generated by shifting each picture element "h" places to the right in the left stereo view and "h" places to the left in the right view. The pair is then viewed through a stereoscope.

A similar false stereo method utilizing geostationary satellite images displayed on a color television monitor will be described in this study. Many new applications are being developed which were not possible with polar orbiting satellites. Since the geostationary platform allows continuous monitoring of a given region, time lapse movies of cloud motions are easily produced (Suomi and Parent, 1964). The three dimensional stereographic capability applied to sequences of geostationary satellite images provides much more vertical and temporal detail and eliminates most of the confusion caused by multiple cloud layers.

The potential of this technique is demonstrated in this study by its application to the cloud tracking process for wind estimation, particularly in severe storm situations.

The difficulty of obtaining sufficiently dense and accurate wind observations has always been a major obstacle to severe weather studies. Over the years, numerous methods have been tested to remedy this deficiency. Balloon ascents are widely used, most notably the synoptic rawinsonde network. To adequately examine the finer scale features contributing to a severe storm, a more detailed view of the storm environment is desired. Specially equipped aircraft have been flown through storm systems taking measurements at various altitudes (Shapiro and Kennedy, 1974). In regions where high storm frequencies have been observed, networks of instrumented towers have been erected which provide increased horizontal and vertical resolution (Izumi and Barad, 1963).

The use of clouds as natural indicators of the wind velocity has long been considered a potentially valuable source of data. The first attempts at estimating wind velocities from cloud drift were made from the surface by observing the sky. More recently, sophisticated methods have been developed to estimate cloud displacements from geostationary satellite platforms (Hubert and Whitney, 1971; Suchman et al., 1975). From a sequence of images, the positions and displacements of cloud targets are measured and the cloud velocities computed.

Rawinsonde reports, while generally taken to be reliable sources of wind information, are often too infrequent and too far apart spatially to resolve

many important features of the atmospheric structure occurring at subsynoptic and smaller scales. For example, a southerly low level jet responsible for the influx of warm, moist air from the Gulf of Mexico into a developing storm system is often poorly resolved by the rawinsonde information. Thus, an important destabilizing factor may not be identified (Raymond, 1977). Upper tropospheric jets (Whitney, 1977; McNulty, 1978) and coupled systems of upper and lower jets (Uccellini, 1977) have also been cited as important factors in severe storm development. These are just a few examples illustrating the need for detailed wind information.

Wind sets derived from the apparent motion of clouds on sequences of satellite images are frequently valuable in filling in the gaps between rawinsonde stations. The density of wind vectors obtained in this manner is dependent upon the number and distribution of cloud targets but in almost all cases improves upon the coverage provided by the rawinsonde network. Two primary difficulties must be faced, however, in applying data obtained in this manner. The first is due to the nature of cloud formation which often results in clustered targets and intervening clear regions. Interpolation between the resulting groups of wind vectors can lead to spatial aliasing. The second difficulty lies in properly assigning heights to cloud motion vectors. Vertical positioning is dependent upon the accurate determination of the heights of the target clouds. Regardless of the accuracy of velocity measurement, improper placement in the vertical results in misleading data which may be more detrimental than having no satellite derived data.

Another serious concern in the use of satellite wind information involves the depth of layers through which clouds may be tracked and the resulting vectors analyzed as a single level. In most studies to date, the winds produced by cloud tracking have been separated into three levels (Mosher, 1975). The low level wind set usually consists of all vectors derived from cumulus type tracers which have cloud top heights ranging from about 900 to 700 mb. When mid-level clouds are available and suitable for tracking a second level of winds may be produced with heights from 600 to 400 mb. The high level wind set is derived from the motion of cirrus clouds and extends from 300 to 100 mb.

This study will demonstrate the necessity in subsynoptic scale investigations for improved height discrimination, particularly in severe storm situations where strong vertical shear is often present. In such cases, wind speed and direction change too rapidly with height to allow vectors representing a layer 200 or 300 mb thick to be analyzed as if at a single level. Application of the false stereographic technique to facilitate rapid separation of multiple cloud layers will be demonstrated and suggested as an aid to the operator in selecting targets during the cloud tracking procedure.

In Section II some applications of satellite derived wind fields to severe weather research are discussed. The advantages and disadvantages inherent in this type of data set are explored, and the need for improved vertical resolution is highlighted. Section III describes W. Bryson's (1978) stereo technique for cloud height measurement and the less precise, but more easily implemented,

false stereo technique which provides the basis for this study. The results of a case study in which wind sets were produced with and without the benefit of the increased height discrimination are given in Section IV. Conclusions drawn from this study along with suggestions for further research are discussed in Section V.

II. DETERMINATION OF SATELLITE WIND FIELDS AND APPLICATIONS TO SEVERE WEATHER RESEARCH

Cloud tracking from a sequence of satellite images has become increasingly an important means of estimating wind fields in regions where conventional data is sparse or nonexistent. This technique has evolved over the past decade from using preliminary cumbersome procedures employing time-lapse movie loops (Hubert and Whitney, 1971) to the elaborate electronic display and computational capabilities of the McIDAS facility at the UW Space Science and Engineering Center (Smith and Phillips, 1973; Smith, 1975; Chatters and Suomi, 1975).

The great potential of satellite wind fields lies in the improvement over conventional data sources in both temporal and spatial resolution. Radiosonde wind information is normally available at 12 hour intervals, which is too infrequent to describe the development of many interesting meteorological phenomena, particularly those occuring at subsynoptic scales. Images from the geostationary satellites, on the other hand, are generally transmitted at 30 minute intervals, and when warranted by interesting or unusual weather conditions, may be recorded at 15, 5 or 3 minute intervals. Spatial resolution in the horizontal is determined by the distribution of clouds, but usually the density of wind vectors in the region of interest can be increased many times over conventional data.

Vertical resolution of satellite wind data has presented a greater problem. In order to properly locate a cloud tracer wind in the vertical the height of the target cloud must be known. Many methods have been explored to estimate cloud heights on satellite imagery. That which is currently used by the automated cloud tracking program at SSEC uses visible and infrared data and climatological soundings to estimate cloud thickness and height (Mosher, 1974).

Regardless of its accuracy, a wind vector is useless and potentially detrimental to subsequent analyses if improperly located in altitude. This problem is particularly acute where vertical shear is most pronounced, as in the vicinity of jets and severe storm systems. For example, consider a case where the wind veers strongly with height. A wind vector which is incorrectly included with a set of winds from some higher level will produce a fictitious pattern of convergence and divergence as illustrated in Figure I.1 where the misplaced vector is indicated by an "x". This can lead to erroneous conclusions concerning future development or dissipation of thunderstorms over this area. Occasionally, as in the case study presented in Section IV, wind speed and direction may change with height rapidly enough to cause significant errors if all clouds in a 100 mb layer are analyzed at the same level.

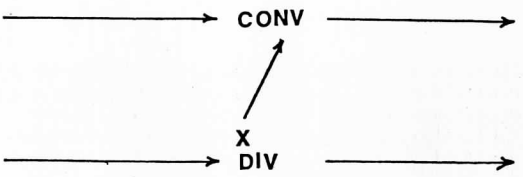

Figure I.1. Erroneous pattern of convergence and divergence caused by incorporating vector "x" into a higher level wind set.

Many applications for satellite derived wind sets exist in the field of severe weather research. Tracking of cumulus clouds prior to storm development may provide insight into the processes of low level heat and moisture transportation and the locations of low level jets. A study by Maddox et al. (1977) demonstrated the use of a satellite-derived low level wind set in estimating moisture convergence. The results show that subsequent severe storm development occurred within the regions of highest moisture convergence.

A correlation between the locations of low level southerly jets and severe storm occurrence has long been known to exist (Raymond, 1977). Unfortunately, the density of conventional wind observations is often insufficient to detect or accurately locate low wind maxima. When a field of cumulus clouds exists over the appropriate area, cloud tracking can fill the data gap and define not only the spatial extent but also the maximum speed of the low level jet.

Attempts have been made to objectively compute fields of vorticity and divergence from low level wind sets (Houghton and Lee, 1977; Peslen, 1977). Extreme caution is advised in such analyses. The del-operator is strictly horizontal and therefore makes no allowances for vertical variation of the wind. It is desirable that the wind sets to which it is applied include only vectors from atmospheric layers which are sufficiently thin to render vertical variations of wind speed and direction negligible.

High level wind sets are also very valuable in the study of severe storms. The locations and intensities of upper level jet streaks are important factors in the development of severe weather. The diffluent region between polar and subtropical jet streams has long been recognized as a preferred region for squall line development (Whitney, 1977; Purdom, 1971). The characteristic cirrus shield associated with jet streams generally provides ample targets for cloud tracking (Anderson et al., 1974). Whitney has shown through a series of five case studies the apparent role of the subtropical jet in providing an environment which is favorable for severe storm development. This was largely unknown before the availability of satellite imagery due to the sparseness of radiosonde data over northern Mexico. It may not always be possible to ascertain the maximum core speed of the jet through cirrus tracking, however, as a clear region frequently exists along the northern flank of the jet. Some other means is required to obtain wind speeds in this area.

In any analysis of satellite winds the possibility of spatial aliasing due to gaps in the wind field must be recognized. Cloud-free regions are often present where targets are not available. Gaps may also be produced in low level wind sets by overlying high clouds which obliterate lower targets from the operator's field of view. Proper selection of analysis techniques may help reduce this problem, although it is advisable in general to avoid drawing inferences from any region where the density of wind information is low.

III. THE USE OF STEREOGRAPHIC DISPLAYS IN SEPARATING CLOUD LAYERS

W. Bryson (1978) has investigated the use of nearly simultaneous images from two geostationary satellites in determining cloud heights. A stereo effect is produced through the superpositioning of the two images on a color television monitor by driving the red gun of the monitor with the data from one satellite and the green gun with the data from the second satellite remapped to the projection of the first. The resulting composite image is then viewed through glasses having one red filter and one green filter. The eye looking through the red filter is presented with the image as "seen" by that satellite which produced the data used to drive the red gun. Similarly, the eye looking through the green filter views the scene from the perspective of the second satellite. Just as normal depth perception results from the mind's superpositioning of images produced by two sensors, the eyes, separated by a distance of a few centimeters, a three dimensional image is created by the mind's interpretation of the superimposed images from two satellites separated by 60°longitude. In other words, a mental analogy is drawn between the two sets of imaging devices, a pair of eyes and a pair of satellites.

Bryson showed that this technique can be used effectively to separate high, middle and low level clouds from each other and from surface features. Unfortunately, the simultaneous images required for its implementation are currently available on an infrequent basis. In addition, only the region of overlap between the areas scanned by the two satellites may be subjected to such analysis.

The false stereo approach taken in this study was conceived and developed by J.T. Young and Frederick Mosher of the University of Wisconsin-Madison Space Science and Engineering Center. While much less accurate in actual determination of cloud heights, it requires only one set of visible and IR data from one satellite at one time to produce a three dimensional image.

To produce a false stereo display for a given time and location, visible and infrared areas of equal dimensions and resolution must be available for pixel by pixel height assignment. Assuming the clouds are opaque, and hence have emissivities equal to one, the temperature at the cloud top is computed from the infrared brightness. The conversion from temperature to height is accomplished by referring to a standard atmosphere sounding of temperature vs. height, corrected for latitude and date.

Having a height estimate assigned to each pixel in this manner, a new image is then constructed to take the place of the second satellite in the stereo view. To form the new image, each pixel in the original visible area is shifted by an amount determined by the height to which it was assigned. The

higher the cloud, the greater the shift will be. In Figure I.2, A is the satellite which provided the original visible and IR data. A' is an imaginary satellite which would produce an image similar to that constructed by the false stereo program. Both A and A' "see" point S on the earth's surface at the same location, hence no shift. From the perspective of A, the low cloud L appears to be located at point A_L, and the high cloud H at point A_H. From the platform of the imaginary satellite A', the location of L is shifted by a distance x_1, and the location of H by a distance x_2 which is greater than x_1. It can be seen that from zero shift at the surface the amount of shift increases in a manner which is approximately proportional to the height of the cloud.

In a manner totally analogous to the real stereo display used by Bryson, the false stereo picture is displayed on a color television monitor with the original visible data driving the red gun and the shifted data driving the green gun. Viewed through the red and green glasses, a three dimensional image results.

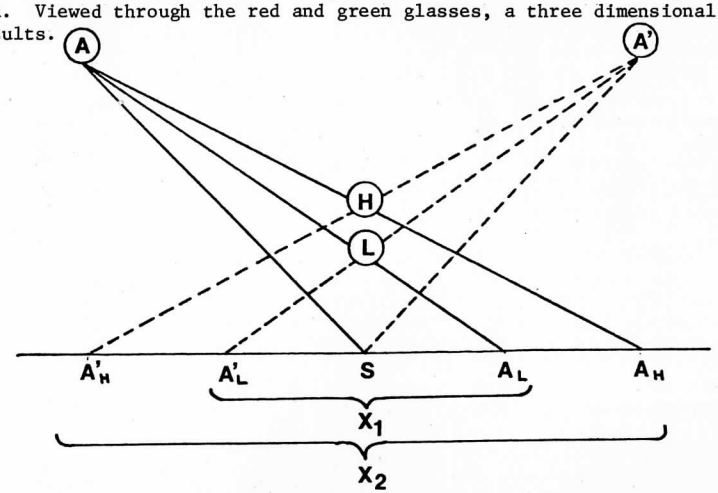

Figure I.2. The effect of altitude in determining the apparent shift in location of a cloud.

While false stereo has the advantage of greatly increased availability and ease of processing, it has several deficiencies. Unlike true stereo, the image constructed for the second satellite cannot see under the clouds which leaves small gaps in the picture. These gaps can be smoothed by an averaging process to make the resulting picture more visually pleasing, but missing data cannot be recovered.

The quality of the false stereo image is also dependent upon the accuracy of the height estimates. Two basic assumptions in the cloud height algorithm may result in inaccuracies under certain circumstances. First, the assumption that the actual vertical temperature profile resembles the climatological sounding may be violated causing errors in the assigned heights of 100 mb or

more (Hinton, 1977). Secondly, the blackbody assumption used in estimating temperature is generally good for cumulus type clouds but is less valid for cirrus which may have emissivities substantially below unity. For this reason, false stereo can be applied most effectively to fields of low and middle level clouds.

The principle utility of this technique lies in the ease and rapidity with which multiple layers of low level clouds can be separated at the time of the actual tracking. While no additional information is added to the original data, that which exists is put into a form easier to assimilate psychologically. In previous studies (Houghton and Wilson, 1975; Houghton and Lee, 1977) wind sets generated by cloud tracking were later divided into layers after estimating the height of each vector by comparing cloud top temperatures from the satellite data with local radiosonde reports. False stereo, while having the disadvantage of using climatological soundings rather than current local radiosonde data, permits immediate separation of layers during cloud tracking merely by looking at the three dimensional display without referring back to a supplementary data set. In addition, the stereographic display makes it easier for the operator to select targets which will produce a more uniform field of vectors at each level. In the interests of speed and efficiency, the cloud height program may be invoked to estimate the heights of several representative clouds at each level, and manual height assignment may then be used during the remainder of the cloud tracking process. In this way, detailed separation of low level cloud layers is no longer restricted to research applications, but becomes available even to real time investigations.

In summary, the use of false stereo allows the operator to separate the cloud fields in the vertical much more readily. The actual height separation will have errors depending on the emissivities of the clouds and the temperature soundings used. Even so, the use of the technique allows the operator to see "meteorologically sensible" cloud fields.

IV. DISCUSSION OF CASE STUDY: 20 MAY 1977

The false stereographic technique described in Section III can be used in conjunction with the McIDAS cloud tracking capability to produce wind fields having more vertical detail than was previously possible without time-consuming comparison with conventional soundings. A case study was undertaken to illustrate the effect of this improved height discrimination on a low level wind set.

The case of 20 May 1977 was selected for this purpose. An area of severe thunderstorms developed throughout Oklahoma and northern Texas in advance of a cold front extending northeastward from a weak low pressure center in New Mexico. Figure I.3 shows surface conditions at 12Z.

East of the thunderstorm activity a southerly low level jet provided moisture from the Gulf of Mexico for the advancing storm system. In Figure I.4,

the position of the 850 mb wind maximum is shown along with the region of surface dewpoints greater than or equal to 18°C. From this abundance of moisture at low levels along with strong surface heating during the day (Figure I.5) a multitude of cumulus clouds developed by 18Z. These clouds were the targets used in producing wind sets for analysis in the following case study.

The case of 20 May 1977 is well suited to this kind of analysis because of the extraordinary quantity of data, both satellite and conventional, which is available. It was one of about a dozen days during the spring and summer of that year on which special observations were taken including GOES images at 3 minute intervals and 18Z rawinsondes over the areas where interesting weather was expected to develop (Kreitzberg, 1977).

The increased frequency of satellite images greatly facilitated the process of obtaining a low level wind set. The majority of the target clouds were of the small cumulus variety having life spans of 30 minutes or less. At the normal mode of operation the satellite would transmit an image every half hour, thereby rendering it impossible to identify an individual cloud on more than one or two pictures. For the purpose of quality control it is desirable to use a sequence of three or more images for cloud tracking. In cases where rapid scan data are available the interval between successive images can be decreased sufficiently to make these clouds valid targets.

For this case study a sequence of three images at 6 minute intervals centered around 18Z was chosen. The area covered extended from 30° to 36°N latitude and 90° to 103°W longitude. This time period and location were selected so as to coincide with the special 18Z rawinsonde observations for the purpose of comparison. Of the 17 stations participating in the 18Z ascent, 7 lie within this region (Figure I.6).

The first wind set was produced in the usual manner allowing the computer to assign heights automatically to each vector (Mosher, 1974). After elimination of those vectors, which the quality controls had flagged as erroneous, the wind set consisted of 250 averaged vector pairs, all assigned to a height of 900 mb (Figure I.7). False stereo images were then produced from the satellite data for the same three time periods and a sequence of four wind sets at 50 mb height increments from 900 to 750 mb were produced by the method described in Section III (Figures I.8 - I.11). After deletion of flagged vectors, the 900 mb data set consisted of 78 vector pairs, the 850 mb set of 102 pairs and the 800 mb set of 31 pairs. Above 800 mb it became difficult to separate cloud layers because the region in which many of the targets existed was veiled by overlying cirrus. The fourth wind set, labelled 750 - 700 mb, contains 58 vector pairs from this region and is probably a mixture of several levels above 800 mb.

Looking individually at the three types of wind data (rawinsonde, low level satellite winds assigned to a common height of 900 mb and satellite winds separated into layers through the use of false stereo displays), large variations in quantity and quality are evident.

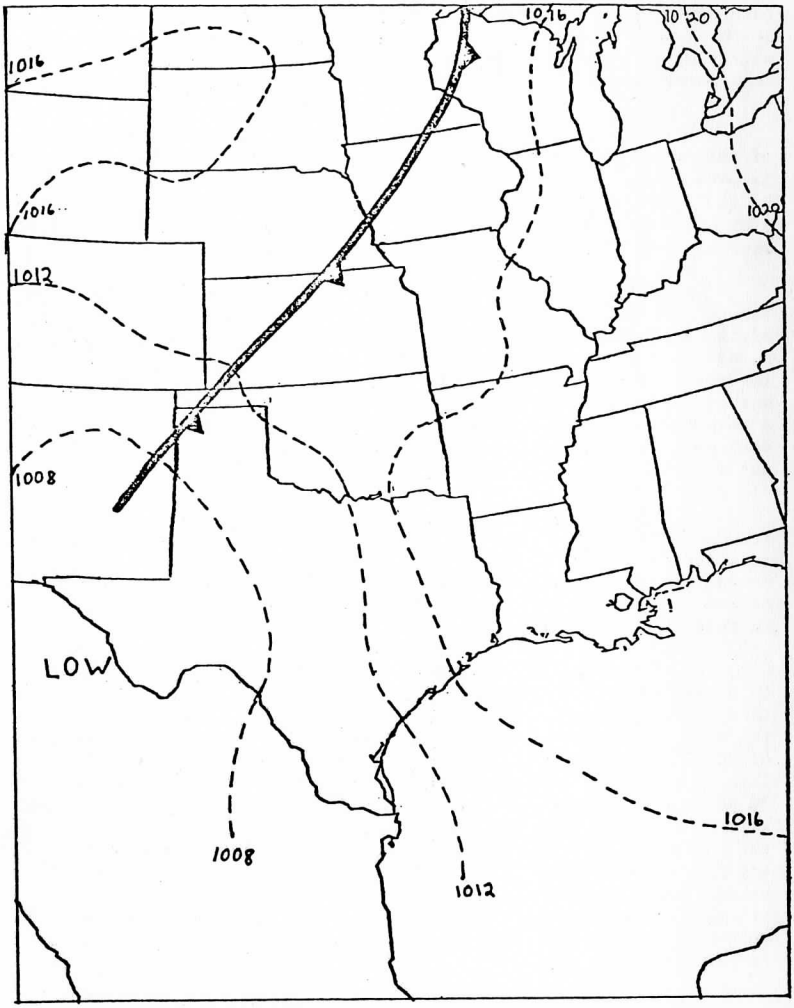

Figure I.3. Surface pressure and frontal systems. 12GMT, 20 May 1977.

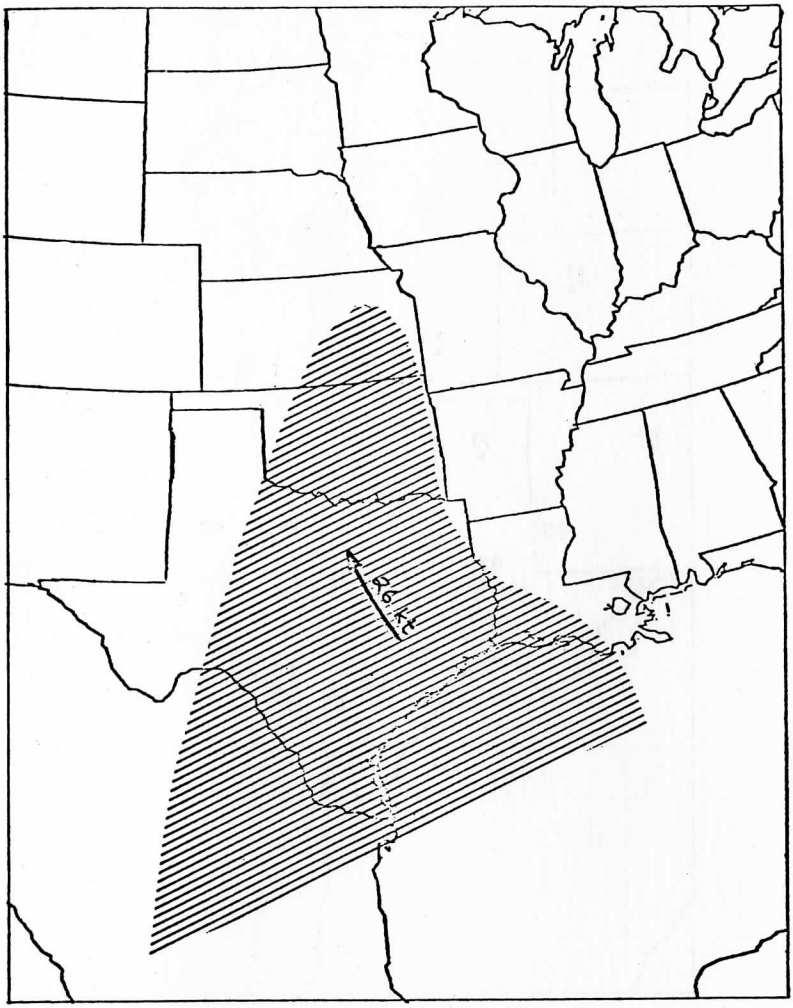

Figure I.4. Low level moisture and 850 mb wind maximum. 12GMT, 20 May 1977. Shaded area indicates surface dewpoints $\geq$ 18°C.

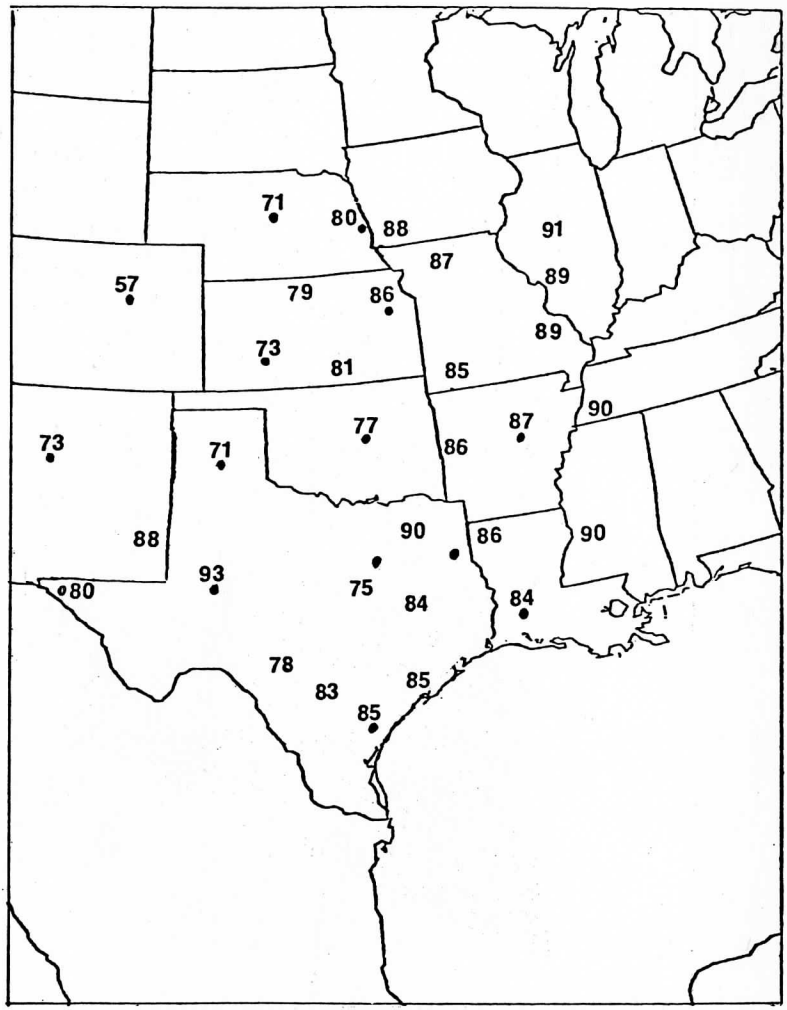

Figure I.5. Maximum temperatures. 20 May 1977.

The conventional data set provides excellent detail in the vertical over the stations from which rawinsondes were launched. However, only 7 stations were located in the region of interest resulting in poor horizontal resolution. Figures I.12 - I.16 are plots of the winds at 900, 850, 800, 750 and 700 mb as given by the 18Z rawinsonde report.

The satellite wind field generated in the usual way using automatic cloud height assignment gives very dense coverage in the horizontal, but vertical discrimination is virtually lost. All of the vectors were placed at the 900 mb level (Figure I.7).

The four wind sets produced with the additional benefit of the false stereo displays exhibit some characteristics of both preceding data sets. Horizontal coverage is greatly improved over that afforded by the rawinsonde network although slightly less dense at any given level than a standard satellite low level wind field. Some information in the vertical is provided by having four layers of low level winds at 50 mb intervals instead of one composite low level field. While the vertical detail is not as great as that provided by a rawinsonde, many important features of the profiles are represented. In particular, since cumulus cloud formation requires moisture and rising motion, the altitudes at which these clouds are located can be taken as indicators of moist regions. Cloud top heights are generally correlated with increased stability and inversions.

A comparison between the 18Z rawinsonde observations and the satellite wind fields for the same time period suggests that the four levels defined with the aid of the false stereo display are reasonable. Figures I.17 - I.19 are plots of the 18Z soundings for SEP, GGG and LCH (see Figure I.6 for locations) which, of the 7 stations lying within the area under consideration, are near enough to the clusters of wind vectors to make direct comparison feasible.

The SEP sounding exhibits considerable moisture throughout a deep layer from the surface to a strong inversion at about 750 mb. The lapse rate is nearly adiabatic up to about 910 mb where the stability increases slightly. Additional increases in stability occur at approximately 850 and 810 mb. It may therefore be expected that clouds, and hence wind vectors, were measured at all four levels. This is borne out by Figures I.8 - I.11. Table I.1 lists the wind direction and speed at each of the four levels which would be expected from inspection of the sounding along with the values measured by cloud tracking. The correspondence between expected and observed winds at all levels is excellent in both speed and direction.

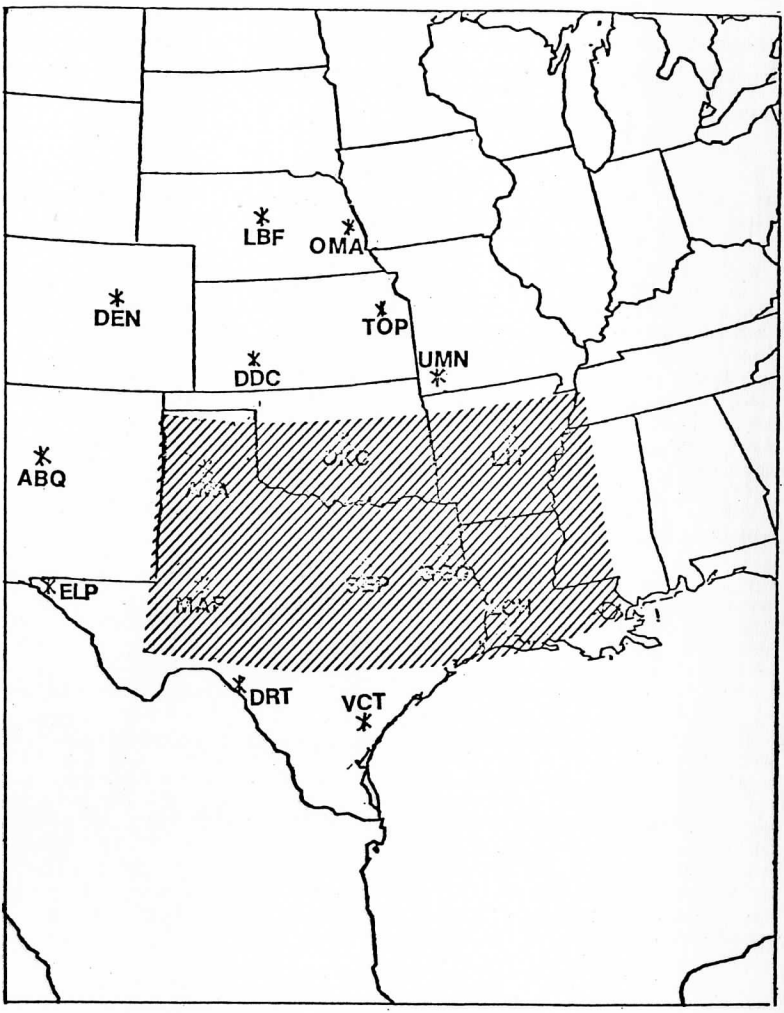

Figure I.6. Locations of 18Z rawinsondes. 20 May 1977. Shaded region indicates area covered by satellite wind fields.

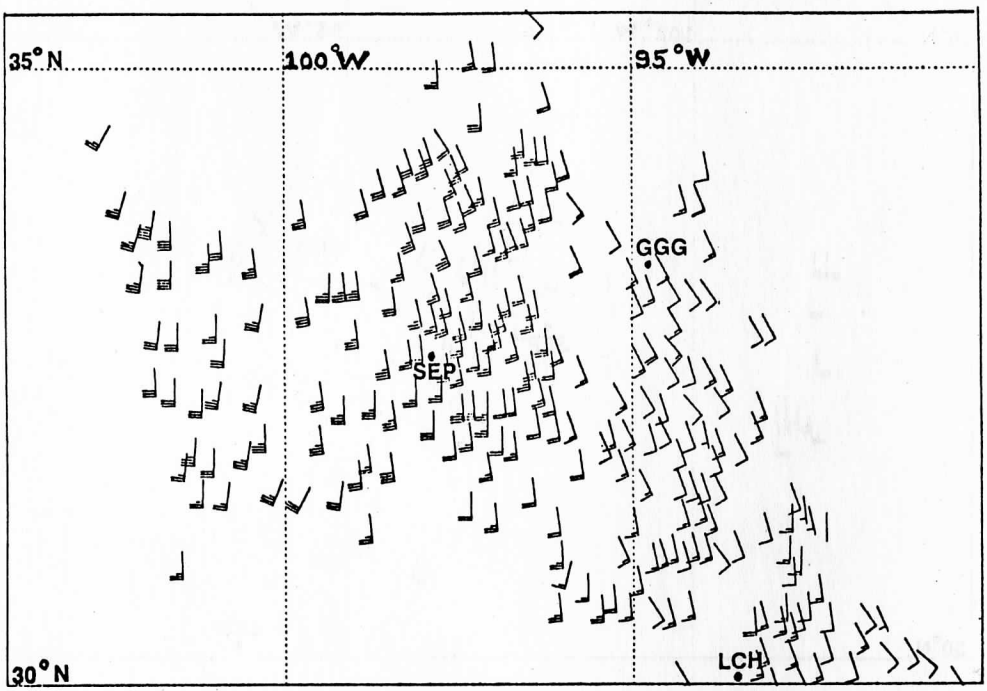

Figure I.7. Standard low level satellite wind set. 18Z, 20 May 1977.

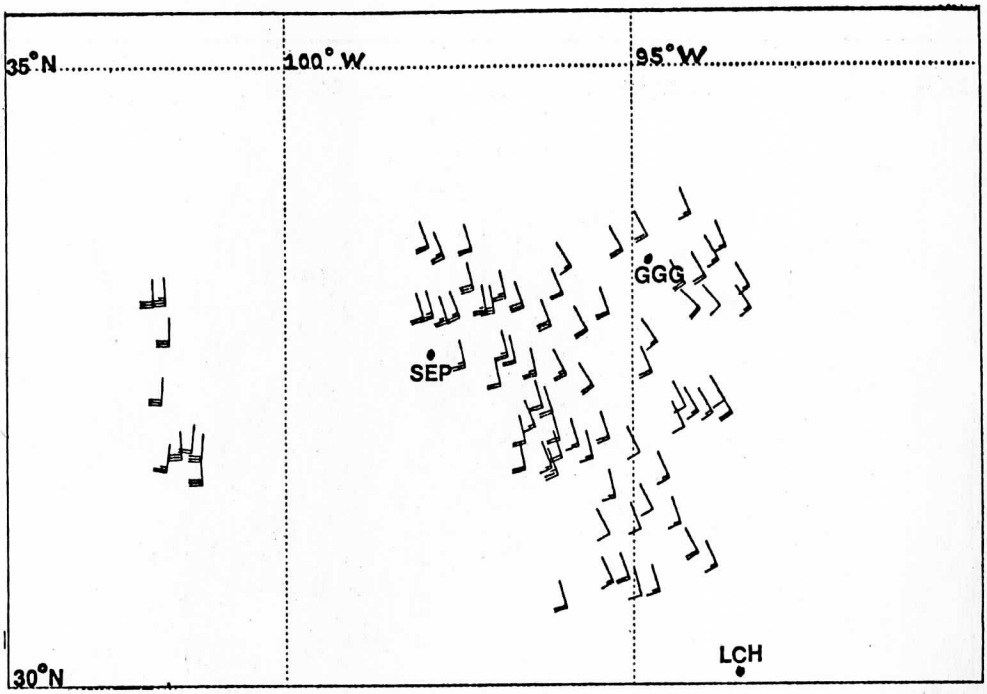

Figure I.8. 900 mb winds from satellite data using stereographic display. 18Z, 20 May 1977.

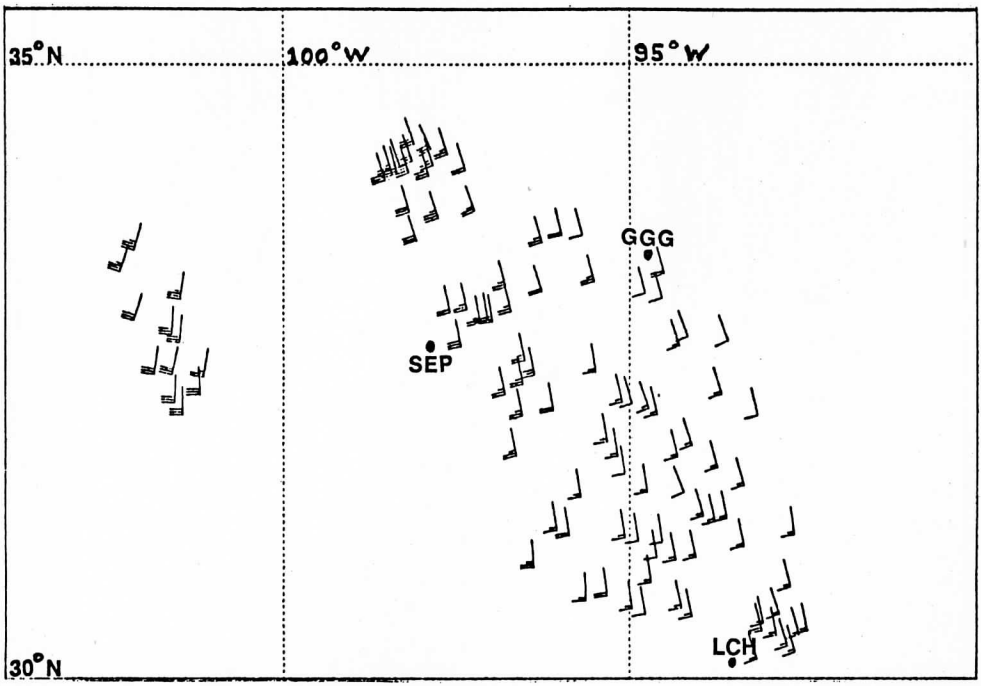

Figure I.9. 850 mb winds from satellite data using stereographic display. 18Z, 20 May 1977.

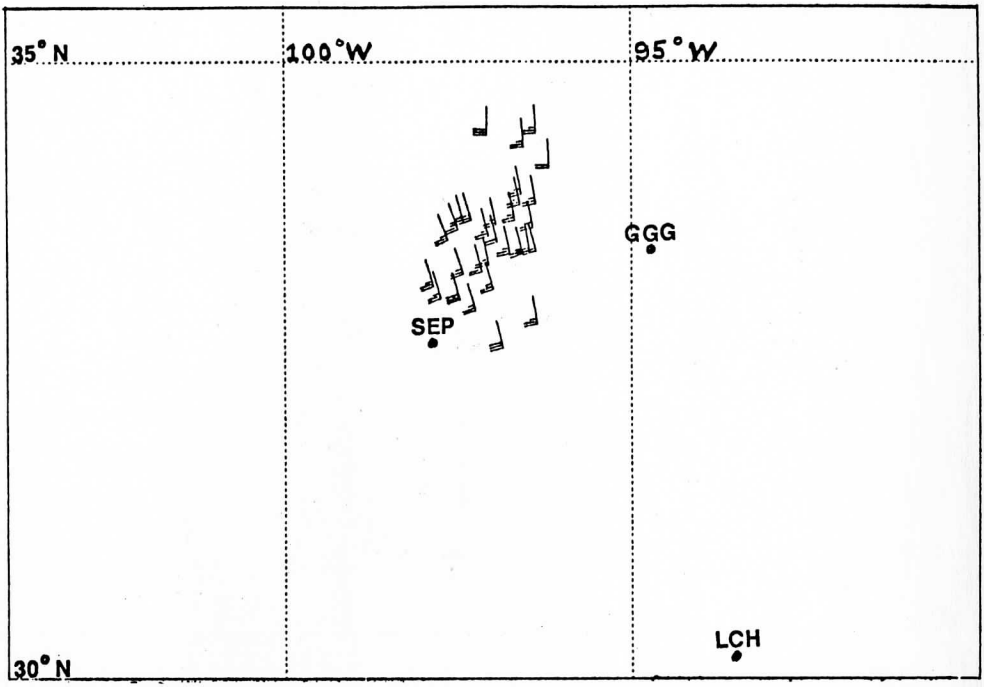

Figure I.10. 800 mb winds from satellite data using stereographic display. 18Z, 20 May 1977.

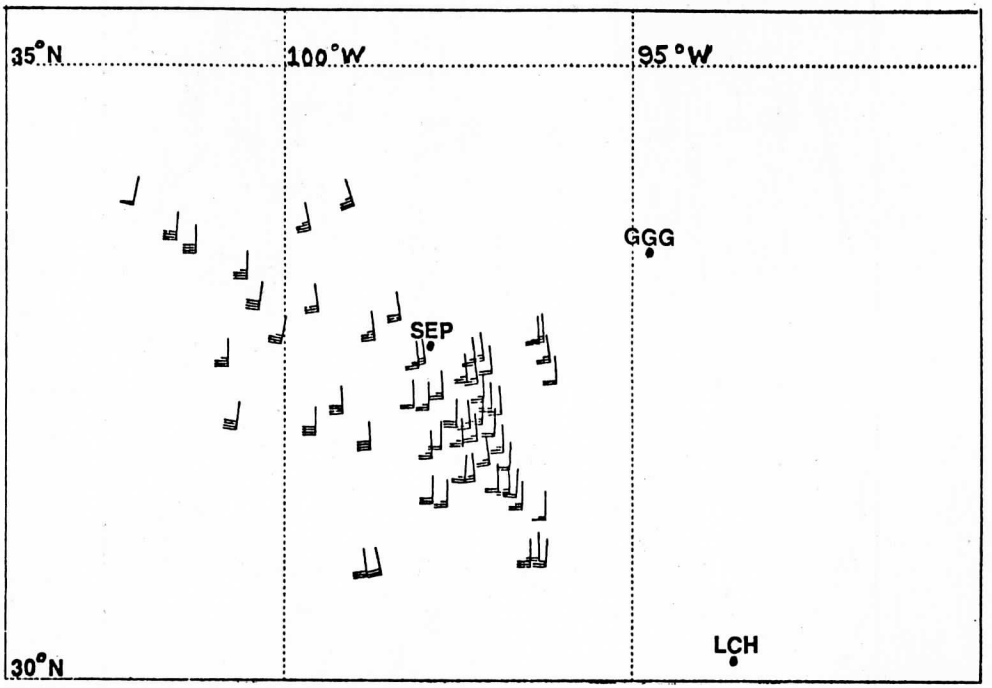

Figure I.11. 750 - 700 mb winds from satellite data using stereographic display. 18Z, 20 May 1977.

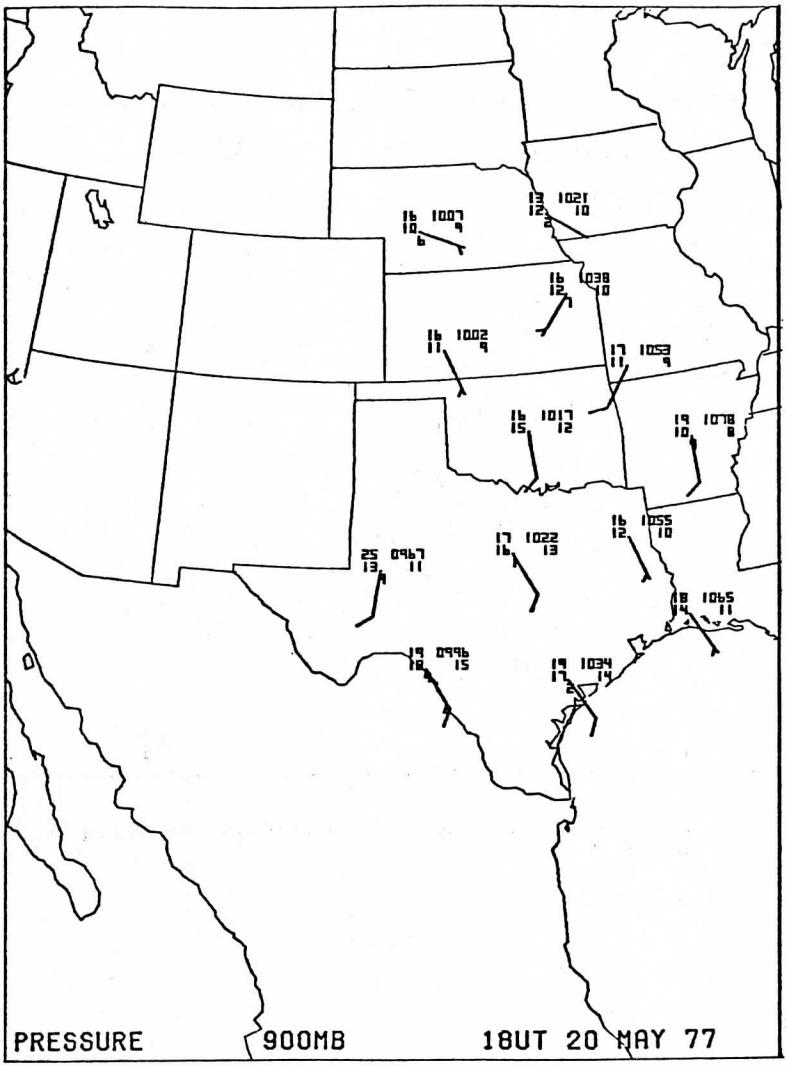

Figure I.12. 900 mb plot from rawinsonde data.

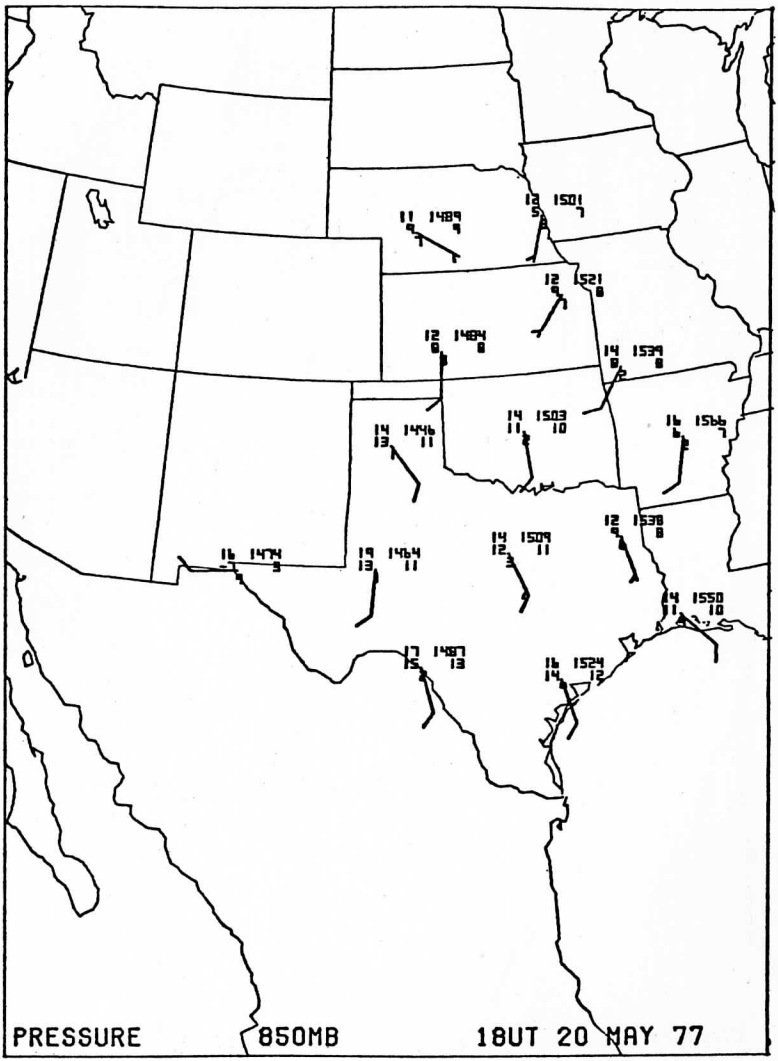

Figure I.13. 850 mb plot from rawinsonde data.

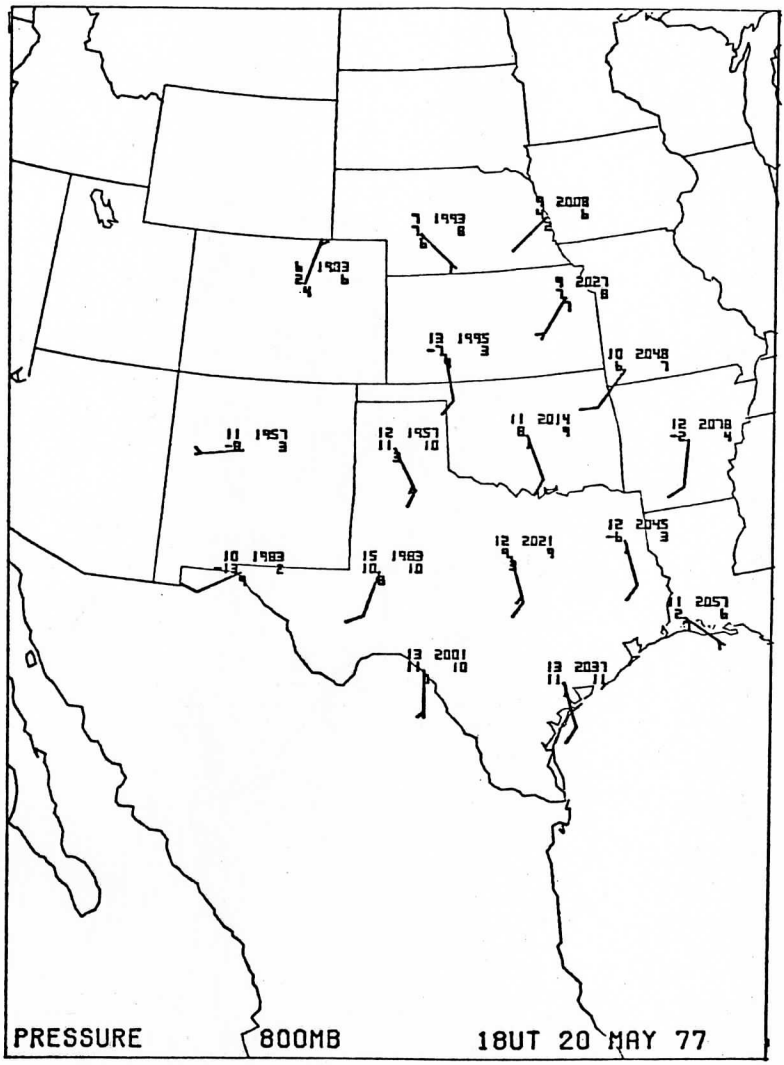

Figure I.14. 800 mb plot from rawinsonde data.

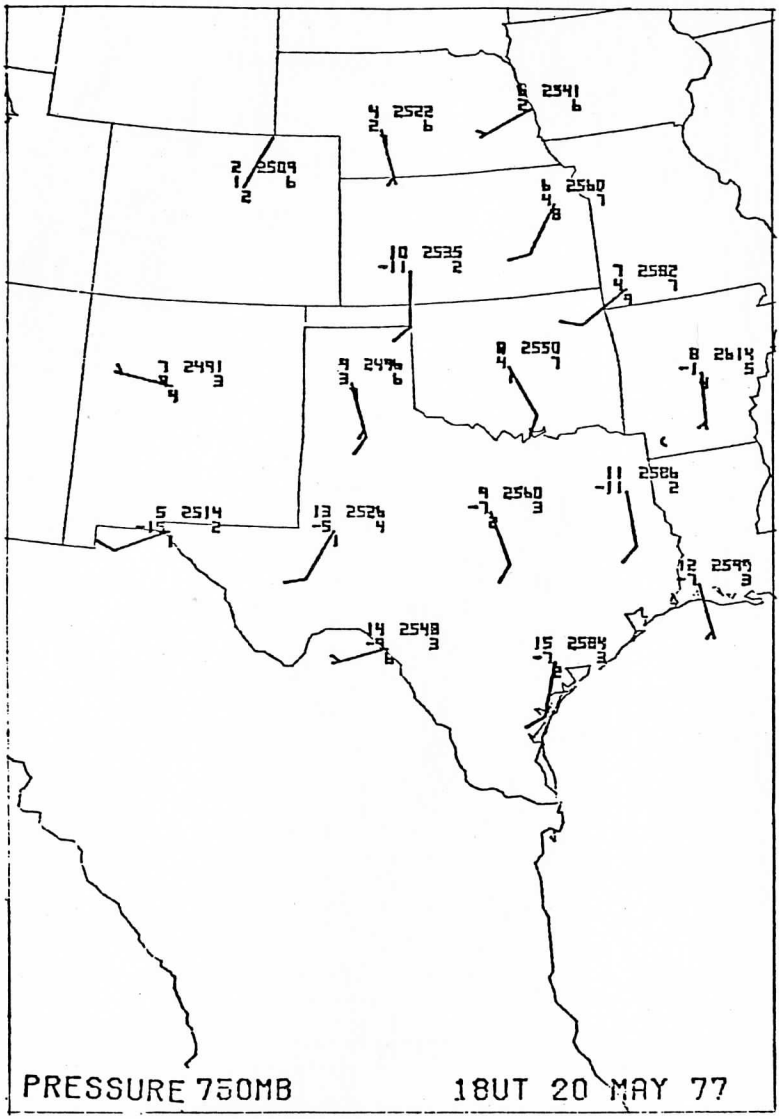

Figure I.15. 750 mb plot from rawinsonde data.

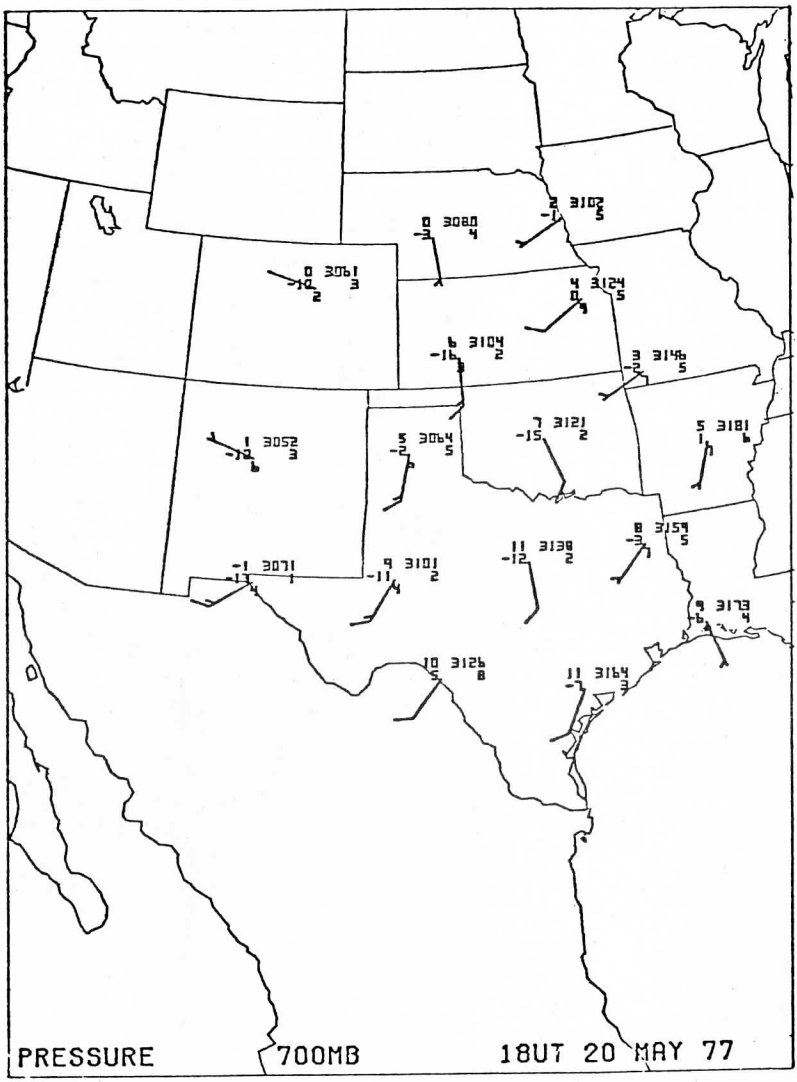

Figure I.16. 700 mb plot from rawinsonde data.

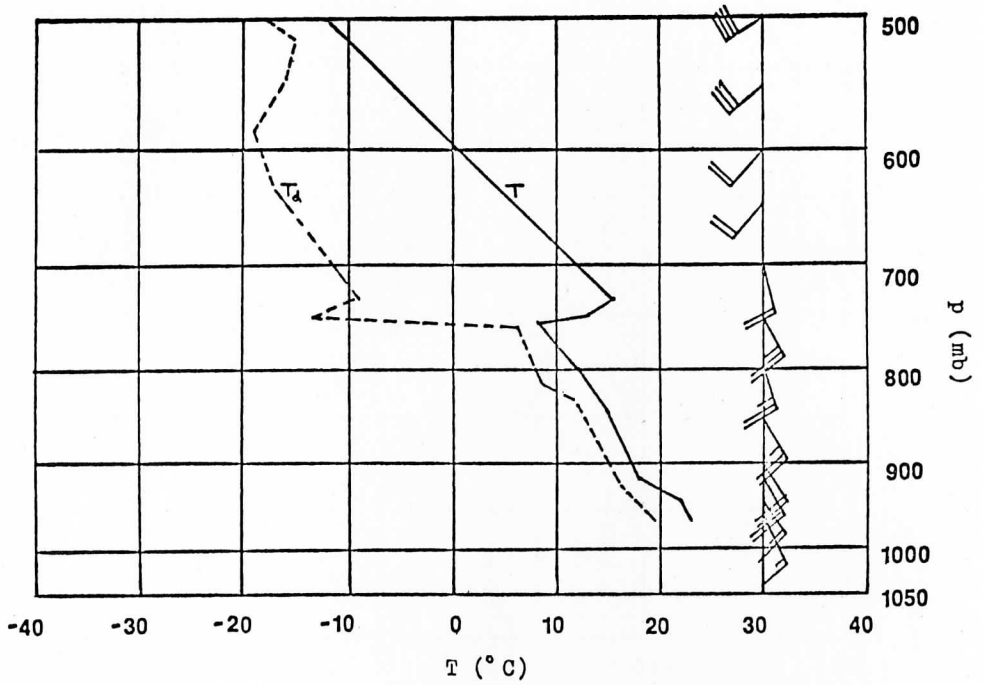

Figure I.17. SEP sounding. 18Z, 20 May 1977.

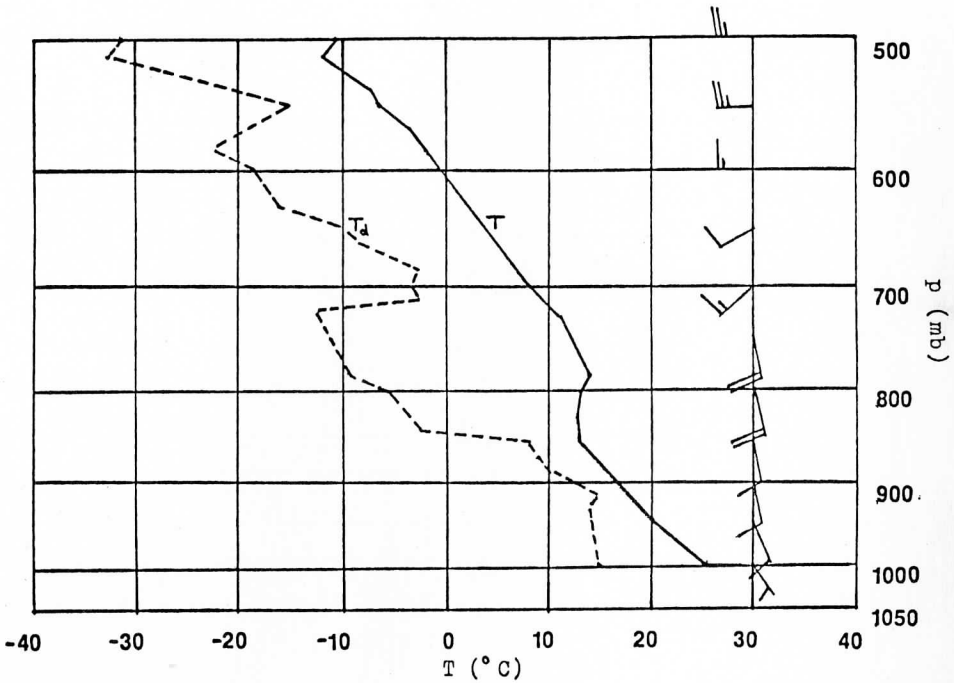

Figure I.18. GGG sounding. 18Z, 20 May 1977.

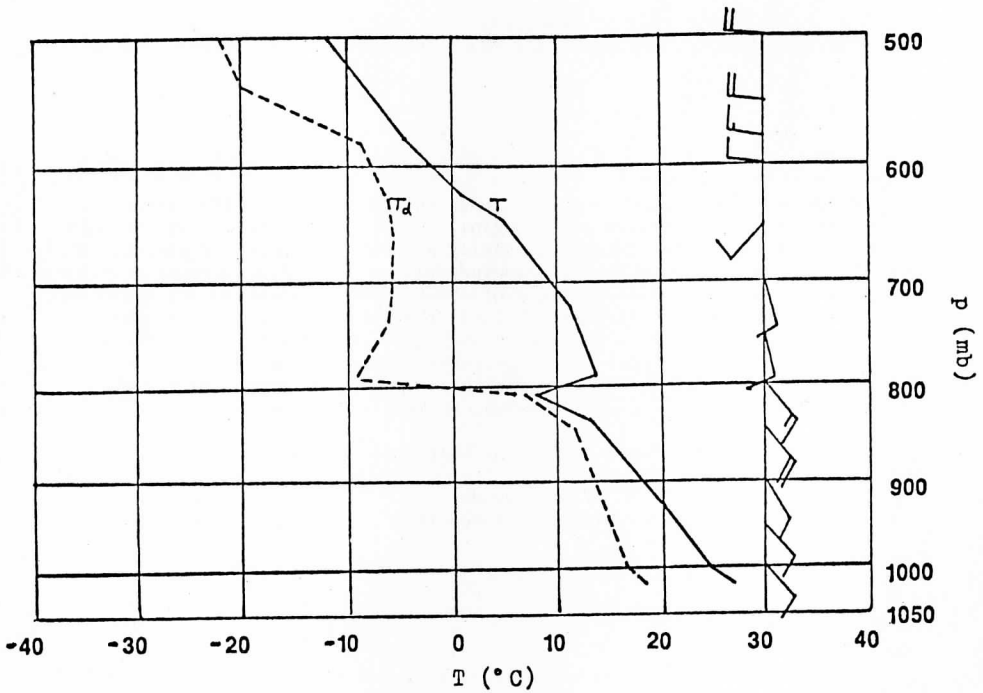

Figure I.19. LCH sounding. 18Z, 20 May 1977.

Table I.1. Wind Velocities at SEP

Height (mb)	Rawinsonde Direction	Rawinsonde Speed (kt)	Satellite Direction	Satellite Speed (kt)
900	SSE	20	SSE	20 - 25
850	SSE	25	SSE	25 - 30
800	SSE	25	SSE	25 - 30
750 - 700	S - SSE	20 - 25	S - SSE	20 - 25

Examination of the GGG sounding leads one to expect clouds primarily at 850 mb where a deep inversion layer begins. Above 850 mb the air is very dry, and below this level the sounding is nearly adiabatic. Table I.2 compares the expected wind velocities with the measured values. Note that a group of winds were measured at 900 mb having speeds of about 20 kt. No clouds are indicated by the sounding, although if they did form, they would be moving from the SSE at about 10 kt. It is clear that the clouds used as targets in this instance actually were situated higher in the atmosphere, perhaps around 800 mb. The measured winds at 850 mb agree much more closely with the expected values. At the higher levels no clouds were observed in keeping with expectations.

Table I.2. Wind Velocities at GGG

Height (mb)	Rawinsonde Direction	Rawinsonde Speed (kt)	Satellite Direction	Satellite Speed (kt)
900	---	---	SSE	15 - 20
850	SSE	10	SSE	10
800	---	---	---	---
750 - 700	---	---	---	---

At LCH the air increased in moisture from the surface to about the 800 mb level, then dried out very abruptly. From stability considerations one would expect to find clouds only at 800 mb where the very moist air is capped by a strong inversion. Table I.3 gives a comparison of expected and observed velocities at this station. With the exception of the fact that the clouds measured at 850 mb should probably have been placed at 800 mb according to the sounding, the correlation is again quite good.

Table I.3. Wind Velocities at LCH

Height (mb)	Rawinsonde Direction	Rawinsonde Speed (kt)	Satellite Direction	Satellite Speed (kt)
900	---	---	---	---
850	---	---	SSE	15
800	SSE	15	---	---
750 - 700	---	---	---	---

Wind speeds in the layer between 900 and 700 mb show only a slight variation on the order of 5 kt. The primary feature differentiating the various levels is the wind direction which veers significantly with height. Figure I.20 illustrates this tendency. At each level (plotted along the ordinate) a dot represents one satellite wind from the direction given by the abscissa. Note the shift in maximum concentration of winds from approximately 150 at 900 mb to 175 at the 750 - 700 mb layer. On the same figure wind directions measured at the three rawinsonde stations are plotted for comparison. The similarity in the profiles for SEP and GGG to the satellite winds indicates that the separate layers revealed by the false stereo method are valid. While the LCH profile differs significantly, particularly in the lowest 100 mb, it should be noted that few clouds were tracked in this region, and the majority of those that were available exhibited probable height errors.

This analysis indicates that the false stereo techniques works very well for separating multiple cloud layers. The primary difficulty lies in accurately assigning heights to the various layers. The probable cause of the errors in height estimation is the use of climatological rather than actual recent soundings. This problem could be remedied by incorporating current sounding data into that section of the false stereo program which is responsible for height estimation. In cases where true stereo is available no such difficulty would exist.

V. CONCLUSIONS AND SUGGESTIONS FOR FURTHER RESEARCH

The false stereographic technique described in Section III may be applied to any set of satellite imagery containing simultaneous visible and infrared data. Due to the problem of estimating cloud emissivities in performing the temperature-to-height conversion, the best results are obtained when the blackbody assumption is not violated. Fields of low level cumulus type clouds are generally suitable.

When multiple layers of cumulus clouds are present, time lapse sequences of satellite images displayed in false stereo clearly show the individual layers with consistent flow patterns at each level. This is a significant clarification of the unprocessed data where multiple layers frequently cause confusion as to the actual pattern of air motion at low levels.

In Section IV a case study was described in which wind sets were produced by tracking small cumulus clouds in advance of a severe storm system. Comparisons were made between rawinsonde wind data, a standard satellite low level wind set including all vectors from the surface to a height of approximately 700 mb, and four wind sets at 50 mb increments from 900 to 750 mb produced with the aid of a false stereo display. The results of this case study indicate that the three dimensional image is an effective tool enabling the operator to visually discriminate between layers of clouds as thin as 50 mb.

In comparing the satellite winds with rawinsonde observations it becomes

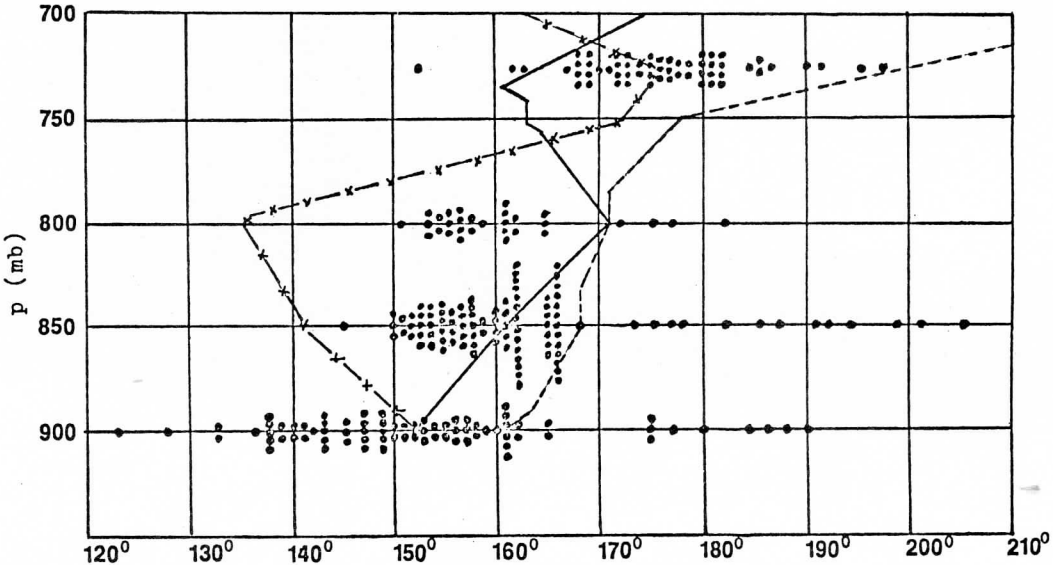

Figure I.20. Wind directions from satellite and rawinsonde data.

evident that, while individual layers are clearly separated by this technique, the heights assigned to those layers may be off by 50 to 100 mb, as was apparently the case at GGG and LCH. The most probable cause of these height errors is the use of climatological rather than actual recent soundings by the false stereo program.

Examination of Figure I.20 shows a pronounced tendency for veering of the wind with height over most of the region. As discussed in Section II, combining winds from all of these levels to form one composite low level wind set (similar to Figure I.7) would give a very misleading picture of the actual structure of the atmosphere between the surface and 700 mb. Fictitious patterns of convergence and divergence would appear on an objective analysis of such a wind set and could be very detrimental to a forecast based upon the results. If instead the forecaster had a quick and efficient means of separating the various layers of low level clouds, such as a stereographic display, a more accurate description would be available.

Additional studies are needed to test and improve the accuracy of height assignments to the cloud layers revealed by the false stereo display. Since false stereo is a convenient substitute for the more desirable but less easily obtained and processed true stereo, it is suggested that a study be undertaken whereby images are produced by both methods from the same data and compared. The true stereo images could then be used to check the accuracy of the false stereo.

The feasibility of incorporating current local soundings into the height assignment routine of the false stereo program should be pursued as a means of improving its accuracy. If the individual levels can be properly placed in the vertical, a quantitative study could be performed to determine the effect of this improved height discrimination on objectively analyzed fields of divergence and vorticity. The validity of such analyses in previous research should be questioned.

Finally, research is needed in the area of devising a method for combining data from different sources such as rawinsondes and satellite cloud winds. This would lead to one superior wind set having the advantages of each individual source. Horizontal coverage would be increased by the inclusion of satellite winds, while the rawinsonde data would improve vertical resolution and help fill the gaps left by cloud-free regions.

REFERENCES

Anderson, et al., 1974: Applications of Meteorological Satellite Data in Analysis and Forecasting. ESSA Technical Report NESC 51.

Bryson, W.R., 1978: Cloud Height Determination From Geosynchronous Satellite Images. Ph.D. Thesis, University of Wisconsin-Madison.

Chatters, G.C. and V.E. Suomi, 1975: The Applications of McIDAS. IEEE Trans. Geosci. Electron., GE-13, 137-146.

Hinton, B.B., 1977: Climatology Based On Winds Derived From Cloud Motions. Studies of Soundings and Imaging Measurements, Final Scientific Report on NAS5-21798, 1974-1976, Univ. of Wis. Press.

Houghton, D.D. and D.K. Lee, 1977: Mesoscale Wind Fields For the May 6, 1975 Omaha Tornado Situation Derived From SMS Cloud Observations. Tenth Conf. On Severe Local Storms, Amer. Meteor. Soc., 16-21.

Houghton, D.D. and T.A. Wilson, 1975: Mesoscale Wind Field For a Severe Storm Situation Determined From Synchronous Meteorological Satellite (SMS) Cloud Observations. Ninth Conf. on Severe Local Storms, Amer. Meteor. Soc., 187-192.

Hubert, L.F. and L.F. Whitney, Jr., 1971: Wind Estimation From Geostationary-Satellite Pictures. Mon. Wea. Rev., 99, 665-672.

Izumi, Y. and M.L. Barad, 1963: Wind and Temperature Variations During Development of a Low-level Jet. J. Applied Meteor., 2, 668-673.

Kreitzberg, C.W., 1977: SESAME '77 Experiments and Data Availability. Bull. Amer. Meteor. Soc., 58, 1299-1301.

Maddox, R.A., A.J. Negri and T.H. Vonder Haar, 1977: Analysis of Satellite Derived Winds for April 24, 1975. Tenth Conf. On Severe Local Storms, Amer. Meteor. Soc., 54-60.

McNulty, R.P., 1978: On Upper Tropospheric Kinematics and Severe Weather Occurrence. Mon. Wea. Rev., 106, 662-672.

Mosher, F.R., 1974: SMS Cloud Heights. Space Science and Engineering Center (SSEC). Publication.

Mosher, F.R., 1975: Report on the Wisconsin Participation in the August-September 1975 DST. SSEC Publication.

Peslen, C.A., 1977: A Satellite Interpretation of the Dynamics of a Severe Local Storms Area Using 5 Minute Interval SMS Data. Tenth Conf. on Severe Local Storms, Amer. Meteor. Soc., 1-7.

Pichel, W., C.L. Bristor and R. Brower, 1973: Artificial Stereo: A Technique For Combining Multi-channel Satellite Image Data. Bull. Amer. Meteor. Soc., 54, 688-691.

Purdom, J.F.W., 1971: Satellite Imagery and Severe Weather Warnings. Seventh Conf. on Severe Local Storms, Amer. Meteor. Soc., 120-127.

Raymond, D.J., 1977: Instability of the Low Level Jet and Severe Storm Formation. Tenth Conf. on Severe Local Storms, Amer. Meteor. Soc., 515-520.

Shapiro, M.A. and P.J. Dennedy, 1974: A Multiple-Structured Frontal Zone-Jet Stream System as Revealed by Meteorologically Instrumented Aircraft. Subsynoptic Extratopical Weather Systems, (ed. M. Shapiro), Mat. Center Atmos. Res., Boulder, Colo., 242-260.

Smith. E.A., 1975: The McIDAS System. IEEE Trans. Geosci. Electron., GE-13, 123-136.

Smith, E.A. and D. Phillips, 1973: McIDAS Cloud Tracking System. SSEC Publication.

Suchman, D., D.W. Martin, F.R. Mosher, B. Sawyer and K.G. Bauer, 1975: Preliminary Assessment of the Cloud Tracking System Developed at the University of Wisconsin. SSEC Publication.

Suomi, V.E. and R.J. Parent, 1964: Initial Proposal to NASA for an ATS Technological Experiment. Unpublished.

Uccellini, L.W., 1977: The Coupling of Upper and Lower Tropospheric Jet Streaks and Implications For the Development of Severe Convective Storms. Ph.D. Thesis, University of Wisconsin-Madison.

Whitney, L.F., 1977: Relationship of the Subtropical Jet Stream to Severe Local Storms. Mon. Wea. Rev., 105, 398-412.

LIST OF FIGURES

LIST OF TABLES

CHAPTER II

INTRACOMPARISONS OF SMS WIND SETS: A STUDY USING RAPID-SCAN IMAGERY

Gregory L. Johnson

ABSTRACT

This study examines the effect that varying the resolution of satellite imagery has on cloud-tracked winds. Very little research has been conducted on this subject, particularly for clouds over land.

Rapid-scan satellite data is used as a basis for computing cloud-tracked wind fields over the south central U.S. on three synoptically different days in 1978. Winds from 30, 15, 6, and 3 minute time intervals are produced, discussed, and intercompared. The latter includes examination of streamline and isotach maps, comparisons of mean and standard deviation values for speed and direction, and a discussion of operator observations. Low level clouds are tracked on 3 separate days, cirrus level, on 2 days.

Nearly ten times as many low cloud winds were computed on days of rapid cloud growth and dissipation using a 3 minute interval as, were computed using the conventional 30 minute interval; spatial coverage of vectors was also significantly greater. The difference in number of cloud winds was less pronounced on days with longer cloud lifetimes. Cirrus clouds, with lifetimes much greater than that of low level cumuli, could be tracked more easily with a 30 minute interval, and produced a smoother wind field. Whether tracking cumulus or cirrus, viewing a 30 minute interval sequence, as well as examining the synoptics, always proved valuable before any tracking was performed, to assess the situation. Short intervals caught the mesoscale features that longer intervals missed, but required much more operator time for tracking.

It is recommended that the conventional 30 minute interval with single pixel tracking methods be used on cirrus clouds, while a shorter interval (6 to 10 minutes) be used on low level clouds. A change in the present scanning method on geosynchronous satellites to allow for a greater frequency of images should therefore be considered.

I. INTRODUCTION

The usefulness and accuracy of cloud winds to represent the environmental wind field has been a subject of discussion and research since the launching of geosynchronous satellites in the 1960's. The utility of such information, particularly over oceanic areas relatively void of atmospheric data, has been examined in several studies in the decade since ATS-I was launched. In these

studies, however, there has been little examination of the impact upon cloud winds by variations in the space and time resolutions of the images used. Such an investigation will be made here.

Research into the accuracy and errors in cloud-tracked winds was performed by Hubert and Whitney (1971). They identified five possible sources of error from satellite-tracked winds: 1) errors due to uncertainty of target cloud height, 2) errors due to non-advective cloud motion, 3) errors of measurement, 4) errors in tracking cloud targets, and 5) errors due to nonrepresentative rawinsonde observations. Cloud height identification was by far the most significant problem mentioned, and remains a problem in all tracking systems today. Other errors are minimized by the operator's meteorological judgment and experience in cloud tracking. Errors in the tracking system itself, most notably misregistration and navigation of images, has also presented problems, but a technique developed at the University of Wisconsin has minimized the navigation errors (see Mosher, 1979). The Wisconsin system (the Man-computer Interactive Data Access System, or McIDAS) was the one employed in this study.

The representativeness of cloud displacements was also discussed by Hubert and Whitney (1971), where they found a level of best fit (LBF) between the tracer cloud's movement and radar winds in the same vicinity. 850 mb was the LBF for cumulus clouds, while 200 mb was found to be best for cirrus level winds. Other investigations have put the LBF for low cumulus closer to 950 mb (Bengtsson and Morel, 1974). Comparisons of ground truth winds and satellite winds are made in this study, whenever possible, to determine the LBF for clouds tracked and for determination of accuracy in wind fields.

In an assessment of quality of wind sets, Suchman and Martin (1976) found differences between satellite and ship winds in the GATE area to be less than 3 $msec^{-1}$. In a study by Bauer (1976), intercomparisons were made between cloud winds and radiosonde winds, finding mean absolute differences of 4.4 $msec^{-1}$ for the u-component, and 4.6 for the v-component of the wind. When a similar intracomparison was done for radiosondes, difference values of 4.2 and 5.1 $msec^{-1}$ for u and v, respectively, were found. Thus, consistency in the accuracy of cloud winds is on a level comparable to that of conventional radiosonde reports.

A study by Hasler, Shenk and Skillman (1977) focused on in situ aircraft verifications of the accuracy of cloud tracked winds. Their findings showed that, at cloud base, trade-wind cumulus would move within about 1.3 $msec^{-1}$ of the wind, and within about 1.6 $msec^{-1}$ for cirrus clouds. Both of these differences are no larger than those for radiosonde winds, and thus reliance upon cloud motions for ambient wind determinations seems reasonable.

Fujita, Pearl, and Shenk (1975) investigated the size of a cumulus cloud in relationship to representativeness. Cumulus plumes (less than .5 km diameter) were found to be bad targets because of their unsteady updrafts. Turrets (.5 to 3.2 km) were said to be the best for tracking, but were hard to track because they were so small and short lived. Small cells, 3.2 to 8 km in size, had longer lifetimes and were also good for tracking, while

cells larger than these probably had active convective processes, causing them to move differently from the environmental wind field.

The brief lifetimes of these small clouds thus requires a short time interval between images to capture their movement. Tecson, Umenhofer, and Fujita (1977), in a study of cloud motions from 5 minute interval SMS pictures, stated: "...the mean life of these best targets are extremely short. Rapid-scan pictures provide us with the only solution toward this trade off." Rapid scan data is used in this study, with time intervals of 3, 6, and 15 minutes compared to the conventional 30 minute interval.

More recently, Rodgers, et al. (1979) investigated the benefits of using a shorter time interval in tracking clouds around tropical cyclones. While this paper deals with extratropical data, primarily over the south central U.S., the work of Rodgers and his colleagues did show that rapid scan images significantly increased the number of trackable clouds (a nearly tenfold increase as the time interval was decreased from 30 to 3 minutes). Greater numbers of cloud tracers were also observed with improved spatial resolution. The importance of such increases will be discussed in this paper.

The focus of this study is to investigate the benefits of rapid scan data in cloud tracking over land in mid-latitudes. Both low and upper level clouds are tracked.

A discussion of the methods of data collection and analysis used along with a short summary of the workings of the McIDAS system serves as a beginning point. Wind sets of different image intervals, centered on a given time, are compared statistically and qualitatively. Operator observations and notes from cloud tracking experience are also included. Maps of raw winds and streamlines and isotachs will be shown. In a concluding section, analysis of data and maps, and a discussion of the applicability of this study will be made.

II. METHOD

This section includes a description and discussion of the limitation of the data used in this study, a discussion of cloud tracking schemes available on McIDAS, and their use in this investigation, a discussion of space and time resolutions and their bearing on cloud tracking, and a description of techniques used for intracomparisons of wind sets.

A. Data

Rapid scan days have been designated during 1977, 1978, and 1979 as a part of the Severe Environmental Storms and Mesoscale Experiment (SESAME) (Lilly, 1978). There were 11 such days in 1977 and 12 in 1978. This data is routinely archived on cassette tape at the Space Science and Engineering Center (SSEC) of the University of Wisconsin, along with conventional service-A (surface reports) and service-C (radiosonde) data. The latter is used both for ground truth and for extending analyses into cloud free regions. Surface

reporting stations are shown in Figure II.1. The areas covered by cloud winds when low-level cloud winds were computed are indicated by areal outlines. Figure II.2 shows the distributions of radiosonde stations.

Rapid scan format consists of full disc pictures taken on the hour and half hour, with limited area scans at 9, 12, 15, 18, 21, and 24 minutes after the hour and half hour. A three frame sequence is most common for tracking purposes, and thus 3, 6, 15, and 30 minute intervals can all be centered on either 15 minutes before the hour or half hour. Visible and IR data for a one hour period from three separate rapid scan days in 1978 provide the data base in this investigation: April 9, April 17, and May 20.

As Figures II.1 and II.2 show, wind fields were computed between latitudes 30° and 40°N. At 40°N, the spatial resolution of the GOES-II digital data used in this study is approximately 1.2 km for the visible channel and 9.4 km in the IR. GOES-II has a sub-satellite point at 0°N, 75°W, thus scanning all of the central and eastern U.S.

In most cloud tracking procedures three principal sources of error are normally present (Suchman and Martin, 1976): Navigation, operator, and image resolution errors. Absolute navigation errors (where there is apparent earth motion between image frames) have been reduced to approximately two full-resolution picture elements on McIDAS (1.6 km for visible sensor at sub-satellite point). Relative alignment errors between successive images are much less than a picture element (pixel), and are therefore negligible in cloud tracking (Mosher, 1979). Operator errors are not significant in this study, as one operator performed all tracking. Image resolution errors (the matching of time and space resolutions, affecting wind accuracy) may be significant, particularly for the shortest time intervals, and will be discussed in a following section.

B. Cloud Tracking

On the McIDAS system there exist two types of cloud tracking methods--single pixel and correlation. In single pixel tracking the cursor on the video screen is often made as small as possible (i.e. one pixel), and is then positioned over the portion of the cloud to be tracked throughout the image sequence. This is the method which has proven to work best for clouds which are changing their shape and size rapidly, and for multiple layer clouds.

The correlation method gives the operator less discretion than does single pixel. After a cloud tracer is selected by the operator, the cursor (generally 10 pixels square, at a minimum) is positioned over the tracer. Correlation algoritms are then used by the computer on the digital data, which tracks the cloud automatically. Correlation works best for clouds with sharp brightness centers, and for clouds which do not change size or shape significantly through the time interval.

Low clouds which are tracked in this study are generally cumuli over land, which grow in size and change shape quite rapidly. For this reason, and for consistency, all low clouds are tracked using the single pixel method. Cirrus

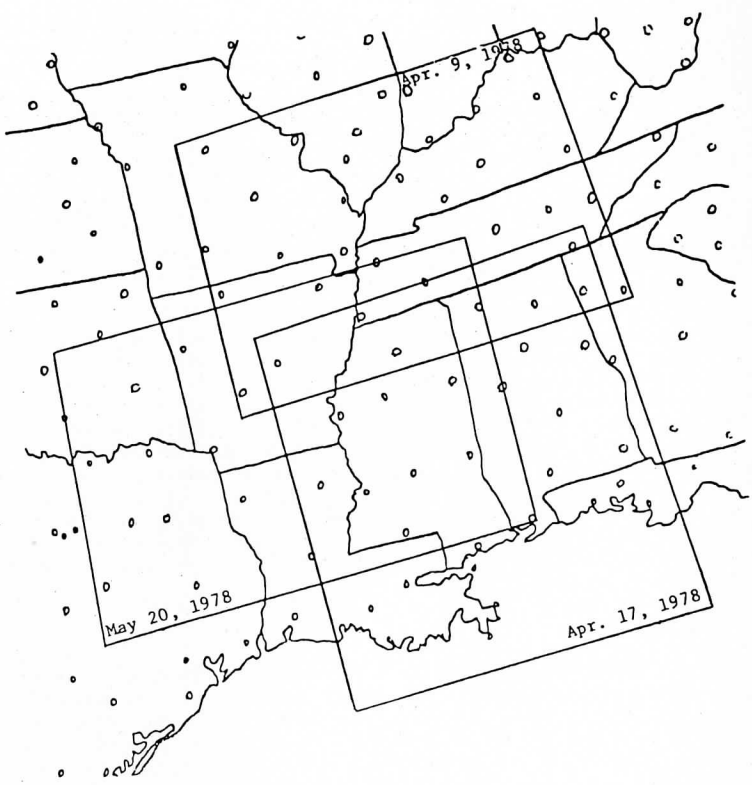

Figure II.1. Surface reporting stations, and outlines of low level tracking regions.

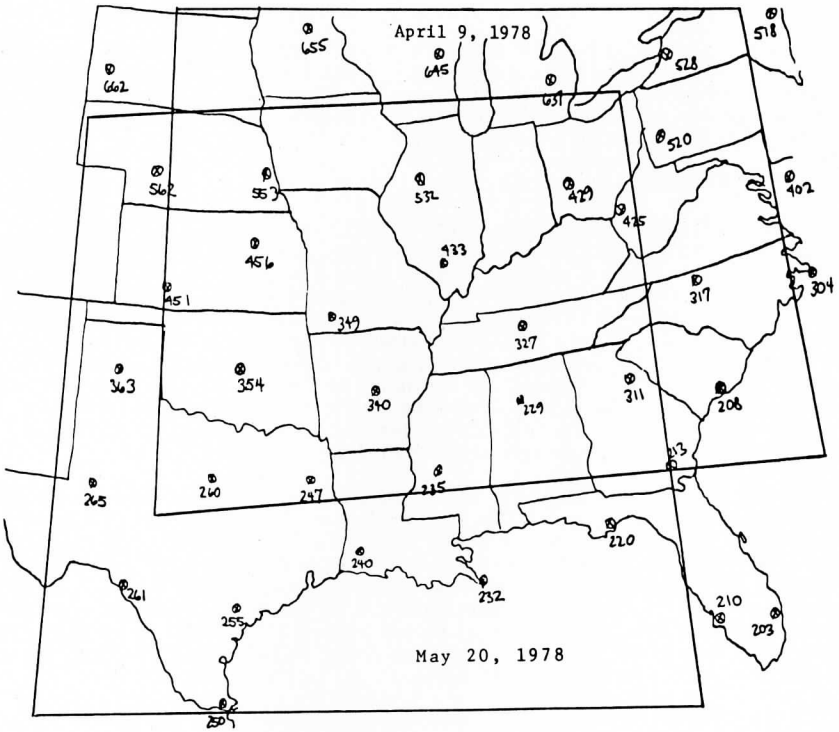

Figure II.2. Radiosonde stations, and outlines of cirrus level tracking regions.

clouds are tracked using both correlation and manual (single pixel) procedures. As the results section will show, single pixel produces more consistent results and more wind vectors than does correlation. Lack of a distinct brightness center and the more "hazy" appearance of cirrus may be a reason for problems in correlation tracking at this level.

C. Space and Time Resolutions

Selecting a proper match in temporal and spatial resolutions is a necessity for accuracy in cloud tracked winds. The size of the cloud tracer is an important factor: The cloud must exist long enough to be followed in a sequence of images and must be large enough to be viewed by the operator. Fortunately, there is usually a direct relationship between cloud size and lifetime. Tecson, et al. (1977) estimated that the lifetimes of small cumulus clouds 2 to 3 miles in size was only about 23 minutes, and thus concluded that a picture interval of 3 minutes was necessary for tracking land cumuli. Higher clouds (cirrus) of 4 to 6 mile size were estimated to "live" for up to 5 hours, and hence could be tracked from longer interval images. The results of this study show similar findings.

Once cloud size and height are identified, proper space-time resolution matching becomes important. The best indicator of this matching tends to be experience; Suchman and Martin (1976) found that "a 30 minute picture interval is well matched to 2 km (1 n mi) data; a 15 minute interval to 1 km data". Mosher (1979) states that .8 km data need 3 to 10 minute intervals, 1.6 km data need 6 to 15 minute intervals, and 6.4 km data need 30 minute intervals. He also states that for a cloud to be identifiable it should be at least 10 pixels across on the image. A cloud was found to be identifiable in this study when only 4 to 5 pixels in size.

The random error resulting from the matching of space and time resolutions puts absolute limits on the accuracy of cloud tracked winds, and is implicit in the matching requirements found from experience. As the spatial resolution becomes larger and the time interval decreases, the random error in both wind speed and direction increases. Table II.1 shows the error in $msec^{-1}$ for time versus space resolution using single pixel tracking. 1.2 km data, used for all low level tracking in this study, is seen to have a 6.7 $msec^{-1}$ error for a 3 minute interval while only .67 $msec^{-1}$ error for 30 minute intervals. Cirrus level tracking using the single pixel method was performed using 2.4 km data for all time intervals, where again a tenfold difference in random error is seen between 3 minute and 30 minute intervals (13.3 vs. 1.3 $msec^{-1}$). Correlation tracking at this level used infrared images (9.4 km resolution at 40°N). Although random errors are somewhat reduced using correlation tracking, errors were still much greater than those from single pixel tracking due to the relatively poor resolution of the IR images used.

Figure II.3 shows how velocity errors can arise in short interval tracking. Such errors are often called image granularity errors, referring to the size or "granularity" of a picture element. The cloud outlined moves as shown from its starting position to the positions shown after 3 minutes and 30 minutes have elapsed. Three minute interval tracking extrapolates the cloud's position

RANDOM ERROR IN M/SEC DUE TO IMAGE GRANULARITY

SPACE RESOLUTION (KM)	TIME RESOLUTION 3 MIN.	6 MIN.	7 MIN.	15 MIN.	30 MIN.
1	5.5	2.8	2.4	1.1	.55
1.2	6.7	3.3	2.9	1.3	.67
2	11.1	5.5	4.8	2.2	1.1
2.4	13.3	6.7	5.7	2.7	1.3
3	16.6	6.3	7.1	3.3	1.7
4	22.2	11.1	9.5	4.4	2.2
5	27.7	13.9	11.9	5.5	2.8
6	33.3	16.6	14.3	6.6	3.3
8	44.4	22.2	19.0	8.8	4.4
9.4	52.2	26.1	22.4	10.4	5.2

Table II.1. Random error values ($msec^{-1}$) due to image granularity.

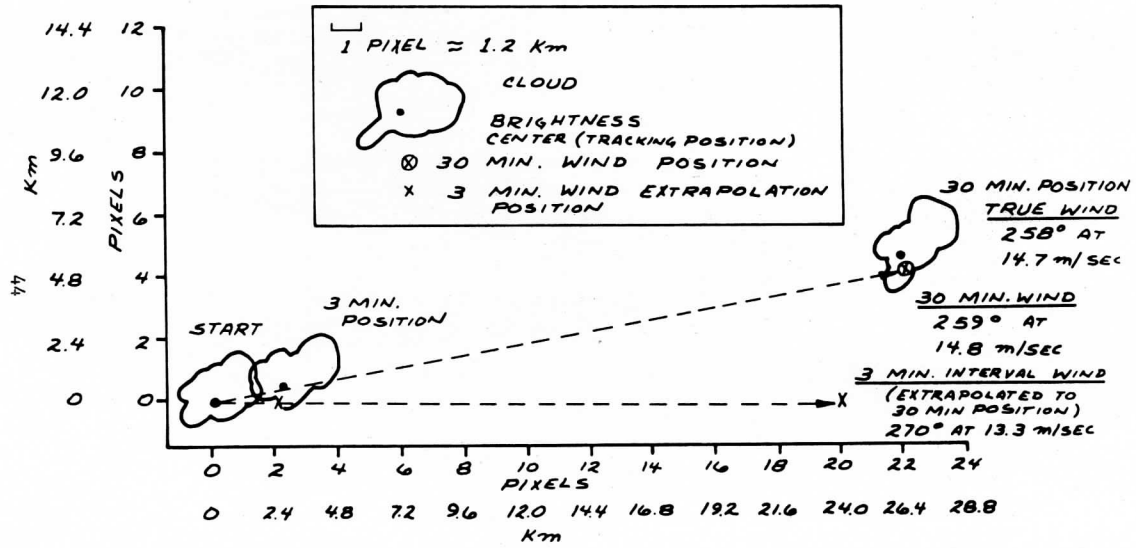

Figure II.3. Image granularity errors using full resolution data.

in a direct eastward direction and computes its speed to be 1.4 $msec^{-1}$ slower than actual, due to interpolation to the nearest pixel after 3 minutes have elapsed, as shown. The 30 minute interval wind is within 1° and 0.1 $msec^{-1}$ of the true wind, as there is no extrapolation necessary. Such differences are significant and cannot be neglected in the intracomparisons performed in the results section.

D. Analysis of Wind Sets

Once the proper tracking system, space resolution, and time resolution were selected for a particular data set, as many clouds as possible were tracked over the image sequence. Intracomparisons of these wind sets were then made. Several methods were employed for such comparisons. Among these are: 1) streamline and isotach analyses, 2) RMS calculations from grid point comparisons, 3) computations of mean and standard deviation values of speed and direction from cloud winds over an entire wind set, 4) operator observations, and 5) comparisons with surface and radiosonde data.

1) Streamlines and isotachs are computed as a part of the WIND*SRI computer program (Mancuso and Endlich, 1973). This program first obtains grid point values of u and v velocity components by objective analysis, and then produces streamline and isotach fields from this analysis. Streamline and isotach maps are compared with maps of cloud winds and those using conventional weather data.

2) RMS grid point values are obtained by comparing 30 minute interval u and v grid point data with grid point data from other time intervals. Mean u, v, and resultant wind RMS values are obtained for each wind set comparison, in addition to RMS grid point maps.

3) The mean and standard deviation values of speed and direction for entire wind fields are compared for short and longer interval sets.

4) Operator observations form a key part in this study, with well over 100 hours of cloud tracking being performed. These observations will be included throughout the results section to aid in the discussions of the intracomparisons of wind fields.

5) Winds from surface reporting stations, and radiosonde stations particularly, are quite often found to be too far apart for accurate comparisons with cloud winds. They are included in the next sections, whenever comparisons are possible.

III. RESULTS

The results from the intracomparisons of cloud-tracked winds are presented in this section. Low level cloud winds are examined first, followed by cirrus level winds.

A. Low Level Winds

9 April, 17 April, and 20 May of 1978 are the three rapid scan days chosen for cloud tracking at low levels. Each day is different synoptically. For each case, I will discuss the synoptics, show the wind sets and then present the intracomparisons.

9 April 1978

Figure II.4 shows conditions at the surface at 21Z and at 850 mb at 00Z, 10 April 1978. Both maps show west to southwest flow over the tracking region. The tracking region is east of a trough extending from Manitoba southward to a cut-off low over western Texas at 850 mb. A stationary surface front extends from southern Illinois to northern Georgia, with warmer and more moist air to the south and west of this front.

The 2030Z visible satellite image (Figure II.5) shows numerous small cumulus clouds, with a fairly distinct line of thunderstorms to the east. Cloud lifetimes of only 6 to 10 minutes were common, limiting the number of clouds that could be tracked using a 30 minute interval: Only 17 vectors were produced using a 30 minute interval, while 165 vectors were produced with a 3 minute interval (Figure II.6). 850 mb winds for the 3 radiosonde stations in the region are also displayed on both wind sets.

Table II.2 presents the results for all winds and time intervals at low levels on 9 April. Averaged over the entire region, 30 minute interval winds have a 3 $msec^{-1}$ larger magnitude than 3 minute interval winds. Only larger clouds with longer lifetimes and somewhat greater velocities were trackable over a 30 minute interval, accounting for at least part of this velocity difference.

RMS values, also shown in Table II.2, reveal closest correspondence between 30 and 15 minute interval wind sets. Significant RMS error is introduced simply because the 3 minute interval wind set has a greater spatial coverage of winds than does the 30 minute interval set. Over 6 times as many grid point values were obtained with 3 minute interval winds than the 30 minute interval winds, reflecting on this coverage difference.

17 April 1978

Strong southerly flow at low levels characterized the tracking region (see Figure II.1) on this day, with a large cut-off low over Nebraska and a ridge over the eastern U.S. Figure II.7 shows surface winds over this region at 21Z, with winds mostly southerly at 10-15 mph (5-8 $msec^{-1}$). At 850 mb (Figure II.7), winds are S-SW at 20 to 30 mph (10 to 15 $msec^{-1}$). The 2015Z visible satellite image for this day (Figure II.8) shows small cumulus covering the region, with a large area of thunderstorms to the northwest. The Gulf Coast is at the bottom of the image.

Cloud-tracked winds for this day show few differences in speed or direction for the different time intervals used. Figure II.9a (30 minute and 6 minute intervals) reveals these similarities. The largest difference appears

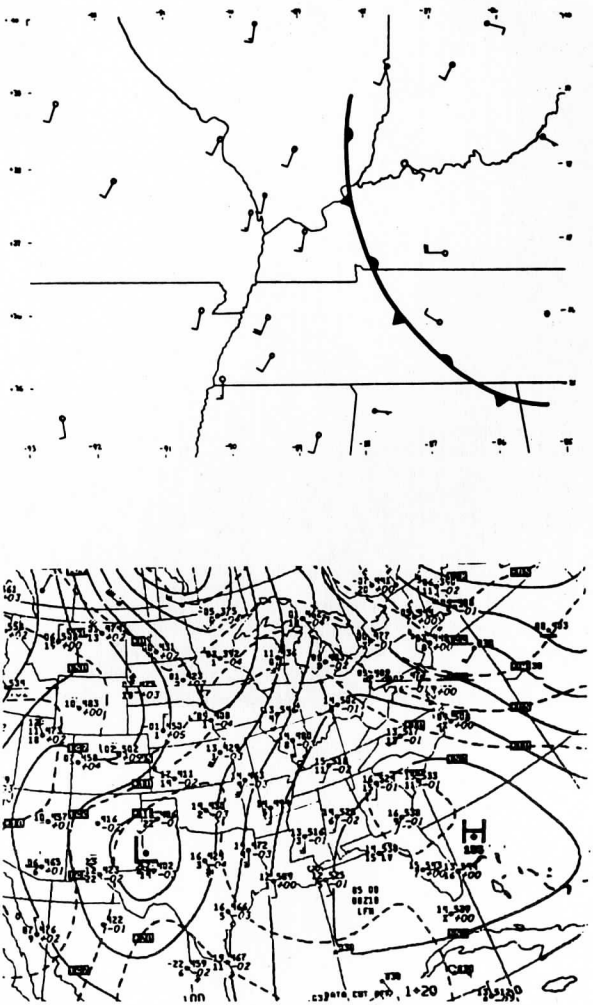

Figure II.4. Top: Surface chart 21Z, 9 April 1978.
Bottom: 850 mb chart 00Z, 10 April 1978.

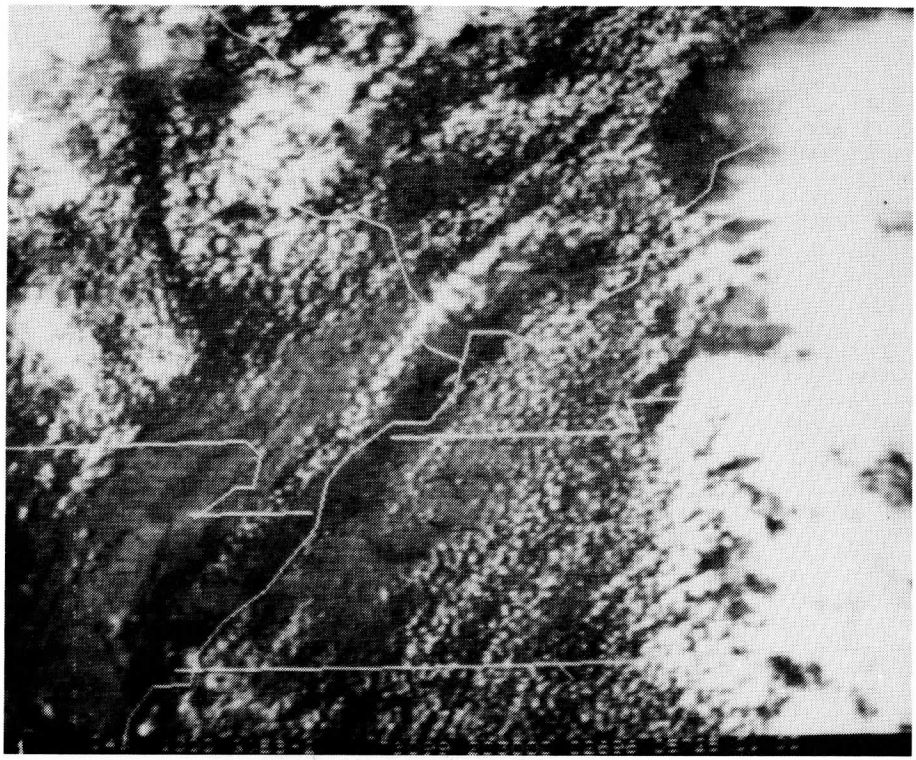

Figure II.5. 2030Z Visible satellite image, 9 April 1978.

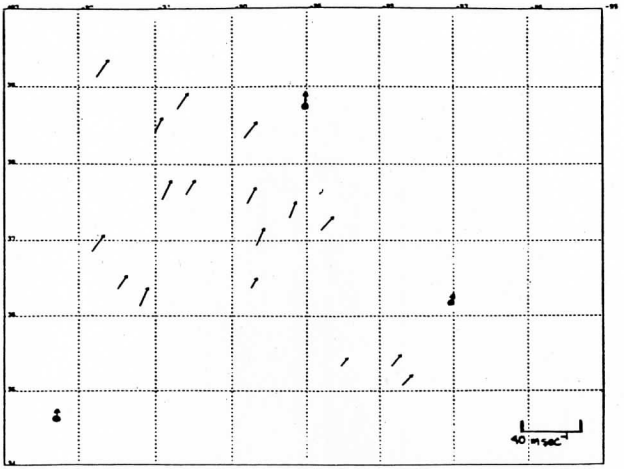

DAY 78099 TIME193000

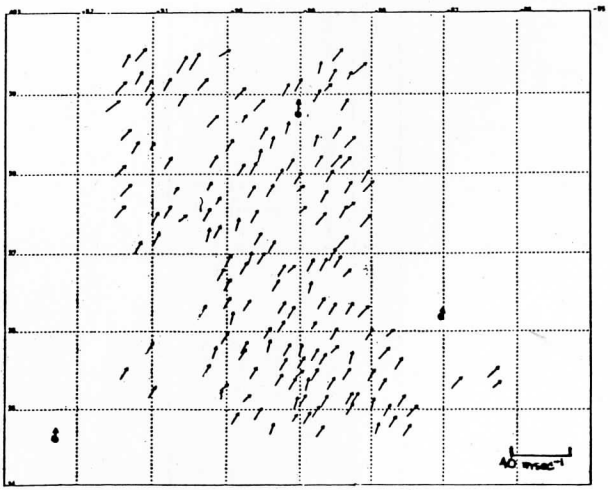

Figure II.6. Low level wind sets, 9 April 1978. Top: 30 minute interval, 2000Z center. Bottom: 3 minute interval, 1945Z center.

Time Int. (min.)	No. of Vectors	Grid Pt. Values	Direction (°)		Speed ($msec^{-1}$)	
			Mean	Std. Dev.	Mean	Std. Dev.
30	17	39	208.1	6.4	12.4	2.2
15	46	117	212.0	6.8	10.3	2.0
6	85	156	207.3	8.9	10.4	1.9
3	165	218	210.4	8.2	9.3	1.3

R M S VALUES ($msec^{-1}$)			
Time Int's. Compared (min.)	Mean U-Comp.	Mean V-Comp.	Mean Resultant Wind
30 min. vs. 15 min.	2.7	4.4	5.2
30 min. vs. 6 min.	3.1	5.4	6.3
30 min. vs. 3 min.	3.5	5.6	6.7

Table II.2. Cloud tracking results, low level
9 April 1978.

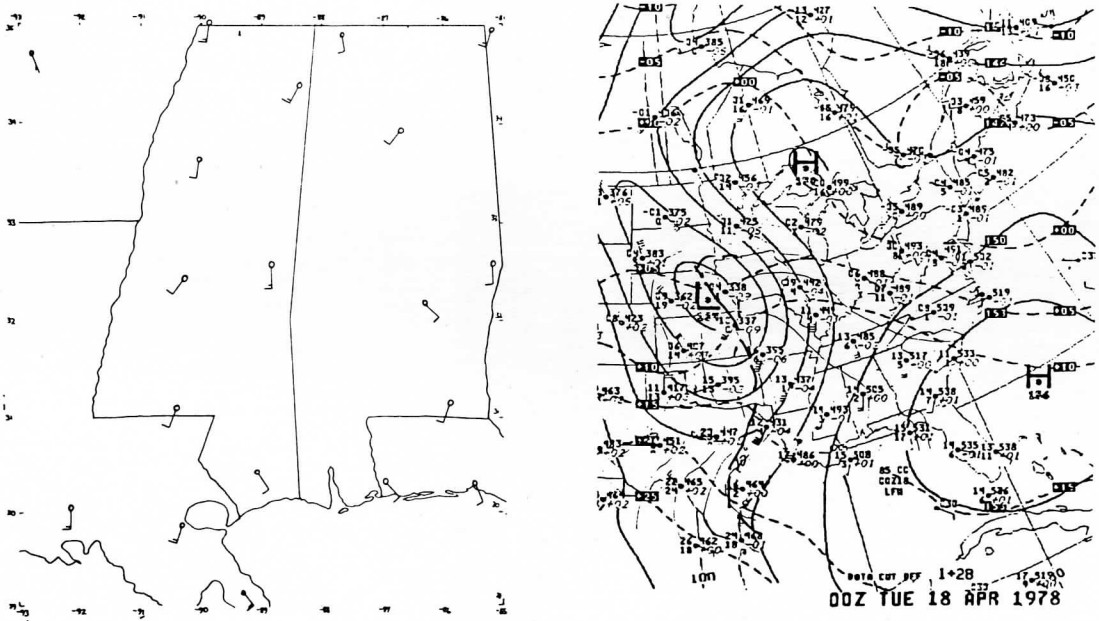

Figure II.7. Left: Surface chart 21Z, 17 April 1978.
Right: 850 mb chart 00Z, 18 April 1978.

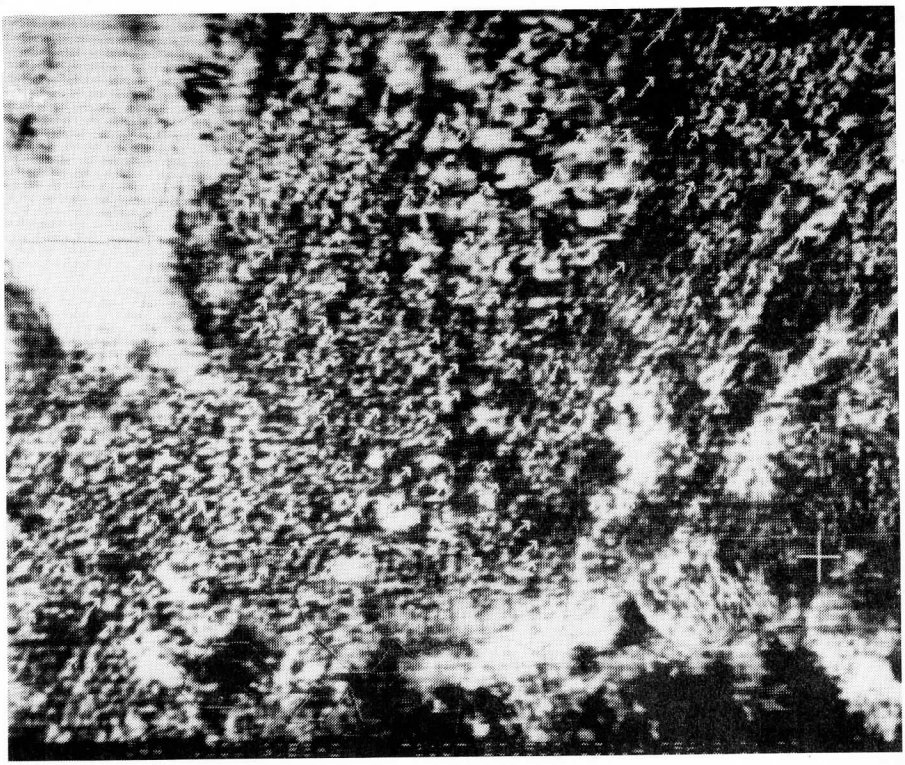

Figure II.8. 2015Z visible satellite image, 17 April 1978, with 15 minute interval wind vectors overlayed.

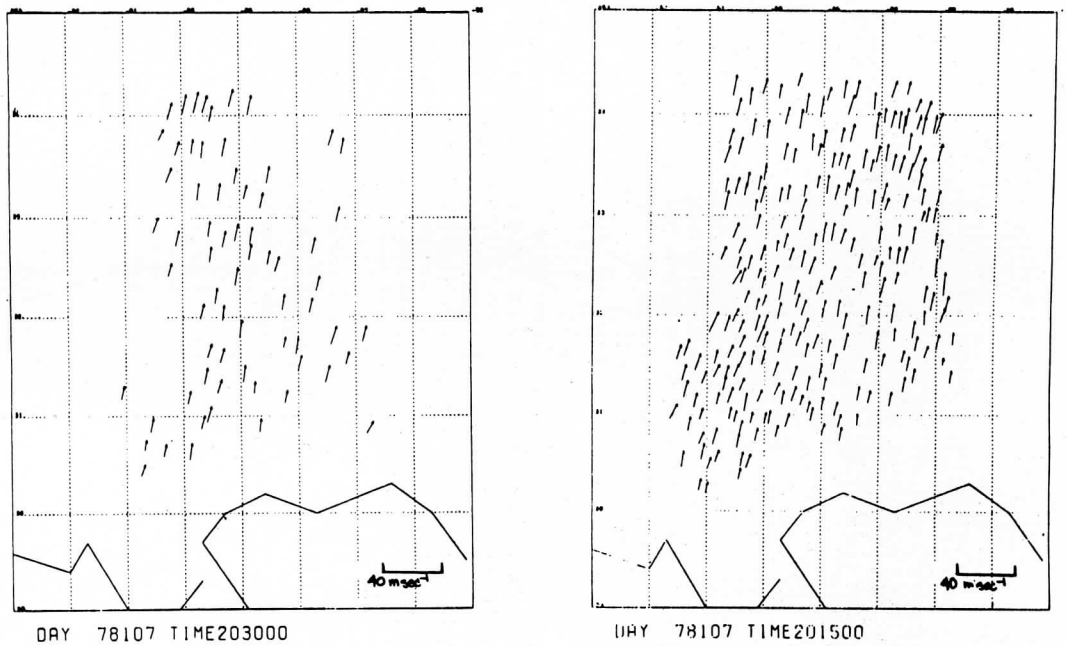

Figure II.9a. Low level wind sets, 17 April 1978. Left: 30 minute interval, 2030Z center. Right: 6 minute interval, 2015Z center

to be the number of vectors produced--over twice as many using a 6 minute interval versus a 30 minute interval. Reducing the time interval to 3 minutes further increases the number of vectors. Figure II.9b shows 3 minute interval winds using a 3 frame sequence, and winds computed using 5 frames, also 3 minutes apart. Granularity errors, discussed earlier, are smaller using a 5 frame sequence because a cloud can be tracked for 12 minutes rather than 6. This difference is so small, though, that it is not noticeable in comparing the two wind sets. However, with a 5 frame sequence the operator was better able to detect true motions, thereby decreasing the time to complete a wind set.

The results for 17 April are displayed in Table II.3. Mean directions, as shown in the windsets, are nearly identical for all time intervals. While clouds were growing and dissipating less rapidly than on 9 April, a four-fold increase in cloud tracers is observed by decreasing the time interval from 30 minutes to 3 minutes. The 6 minute interval produced a comparable number of vectors to the 3 minute interval, and yet took much less operator time to complete. The 6 minute interval is, therefore, a good compromise between wind accuracy and vector coverage, and proved to be optimum for low levels on this day.

20 May 1978

As the 850 mb chart reveals (Figure II.10), a large anticyclone dominates the tracking region on 20 May. Winds are light both at this level and at the surface (Figure II.10). Cumulus cloud lifetimes were longer than on the previous two study days, and no well-organized squall lines or thunderstorms were present (see photo, Figure II.11). Diurnal heating appeared to be chiefly responsible for cloud growth on this day, in contrast to hydrodynamic instability processes forcing vertical motions in the strong southerly flow on both 9 April and 17 April.

Light winds with an anticyclonic circulation show clearly in the 30, 15, 6, and 3 minute interval wind sets (Figures II.12a and II.12b). Because of the longer cloud lifetimes in this region, most clouds tracked using a 3 minute interval could also be tracked with longer intervals (Table II.4).

This table also shows the lightness of the wind field on this day; speeds are smaller by a factor of four than on 9 and 17 April. Three minute interval winds are consistently 1 to 2 $msec^{-1}$ (nearly 50%) stronger than longer interval winds. This systematic difference is opposite the results from 9 April, and may be attributed to the very weak low level flow. Even at full resolution, cloud movements using a 3 minute interval were less than a pixel, producing consistently stronger wind computations.

Streamline and isotach maps have been included for 3 minute and 30 minute interval winds (Figure II.13). The 3 minute interval map reflects greater spatial coverage of vectors than the 30 minute interval map, particularly in the NE part of this region. Inflow into the thunderstorm in the NW section of the map (see also Figure II.11) is captured more completely using 3 minute winds. The usefulness of the short interval winds becomes apparent for

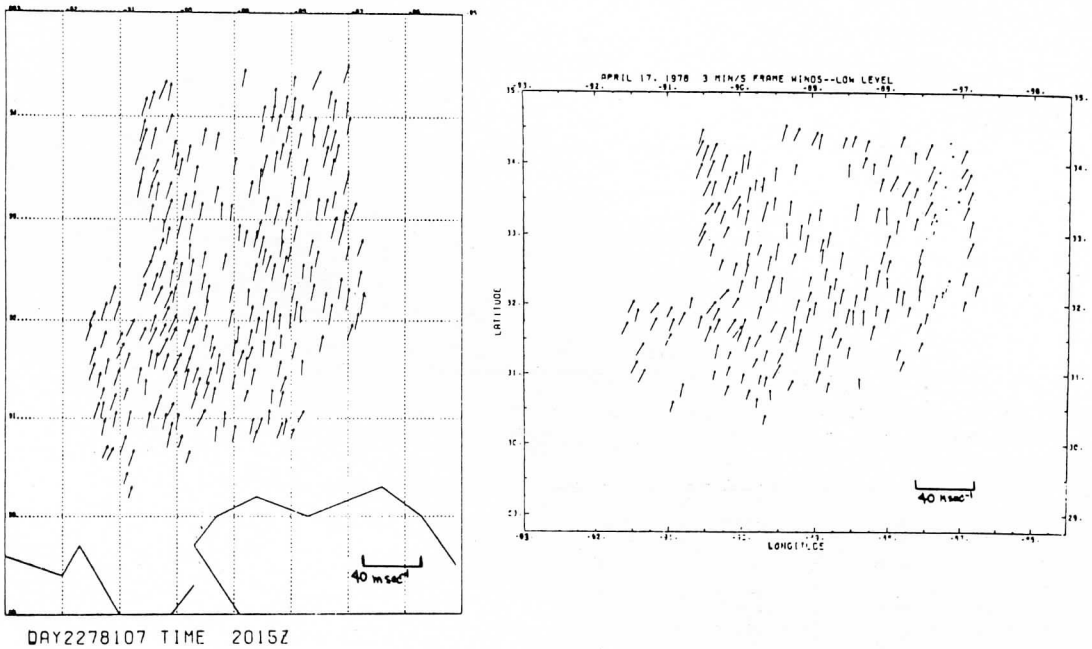

Figure II.9b. 3 minute interval low level wind sets, 2015Z center, 17 April 1978. Left: 3 frame sequence, Right: 5 frame sequence.

Time Int. (min.)	No. of Vectors	Direction (°)		Speed ($msec^{-1}$)	
		Mean	Std. Dev.	Mean	Std. Dev.
30	67	198.9	6.3	11.3	1.4
15	174	193.0	5.4	10.9	1.4
6	246	199.3	6.8	10.9	1.7
3/5 frames	199	196.0	8.2	11.0	1.6
3/3 frames	254	199.6	7.9	12.5	1.8

R M S VALUES ($msec^{-1}$)			
Time Int's. Compared (min.)	Mean U-Comp.	Mean V-Comp.	Mean Resultant Wind
30 min. vs. 15 min.	1.8	4.8	5.1
30 min. vs. 6 min.	2.3	5.5	5.9
30 min. vs. 3 min./ 5 frame	2.3	5.5	5.9
30 min. vs. 3 min./ 3 frame	2.6	6.3	6.9

Table II.3. Cloud tracking results, low level
17 April 1978.

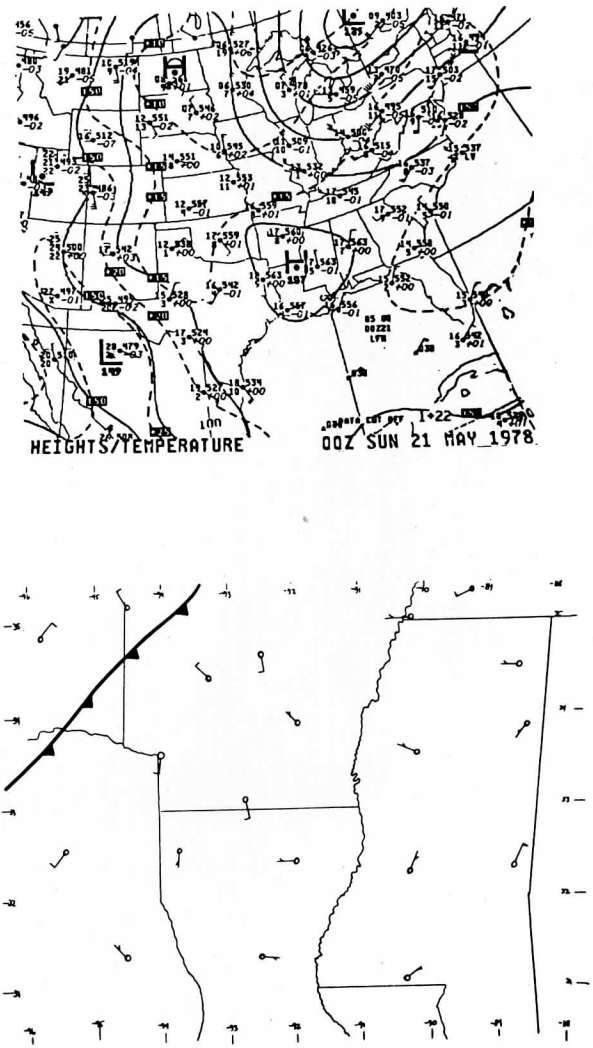

Figure II.10. Top: 850 mb chart 00Z, 21 May 1978.
Bottom: Surface chart 21Z, 20 May 1978.

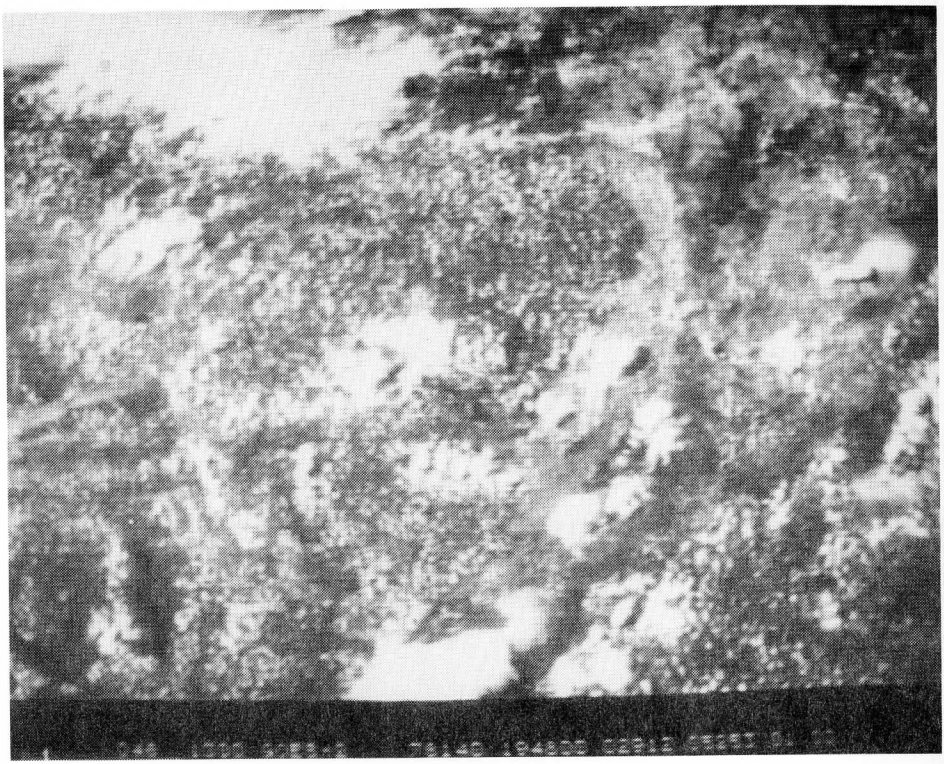

Figure II.11. 1948Z visible satellite image, 20 May 1978.

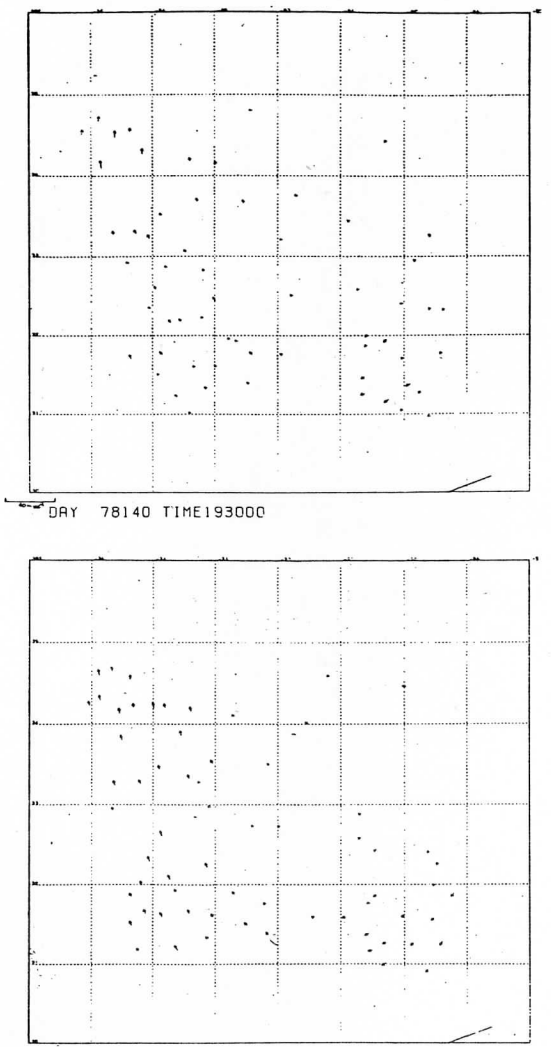

Figure II.12a. Top: 30 minute interval low level wind set, 2000Z center. Bottom: 15 minute interval set, 1945Z center, 20 May 1978.

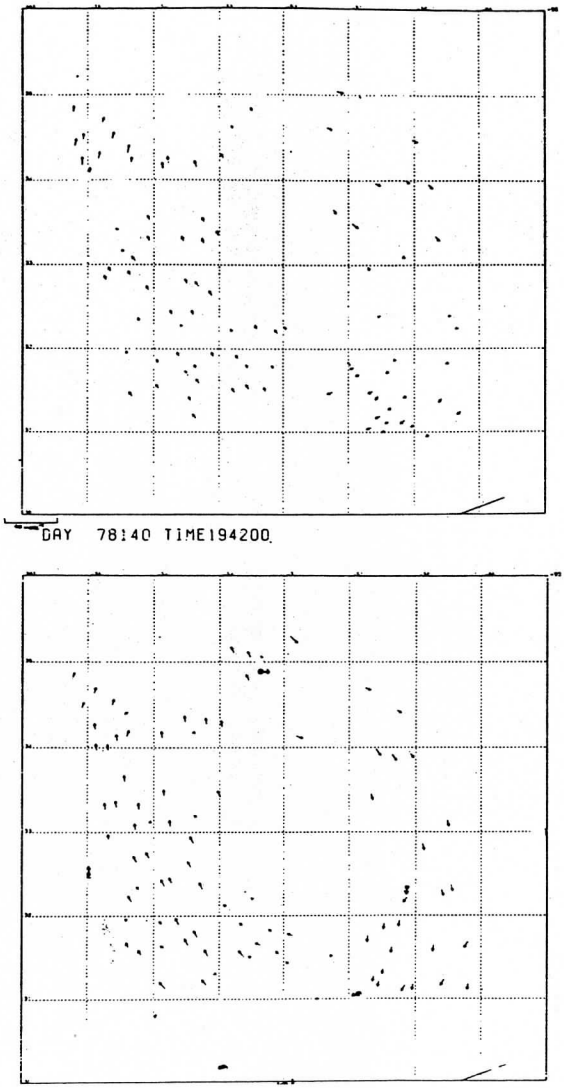

Figure II.12b. Top: 6 minute interval low level wind set, 1948Z center. Bottom: 3 minute interval low level wind set, 1945Z center. Both on 20 May 1978.

Time Int. (min.)	No. of Vectors	Grid Pt. Values	Direction (°)		Speed ($msec^{-1}$)	
			Mean	Std. Dev.	Mean	Std. Dev.
30	61	135	120.0	59.9	3.0	1.1
15	67	148	128.1	61.8	3.3	0.9
6	90	189	153.2	74.1	3.9	1.0
3	89	160	155.9	87.4	4.8	1.3

R M S VALUES ($msec^{-1}$)

Time Int's. Compared (min.)	Mean U-Comp.	Mean V-Comp.	Mean Resultant Wind
30 min. vs. 15 min.	0.7	1.1	1.3
30 min. vs. 6 min.	1.2	1.5	1.9
30 min. vs. 3 min.	1.2	1.9	2.2

Table II.4. Cloud tracking results, low level
20 May 1978.

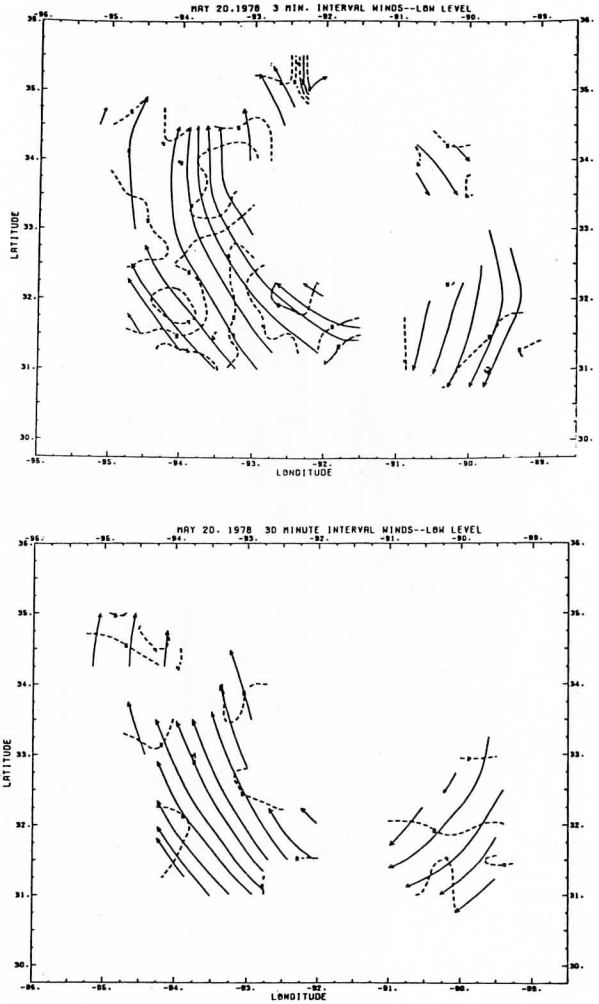

Figure II.13. Streamlines and isotachs from low level winds, 20 May 1978. Top: 3 minute winds. Bottom: 30 minute winds.

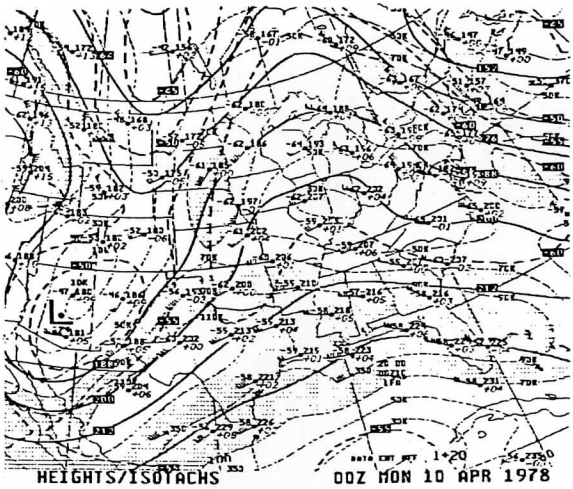

Figure II.14. 200 mb chart. 00Z, 10 April 1978

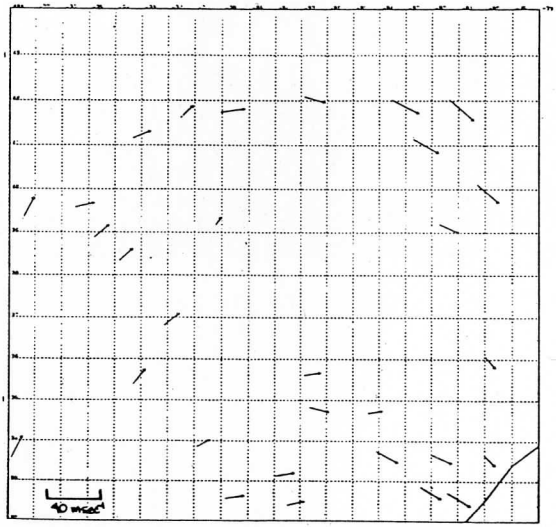

Figure II.15. 30 minute interval cirrus level wind set, correlation tracked. 2000Z center, 9 April 1978.

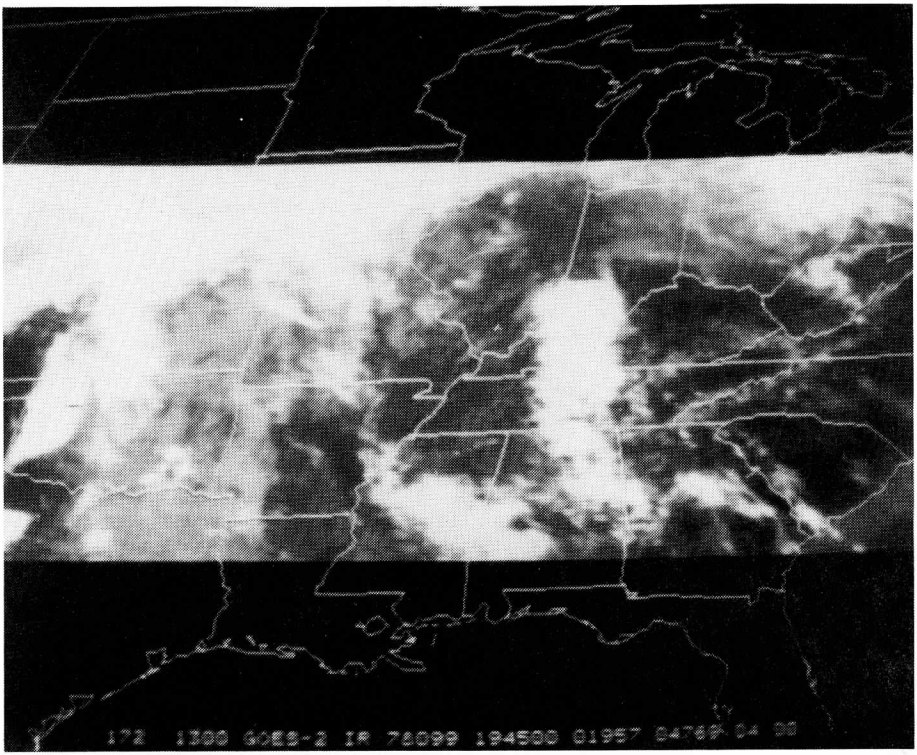

Figure II.16. 1945Z IR satellite image, 9 April 1978

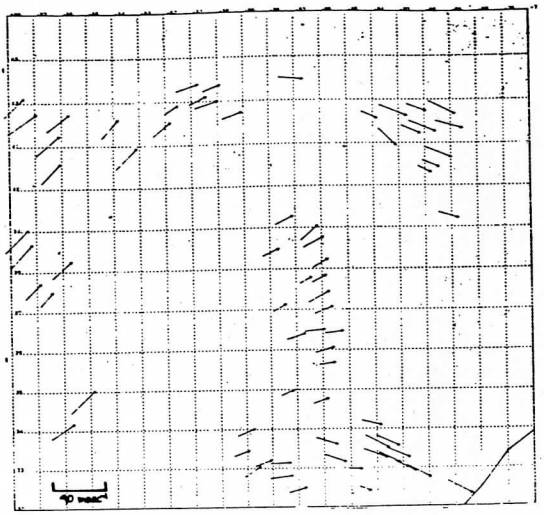

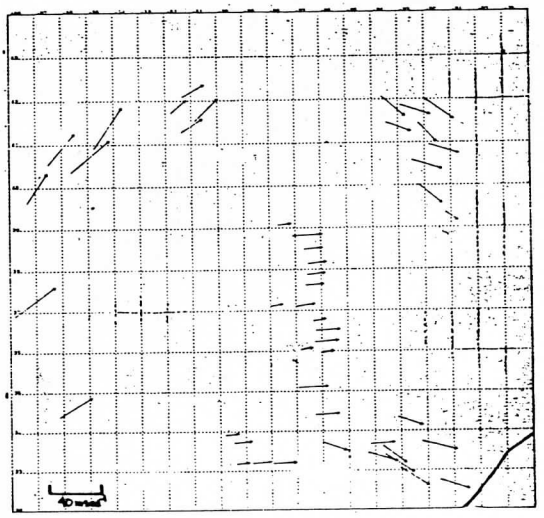

Figure II.17 Cirrus level wind sets (single pixel), 9 April 1978. Top: 30 minute interval, 2000Z center. Bottom: 3 minute interval, 1942Z center.

CIRRUS LEVEL

SINGLE PIXEL TRACKED					
Time Int. (min.)	No. of Vectors	Direction (°)		Speed ($msec^{-1}$)	
		Mean	Std. Dev.	Mean	Std. Dev.
30	90	256.3	22.6	20.1	6.1
15	87	261.2	22.1	23.1	7.3
6	77	257.5	23.3	25.0	7.8
3	65	261.3	23.4	25.5	11.6
CORRELATION TRACKED					
Time Int. (min.)	No. of Vectors	Direction (°)		Speed ($msec^{-1}$)	
		Mean	Std. Dev.	Mean	Std. Dev.
30	32	262.9	31.7	16.7	3.9
15	32	254.8	28.6	15.2	3.7
6	32	260.7	32.5	18.2	6.2
3	14	249.4	14.5	18.1	6.8

R M S VALUES ($msec^{-1}$) (From Single Pixel Tracked Winds)			
Time Int's. Compared (min.)	Mean U-Comp.	Mean V-Comp.	Mean Resultant Wind
30 min. vs. 15 min.	4.0	2.1	4.5
30 min. vs. 6 min.	4.3	2.3	4.9
30 min. vs. 3 min.	3.7	2.1	4.2

Table II.5. Cloud tracking results, cirrus level 9 April 1978.

mesoscale processes such as low level convergence in thunderstorm regions and minor directional changes in the wind, as are depicted in these streamline maps. Caution must be used, though, when determination of wind speed is important, as short interval winds may be too strong.

B. Cirrus Level Winds

Two days were selected for tracking cirrus: 9 April and 20 May of 1978. In general, cirrus have longer lifetimes and thus are found to be more easily trackable over longer intervals than are low level cumulus. The results for each day follow.

9 April 1978

The 200 mb chart for 00Z, 10 April (Figure II.14) shows strong ridging from the Gulf Coast to the Great Lakes. Evidence of the subtropical jet exists over the southern states and along the Gulf Coast, with 100 kts (55 $msec^{-1}$) reported over the Florida panhandle. This zone of maximum winds can also be seen in the 2030Z IR satellite photo (Figure II.16), with cirrus circulating around the ridge.

Figure II.15 presents wind vectors over this region, computed using correlation tracking on IR images with a 30 minute time interval. The following two wind sets (Figure II.17) show vector fields computed using single pixel tracking and visible images with both 30 and 3 minute intervals, respectively. In contrast to low level tracking, it was found that the 30 minute interval produced the most vectors, as the figures show. It also took much less time to track the cirrus using a 30 minute interval. The 3 minute interval often produced vectors inconsistent with the rest of the field, making the editing process longer and more tedious.

In Figure II.17 (bottom), one can see directional errors using a short interval sequence, particularly in the northeast and southeast sections of the map. Granularity errors from using single pixel tracking and a 3 minute interval are noticeable in wind speeds, also. Three minute winds are consistently stronger here, as was found on 20 May at low levels.

Table II.5 summarizes the results for both single pixel and correlation tracking on this day. Nearly 3 times more vectors were produced using single pixel than correlation. The operator had difficulty identifying distinct, trackable features in the cirrus using correlation tracking. In addition, it took nearly twice as long to produce the correlation wind sets, and was nearly impossible to use correlation with a 3 minute time interval. Not only were cloud features difficult to identify, but they moved so little in 3 minutes that correlation algorithms often computed zero wind speed, or erroneous wind directions.

As was shown in Figure II.17, the 3 minute interval winds are 5 $msec^{-1}$ greater than 30 minute interval winds, using single pixel methods. Directions are fairly consistent in all computations. RMS values reveal close agreement between all time intervals, showing that cirrus level tracking is less time

interval-dependent than low level tracking.

20 May 1978

The flow at all levels was weaker on this day than on 9 April. At 200 mb (Figure II.18), there is a wind maximum of 90 kts (45 $msec^{-1}$) over Illinois at 00Z on 21 May. A ridge extends from Louisiana to the Dakotas, giving SW flow over the Southwest. Evidence can be found for the subtropical jet over northern Mexico, supplying the needed upper level support for a large area of thunderstorms and severe weather over Texas. Figure II.19, the IR picture for 2030Z, shows this thunderstorm area, and the cirrus blow-off to the east.

In single pixel tracking, visible images of 2.4 km resolution with IR images on the opposite frames were used. The 3 minute interval wind set is shown in Figure II.20a. To the right, also in Figure II.20a, is the 3 minute interval wind set produced using full resolution visible images, with 200 mb radiosonde winds also shown. The 3 minute/2.4 km wind set again has consistently stronger winds, but by reducing the spatial resolution to 1.2 km, wind speeds are slower and compare more favorably with radiosonde winds. Significantly more vectors with a slightly greater spatial coverage are also produced when full resolution images are used. Both sets show the jet at approximately 40°N, although the wind directions appear to be more realistic using full resolution images, as minor directional differences are noted which the 2.4 km images did not catch.

Thirty minute interval wind sets are shown in Figure II.20b. The one on the left was computed using single pixel and 2.4 km resolution visible images, while the one on the right was computed using IR frames and the correlation method. A much smoother field is produced with a 30 minute interval than with either of the 3 minute intervals, and the jet to the north is well depicted. This set took only 2 hours to produce, while the 3 minute/full resolution set took nearly 10 hours.

The correlation-produced wind set (Figure 20b) shows more of the problems in tracking cirrus using correlation: spatial coverage of vectors is quite limited, and wind directions are in error in several locations.

The summary of all cirrus level tracking on 20 May is presented in Table II.6. The 30 minute interval winds were the slowest, and standard deviations of speed were least. All time intervals produced similar numbers of vectors except when the spatial resolution was improved, nearly doubling the number. Five times as many vectors were computed using single pixel rather than correlation, and, again, the correlation method was nearly impossible using the shortest intervals. RMS values show closest correspondence between 30 and 15 minute intervals, with the larger differences between 30 and 3 minute intervals attributable to the consistently stronger wind speeds using the short intervals, and the greater spatial coverage of vectors using full resolution images.

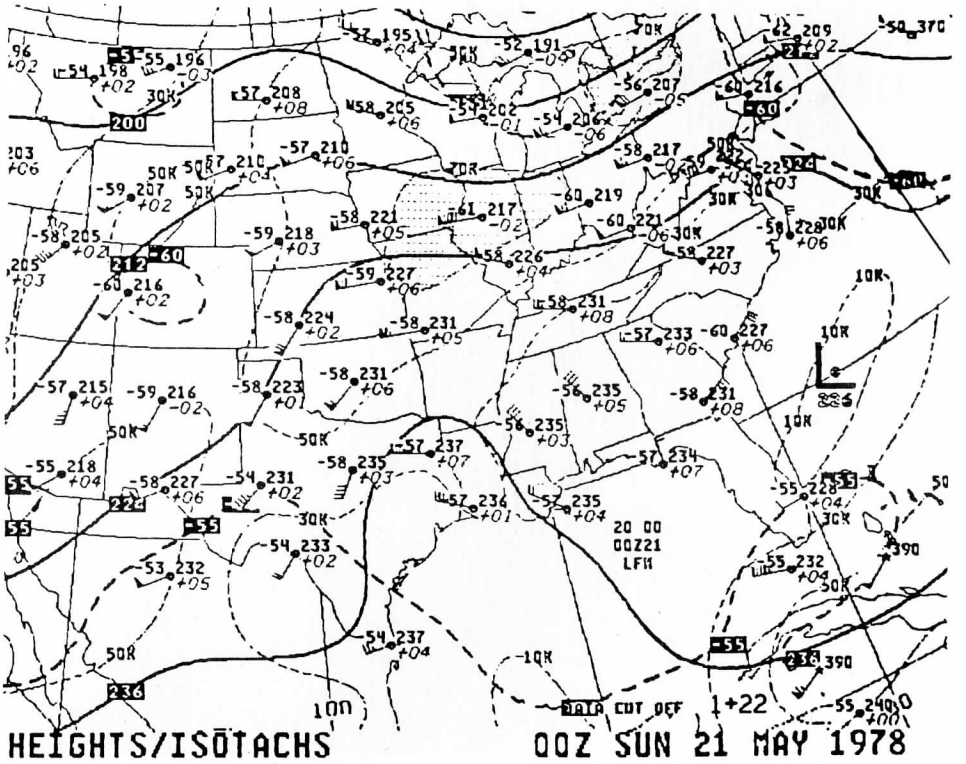

Figure II.18. 200 mb chart 00Z, 21 May 1978.

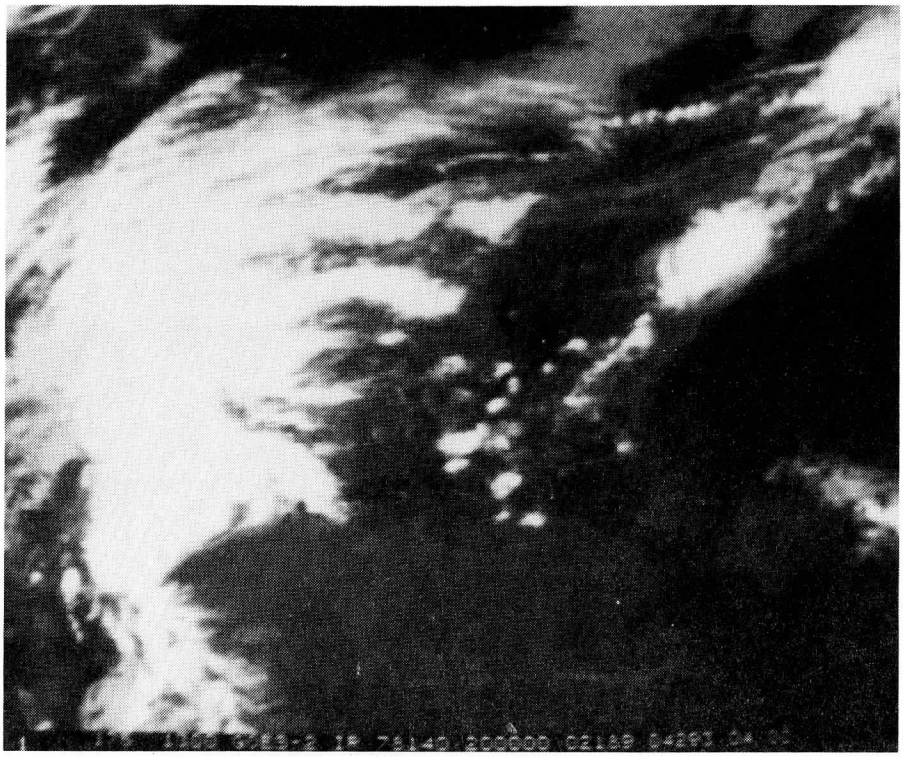

Figure II.19. 2000Z IR satellite image, 20 May 1978.

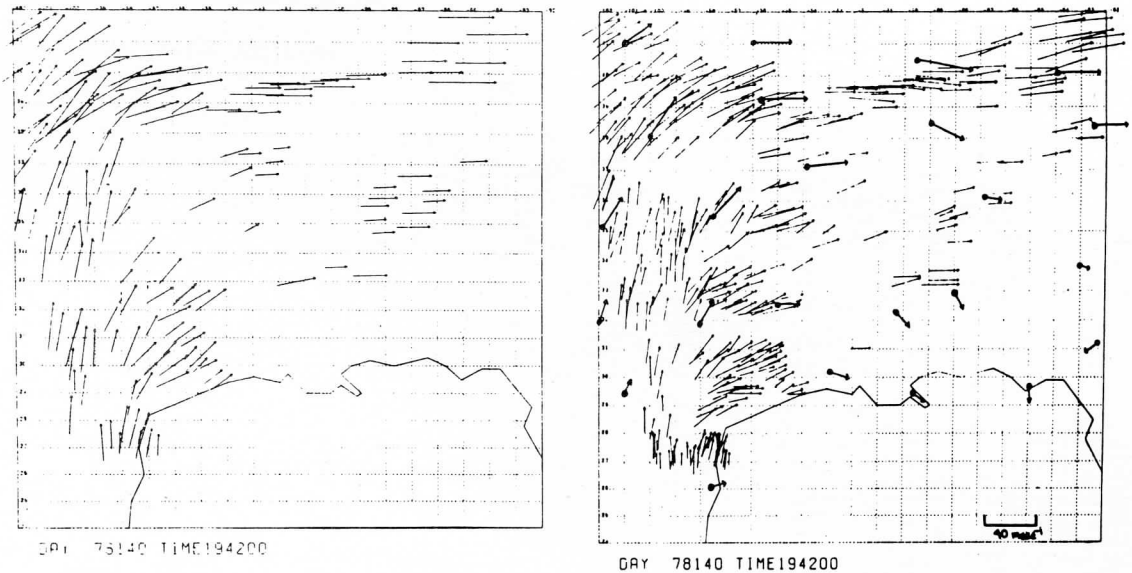

Figure II.20a. 3 minute interval cirrus level wind sets, 1945Z center, 20 May 1978. Left: 2.4 km res. used. Right: 1.2 km res. used, with 200 mb sonde winds as dark arrows.

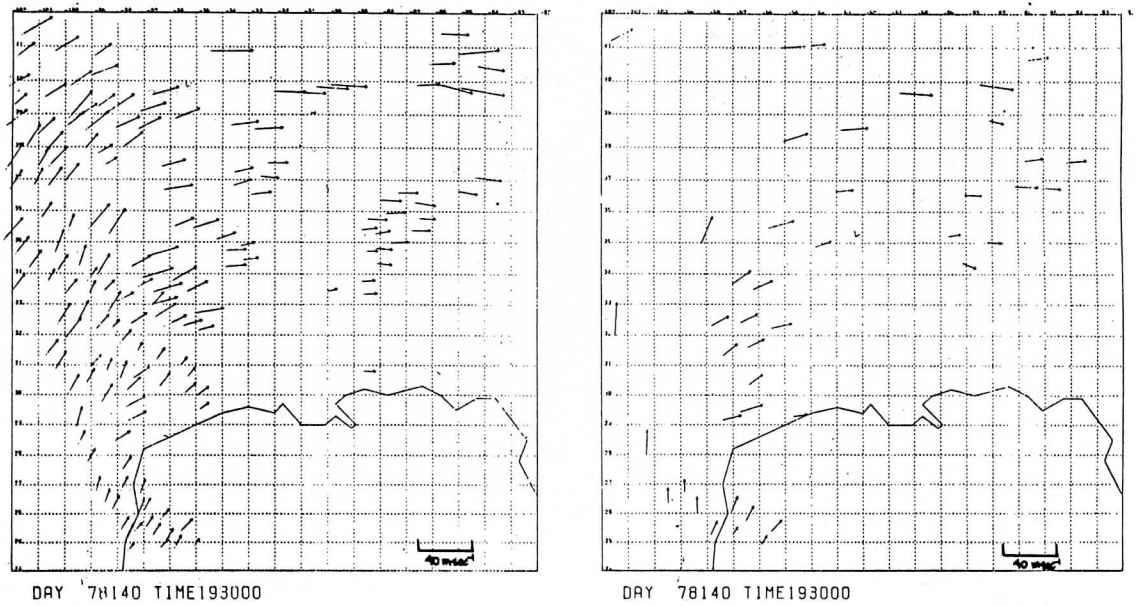

Figure II.20b. 30 minute interval cirrus level wind sets 2000Z center, 20 May 1978. Left: Single pixel tracked, using 2.4 km res. vis. images. Right: Correlation tracked, using 9.4 km res. IR images.

CIRRUS LEVEL

SINGLE PIXEL TRACKED					
Time Int. (min.)	No. of Vectors	Direction (°)		Speed ($msec^{-1}$)	
		Mean	Std. Dev.	Mean	Std. Dev.
30	201	231.6	24.7	16.4	5.0
15	207	226.0	25.2	19.2	5.8
6	203	227.0	25.3	24.4	6.4
3/2.4 Km	181	226.7	30.3	31.8	9.5
3/Full Res.	376	228.4	29.5	23.4	7.2
CORRELATION TRACKED					
Time Int. (min.)	No. of Vectors	Direction (°)		Speed ($msec^{-1}$)	
		Mean	Std. Dev.	Mean	Std. Dev.
30	47	237.6	32.2	16.0	5.7
15	42	237.0	32.3	17.7	5.7
6	24	255.9	24.4	20.7	7.4
3	19	247.5	31.1	21.1	9.6

R M S VALUES ($msec^{-1}$)			
Time Int's. Compared (min.)	Mean U-Comp.	Mean V-Comp.	Mean Resultant Wind
30 min. vs. 15 min.	5.2	3.3	6.1
30 min. vs. 6 min.	4.8	4.8	6.8
30 min. vs. 3/2.4 Km	6.5	5.8	8.7
30 min. vs. 3/Full Res.	8.3	5.7	10.1

Table II.6. Cloud tracking results, cirrus level 20 May 1978.

IV. CONCLUSION

Rapid scan imagery provides a basis upon which intracomparisons between cloud-tracked winds computed using images with different time and space resolutions were made. Tracking was performed on both low level and cirrus-level clouds on several synoptically different days.

Low level cumulus clouds over land have lifetimes which vary in length (5 to 30 minutes) and are dependent upon the meteorological processes causing their existence. These differences in cloud lifetimes directly affect cloud tracking results. On days of rapid cloud growth and dissipation, nearly 10 times as many cloud winds were produced using images spaced 3 minutes apart compared to those spaced 30 minutes apart. Average wind speeds were slightly less (1 to 2 $msec^{-1}$) and the spatial coverage of vectors significantly greater (6 times as many grid points) for 3 minute interval winds on these days. On days with longer cloud lifetimes, this difference was much less, with vector numbers nearly the same, and wind speeds slightly stronger for the 3 minute interval. Hence, in general, for low level cloud tracking, slower wind speeds and longer cloud lifetimes cause smaller differences between long and short intervals in terms of numbers of wind vectors produced. In addition, the effects of image granularity are also enhanced. This granularity problem is reduced if a 5 frame sequence of images is used rather than 3. However, few differences were found between 5 frame and 3 frame wind fields, except that the operator found cloud motions easier to detect while tracking was being performed.

One of the most important assets of winds from rapid scan images is their ability to describe mesoscale features during severe weather outbreaks. Not only are more wind vectors produced, but often mesoscale flow patterns are caught which 15 or 30 minute interval winds miss. Confluence into a thunderstorm was well depicted in a streamline map using 3 minute interval winds, while 30 minute interval winds showed no confluence.

The differences between short and longer interval winds decreased when tracking cirrus. Cirrus cloud lifetimes are an order of magnitude greater than those for low level cumulus and therefore could be tracked using 30 minute interval images. Cloud tracer numbers and spatial coverage were nearly the same for all intervals used. For cirrus level tracking (and low level tracking on days of slow cloud growth), the longer the interval between images, the easier it was for an operator to discern cloud motions, resulting in decreased wind set completion time. A 3 minute interval cirrus wind set took up to 4 times as long to complete as a comparable 30 minute interval set.

In general, a short interval between images was found poor for cirrus-level tracking. Average 3 minute interval wind speeds were up to 10 $msec^{-1}$ stronger than 30 minute interval and radiosonde speeds, and short interval wind directions were often in error. As a result, a much smoother wind field can be produced using 30 minute interval winds than 3 minute winds, at the cirrus level. Single pixel rather than correlation tracking worked best for tracking cirrus, since cirrus shape and brightness lacks distinctness. Nearly 3 times as many cirrus clouds could be tracked using single pixel rather than correlation. As a rule, then, single pixel tracking with a 30 minute interval

should be used on all cirrus clouds.

A change in the spatial resolution of the images produced significant differences in cloud winds. At the cirrus level, the number of wind vectors produced increased twofold (376 vs. 181) as the space resolution was decreased from 2.4 to 1.2 km, for 3 minute images. Spatial coverage of vectors also increased with this improvement in resolution, reaffirming that spatial as well as temporal resolutions are important in cloud tracking. The value of added wind vectors and greater spatial coverage of winds is well established, particularly in model initialization (Rodgers, et al., 1979). Short interval winds may be a valuable addition for model input, particularly on a mesoscale level over land.

The results of this study show that different tracking procedures must be used for different types of clouds. For cirrus clouds, with their longer lifetimes, the 30 minute interval with single pixel tracking proved to be most accurate and efficient in all cases. Low cloud results proved differently. Before selecting a time interval for low cloud tracking the synoptic situation should be examined carefully. Viewing an image sequence with a 30 minute interval (to obtain a general picture of low level flow) always proved valuable. Cloud lifetimes can be estimated rather quickly by viewing a sequence of pictures, determining whether a short interval between images will prove valuable. In short, getting a "feel" for the situation where one is tracking before actual tracking is performed can often expedite the process, and a temporal resolution can be selected which will give the meteorological information one is most interested in. Overall, low level tracking using a 6 minute interval is a good compromise between wind accuracy and vector coverage, and should be used if a "standard" time resolution is to be selected for detection of low level cloud motions from satellite images.

It is recommended, therefore, that different time intervals be used for cirrus level and lower level clouds. For cirrus, the conventional 30 minute interval is optimum. A 30 minute interval produces up to 40% more vectors than the 3 minute interval, takes less time to track, and produces a much smoother wind field. It was also surprising to find that single pixel methods produced better results than correlation methods. Research into correlation methods presently used is recommended. At low levels, a shorter time interval (around 6 minutes) works best. On days of rapid convection up to 10 times as many clouds can be tracked using a 3 or 6 minute time interval over the coventional 30 minute interval. Mesoscale flow patterns are also better depicted with rapid scan images. This implies that a change should be made in the satellite scan time for improved tracking of low level clouds; a reduction from 30 minute to a 6 to 10 minute scan over a region is recommended if improvement in low level cloud-tracked winds is sought. Research into the feasibility of such a change should be conducted so that satellite images with a frequency greater than that of every 30 minutes could be taken on more than just a few select "severe weather days" during the year.

REFERENCES

Bauer, K.E., 1976: A comparison of cloud motion winds with coinciding radiosonde winds. Mon. Wea. Rev., 104, 922-931.

Chang, Y.M., J.J. Tecson and T.T. Fujita, 1973: METRACOM system of cloud-velocity determination from geostationary satellite pictures. SMRP Res. Paper 110, 29pp.

Chatters, G.C. and V.E. Suomi, 1975: The applications of McIDAS. IEEE Transactions of Geoscience Electronics, GE-13, 137-146.

Fujita, T.T., E.W. Pearl and W.E. Shenk, 1975: Satellite tracked cumulus velocities. J. Appl. Meteor. 14, 407-413.

Hasler, A.F., W.E. Shenk and W.C. Skillman, 1976: Wind estimates from cloud motions: Phase I of an in situ aircraft verification experiment. J. Appl. Meteor. 15, 10-15.

_____, 1976: Wind estimates from cloud motions: Results of phases I, II, and III of an in situ aircraft verification experiment. J. Appl. Meteor. 16, 812-815.

Houghton, D.D. and T.A. Wilson, 1976: Mesoscale wind fields for a severe storm situation determined from synchronous meteorological satellite (SMS) cloud observations. In Proceedings of the Ninth Conference on Severe Local Storms, Amer. Meteor. Society, 187-192.

Houghton, D.D. and D.K. Lee, 1977: Mesoscale wind fields for the May 6, 1975 Omaha tornado situation derived from SMS cloud observations. Reprint, Tenth Conference on Severe Local Storms, Amer. Meteor. Society, 16-21.

Hubert, L.F. and L.F. Whitney, Jr., 1971: Wind estimation from geostationary satellite pictures. Mon. Wea. Rev., 99, 665-672.

Krause, G.J., 1978: On the determination of height variations in overshooting thunderstorms from geostationary satellite images, M.S. Thesis, University of Wisconsin-Madison, 65pp.

Lilly, D.K., ed., 1978: SESAME 1979 working group reports and field plans, Severe Environmental Storms and Mesoscale Experiment, U.S. Dept. of Commerce, 63pp.

Maddox, R.A., A.J. Negri and T.H. Vonder Haar, 1977: Analysis of satellite derived winds for April 24, 1975. Reprint, Tenth Conference on Severe Local Storms, Amer. Meteor. Soc. 54-60.

Mancuso, R.L. and R.M. Endlich, 1973: User's Manual, Wind Editing and Analysis Program: Spherical Grid. WEAP-1A, Stanford Research Institute.

Mosher, F.R., 1978: Cloud drift winds from geostationary satellites. Atmospheric Technology, No. 10, 53-60.

Rodgers, E., R.C. Gentry, W. Shenk and V. Oliver, 1979: The benefits of using short-interval satellite images to derive winds for tropical cyclones. Mon. Wea. Rev., 107, 575-584.

Smith, E.A., 1975: The McIDAS System. IEEE Transactions of Geoscience Electronics, GE-13, 123-136.

Suchman, D. and D. Martin, 1976: Wind sets from SMS images: An assessment of quality for GATE. J. Appl. Meteor., 15, 1265-1278.

Tecson, J.J., T.A. Umenhofer and T.T. Fujita, 1977: Thunderstorm-associated cloud motions as computed from 5-minute SMS pictures. Reprint, Tenth Conference on Severe Local Storms, Amer. Meteor. Soc., 22-29.

Wilson, T.A., 1976: The determination of mesoscale horizontal and vertical wind fields from SMS-I satellite observations. M.S. Thesis, University of Wisconsin-Madison, 124pp.

Young, J.T., 1976: Navigation of geostationary images. In Proceedings of the Symposium on Meteorological Observations from Space: Their Contributions to the First GARP Global Experiment, Philadelphia, PA. COSPAR Working Group 6, NCAR, Boulder, CO., 198-200.

LIST OF FIGURES

LIST OF TABLES

CHAPTER III

ON THE DETERMINATION OF HEIGHT VARIATIONS IN OVERSHOOTING THUNDERSTORMS FROM GEOSTATIONARY SATELLITE IMAGES

Gregory J. Krause

ABSTRACT

The updrafts of vigorous thunderstorms often penetrate the tropopause, resulting in cloud features that overshoot the anvil level. This study focuses on determining if height variations of these overshooting tops can be detected in rapid-scan (3 minute interval) geostationary satellite images. The overshooting top of a single-cell thunderstorm is an individual protruding dome, while a multi-cell storm's top has a close group of domes. These features are identified in the visible images by the shadows domes cast in the afternoon sun, so the exact positions of storm tops are determined. By overlaying the infrared (IR) data on the visible image it can be determined if the temperature of each top is resolved.

With the IR resolution of the SMS-1 satellite, 48% of the tops in this study can be uniquely identified as individual cold regions, colder than the surrounding anvil temperature. Assuming positive lapse, temperature changes in these cold regions indicate relative height changes between images. In the 30 storms with overshooting tops that could be identified in the IR data, 74 periods of ascent or descent are observed. These results are then examined to determine if severe weather is related to the height variations of these storm tops. It is found that 14 of 15 severe events occurred beneath an overshooting thunderstorm. Hail events and tornado/funnel reports both have storm tops that ascend about 15 minutes before the event. However, only tornado/funnel storms show a subsequent descent of the top near the event's reported time.

I. INTRODUCTION

The relationship between the height of thunderstorm tops and severe weather had been studied from various platforms. Donaldson (1960) and Bonner & Kempler (1971) are among the many investigators who have studied radar echo heights. They found that the probability of hail or tornadoes increased greatly when storms penetrated the tropopause. Remick (1971) employed terrestial photogrammetry in observing Alberta hailstorms. Some of these storms had overshooting features up to 3 kilometers above the anvil. Airborne photogrammetry by Fujita (1974), Umenhofer (1975), and Pearl *et al.* (1975) also showed a correlation between anvil protrusions and severe weather occurrences beneath them. In this paper, the use of another platform is explored. The heights of overshooting thunderstorms are determined from a geostationary satellite and used in studying severe weather in a case study.

An overshooting top is a cloud feature that protrudes above the relatively flat anvil of a well-developed storm. These features are called "overshooting tops" because various investigators have proposed that they represent the top of an updraft that overshoots the anvil. The direct connection between overshooting features and sub-anvil updrafts is presented in conceptual models of thunderstorms by Browning & Ludlam (1962), Newton (1963 & 1966), and Fankhauser (1971). Figure III.1 is a model from Fankhauser's paper, showing how the protruding top is a result of the main updraft.

In an overshooting updraft, a positively bouyant air parcel rises until it encounters a very stable environment, the tropopause. This level is called the "crossover point" (Fujita, 1972). Momentum carries the parcel above this point, but the parcel becomes strongly negatively bouyant. Therefore, the parcel reaches a peak height, and this appears as an overshooting cloud feature. The height of an overshooting top thus strongly depends on the parcel's updraft speed.

The advent of the geostationary satellite era provided a new view of anvil topography. These satellites are stationary in their orbit, remaining above one point on the earth's equator, thus allowing a region to be continuously monitored.

With ATS-3 images, Fujita (1972) calculated the above-anvil heights of overshooting tops by measuring the length of the shadows they cast on the anvil surface. Shadow length is very sensitive to the top's height with the sun angle being very low. Figure III.2, from Fujita's work, shows that distinct tops are the signature of individual storms in a large anvil cloud. In two cases, tornadoes were reported just after a nearby top had collapsed, suggesting the importance of studying the growth and decay of the overshoots. Fujita concluded that closer investigation of overshooting features is necessary to determine resolution criteria for future satellite monitoring of these features.

In 1972-1974 the nature of tops was studied with airborne photography and measurements from Lear jet flights. Results were documented by Fujita (1974), Umenhofer (1975), and Pearl et al. (1975). They found tops to be usually bubble-shaped, from 3 to 10 miles in diameter, with the majority visible above the anvil for periods of about 10 to 30 minutes. Above-anvil heights vary up to 3 km and the tops are colder than the anvil surface. The name given to overshooting tops with these features is DOME.

The dome itself has a finer structure of rapidly changing features called TURRETS, as shown in Figure III.3. These are smaller (up to 1 mile diameter) bubbles within the dome, and their rising and collapsing cycle usually lasts about 2 to 4 minutes. This suggests that turrets represent individual bouyant air parcels in the general updraft stream. Fujita concluded that the conglomeration of turrets, the dome, is the above-anvil protrusion of a single-cell thunderstorm, as described by Byers and Braham (1949). In high resolution satellite data, Fujita theorized that domes would appear as small cold regions in infrared (IR) maps of anvil surface temperatures. Temperature changes of such regions would reflect height variations of the dome, and thus be a measure of updraft intensity of an individual thunderstorm.

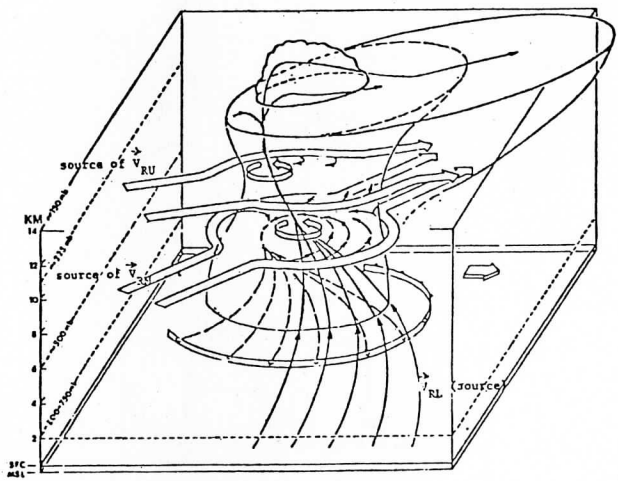

Figure III.1. Model of a severe thunderstorm (Fankhauser, 1971).

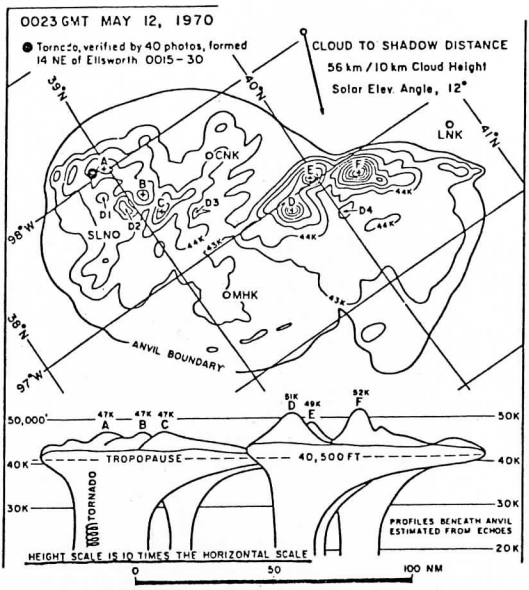

Anvil-top topography of Salina cloud when a tornado verified by 40 photos formed near Ellsworth. The anvil top was contoured for every 1000 ft. using the cloud-shadow relationship. Contours designated by arrows and letter D are shallow depressions of the anvil top.

Figure III.2. Overshooting thunderstorms on 12 May 1970 anvil top topography determined by shadows of overshooting features in visible ATS satellite images (Fujita, 1972).

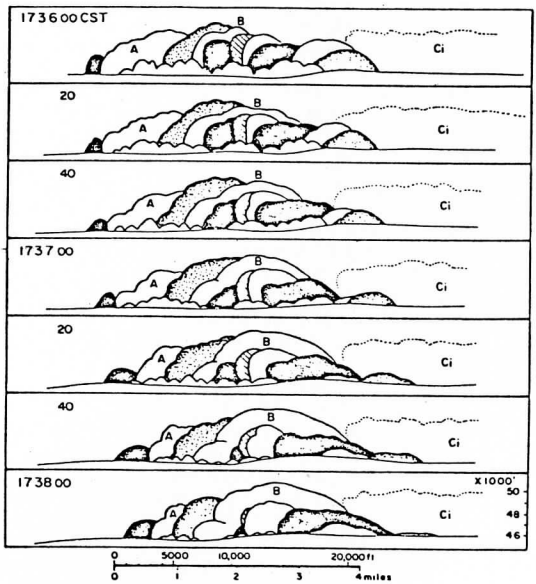

Figure III.3. Dome structure, showing a number of turrets in various stages of overshooting (Fujita, 1974)

With the Synchronous Meteorological Satellite (SMS-1), the high spatial resolution requirement is satisfied.

In this paper, SMS-1 visible and IR data will be used to study dome characteristics in a case study. Using visible data, a method of delineating domes in a large region of overshooting activity will be devised. The main goal is to then see if the domes do appear as unique cold regions in the IR data as Fujita (1974) suggested. Height variations of the domes can then be determined from their temperature changes. Finally, the relationship between severe weather events and height variations of their parent storm's domes will be examined.

II. METHOD

The data for this study is described in the first part of this section. Techniques for identifying domes in the visible images and determining their IR temperatures are then presented. These techniques will be illustrated in a portion of the data set. Finally, several special limitations imposed on the method by the particular data set used will be discussed.

A. Data

The characteristics of domes, as determined by Fujita, were discussed in the introduction. This section shows that the SMS-1 data used in this study, is of sufficient resolution to study these features. The satellite's visible and IR channel resolutions are 1/2 & 4 miles respectively at the subsatellite point. This point is at 0°N & 75°W for SMS-1, so the sensors' de facto resolution decreases to approximately 3/4 & 6 miles when viewing the southern U.S. The visible channel "sees" all domes, and only the smaller ones escape detection in the IR.

The highest temporal resolution for satellite images became available in 1977 with the institution of rapid-scan days, when SMS-1 did limited area scans three minutes apart. This is sufficient to examine life cycles of domes. There were 11 rapid-scan days in 1977 as part of the Severe Environmental Storms and Mesoscale Experiment (Kreitzberg, 1978).

In 1977 rapid-scan SMS-1 data was archived at the University of Wisconsin Space Science and Engineering Center on its McIDAS computer (Man Computer Interactive Data Access System, see Smith 1975). The system can also display the images and do quantitative analysis of the digital data. Images from 1700Z 5 May to 0100Z 6 May provide the data base for this study.

B. Identifying domes in visible images

Shadow identification is the basic means of investigating overshooting activity in visible images. Software in the McIDAS system aids this process in several ways. Image blow-up magnifies the picture on the video monitor to afford an apparent close-up view. A filtering program accentuates brightness

values that contrast with their immediate surroundings. For example, a dome's shadow is made even darker, thus making it more visible to the naked eye. Both of these techniques are used in making the images that appear in Figure III.4. The area is just north of Midland, Texas and the images are at 2000Z and 2009Z (1400 & 1409 CDT).

Based on Fujita's findings, the distinct shadows marked numbers 2, 4, and 6 in the 2009Z image are caused by a dome, evidence of a single-cell storm beneath the anvil. Meanwhile the area designated by a 1 consists of a close group of shadows. Conceptually, this is the sign of a bumpy region, several domes very close to each other.

A preliminary examination of all the visible images revealed that the occurrence of several domes in a close group was a common feature, as common as single domes. Therefore, a subjective classification scheme was devised to identify these dome characteristics on this day, presented in Table III.1. The occurrence of closely grouped domes is evidence of a multi-cellular thunderstorm. This can be seen upon examining the description of such a storm in the work of Byers and Braham (1949). In their model, the downdraft of a single-cell storm in the mature stage may touch off new convective cells in its immediate vicinity. Figure III.5 is a multi-cell storm they observed. In such a storm two or more updrafts could penetrate the anvil simultaneously, their domes yielding a close group of shadows similar to those of area 1 in the 2000Z image. An average diameter of the multi-cell storms in their study was about 10 miles. Therefore, this is chosen as the diameter for a multi-cell storm top in the visible classification scheme in Table III.1.

On 5 May, shadows became apparent in the visible images around 1900Z (1300 CDT). The classification technique is used on each image from 1900 to 2330Z, at which time a technical problem results in missing images. The positions of overshooting features are plotted on charts. A series of single-cell (SC) or multi-cell (MC) tops that progress reasonably in time and space is called an individual storm, and its path will be called a storm track. Image times on this day are 00, 09, 12, 15, 18, 21, and 24 minutes after the hour and half hour. At 03, 06, and 27 minutes after the hour and half hour, pictures were not taken, since the satellite was in the process of being recalibrated for full hemispheric scans on each half hour. Only storms lasting 9 minutes or longer are monitored in this study, to avoid discrimination during the data gaps. An example of this technique is given in a latter section.

In summary, the visible classification technique identifies the tops of individual storms in either a single-cell (SC) or multi-cell (MC) stage. The overshooting tops of these storms are individual domes and close groups of domes respectively.

C. Infrared identification of domes

The next step is to determine if individual storm tops can be identified in the IR data. Since a single dome is colder than the anvil surface, we can expect a close group of domes to be colder than the anvil environment. These ideas are tested by overlaying maps of IR temperature on the visible storm

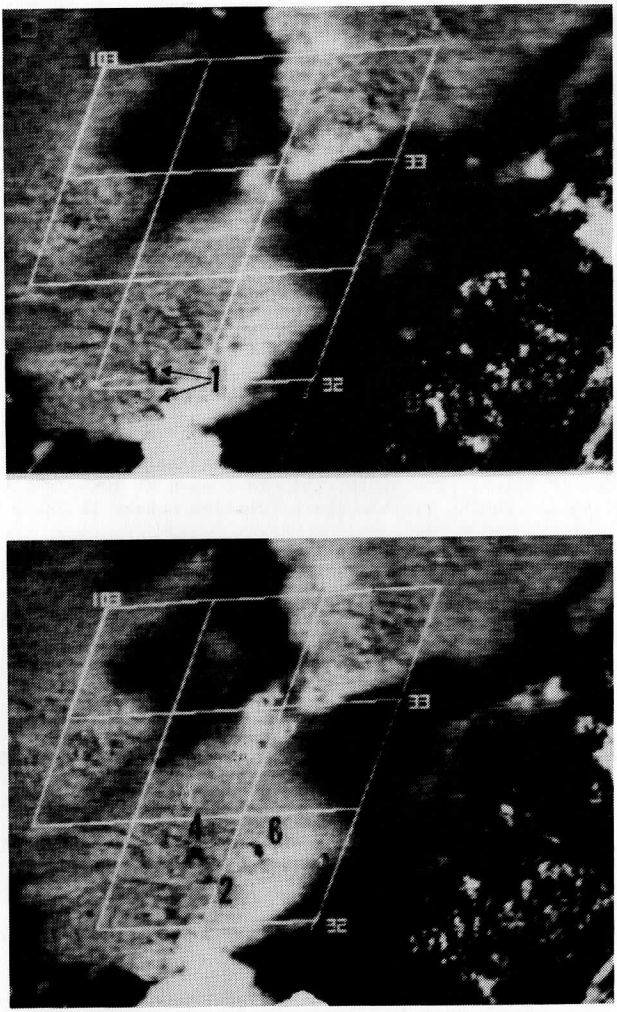

Figure III.4. 2000Z (top) & 2009Z (bottom) visible images.

Classification of Visible Domes		
Feature	Symbol	Description
Single-cell thunderstorm top	△	A single dome, identifiable by a single shadow. Shadow must be distinct, with no other shadows in its close proximity (~ 10 miles)
Multi-cell thunderstorm top	☮	Several domes, identifiable by a bumpy looking area, several shadows in a close group. Group covers an area of ~ 10 miles diameter.
Vanished top	V	Shadows that identify a single or multi cell top in one image dissappear in the next image.
Region of overshooting activity	R	An area of shadows in which individual single-cell or multi-cell tops can not be identified by their above descriptions

Table III.1. A classification of overshooting domes seen in the visible images.

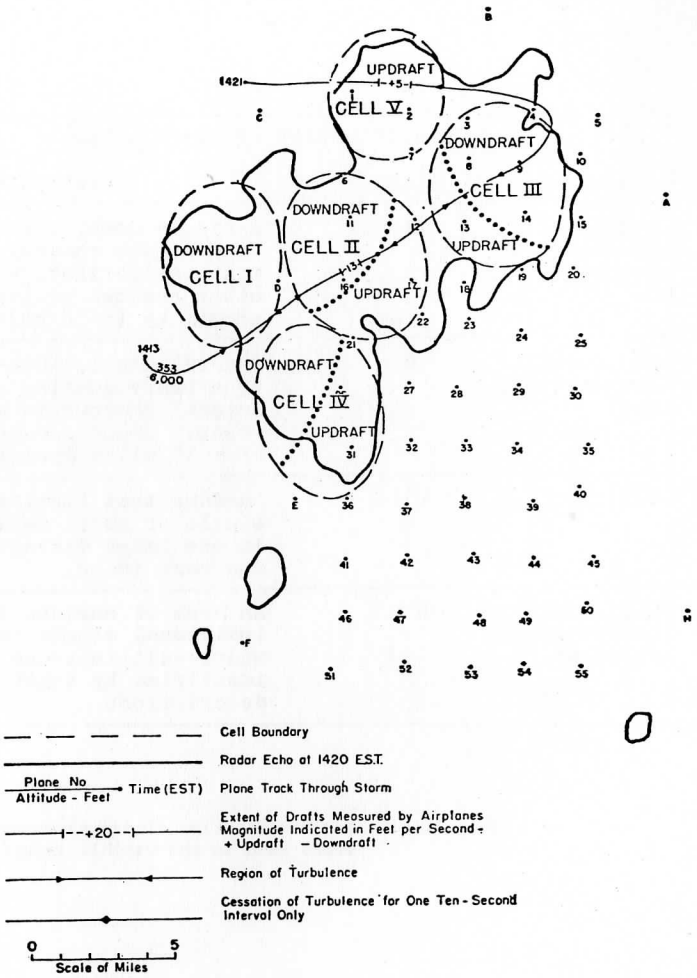

Figure III.5. Horizontal cross section of a multi-cellular thunderstorm (Byers & Braham, 1949).

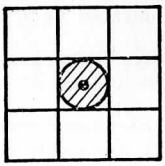

Dome A

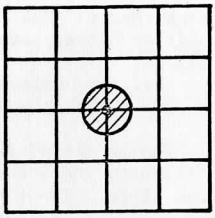

Dome B

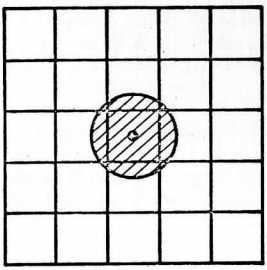

Dome C

Top view of a cylindrical dome
[area surrounding the dome is the anvil surface]

Figure III.6. Three examples of dome positions in the infrared sensing grid. Domes A & B are average-sized (6 mile diameter) while dome C is large (10 mile diameter).

track charts. The distinct cold region in the IR anvil temperatures whose position corresponds to only one SC or MC top, will be defined as a CAP.

First, consider the cap characteristics for a SC top. Important factors include the size and shape of the dome and the resolution of the IR sensor.

Fujita (1974) described domes as bubble-shaped, which is somewhere between a cylinder and a cone. He observes that turret behavior can cause changes in dome shape. The time scale of turrets (2-4 minutes) does not allow them to be monitored in rapid-scan data, so a cylindrical dome shape is assumed for this discussion.

The size of a cap depends both on dome size and its position in the grid of IR sensing boxes. One box is the true resolution of the sensor, about 6 x 6 miles over Texas. Each box is sensed twice consecutively, with the measured radiance in each sensing being assigned to a pair of pixels. Thus each box contains four pixels at possibly two different brightness values. Figure III.6 shows three domes in various grids. Dome A lies in just 1 box so it has a 4-pixel cap. Dome B has a 16-pixel cap. Finally, Dome C is larger, and has a 36-pixel cap, with a minimum temperature showing up in the center 4 pixels. The other 32 pixels are warmer than the center ones but still colder than the boxes that sense only the anvil surface. In conclusion, the cap for a SC storm may range from 4 to 36 pixels and show up to several temperature levels colder than the anvil surface.

Height variations of the dome are inferred from changing cap temperature. Assuming positive lapse rate, colder values imply dome ascent and warmer values imply descent. These dome displacements represent changes in the storm's updraft intensity.

The temperature of a cap is affected by what proportion of the IR box is sensing the dome. Therefore, it is conceivable that a cap can become colder for a dome that grows in area but not in height. However, domes observed by Fujita (1974) showed height increases coincident with diameter increases. Consequently, it will be assumed that colder cap temperatures reflect at least a height increase and possibly a simultaneous height and width increase.

Now consider a multi-cell (MC) storm top. It can be shown that a typical size (10 mile diameter) top may result in a cap size of up to 36 pixels with several temperature levels appearing. Now though, with several domes comprising the storm top, the cap temperature and its changes cannot be attributed to a particular dome. The cap temperature reflects the height of the tallest dome or domes in the storm top. A cap warming for instance implies that the highest dome or domes are now at a lower level than before. This evidence of diminished updrafts will be called a descent of the MC storm top.

For a MC storm, the temperature of a cap is affected by what proportion of the IR box is sensing the storm top. For example, a cap can become colder for a top that grows in area but not in height. Growth in area for a MC top means the addition of new domes. This can increase the proportion of an IR box that

senses dome temperature, resulting in a colder average temperature for that box. Since the addition of new domes indicates new updraft activity, this case is called an ascent of the MC storm top.

In summary, cap temperature changes for a MC storm can result from height or area changes of the top. A cap becoming warmer is called descent, it implies diminished updraft activity in the MC storm. A cap becoming colder is called ascent, it implies increased updraft activity in the storm.

D. Method example

The techniques of the last section will now be demonstrated on part of the actual data set. This example is for the area in the image sequence presented in Figure III.4.

On 5 May 1977 a dry line existed in a weak surface trough in the Texas panhandle area. A short wave at 500 mb moved rapidly across this region touching off convective activity along the dry line (see Figure III.7). Between 1900 and 2330Z there were 15 severe weather reports in an area extending from Midland, Texas to the SW corner of Oklahoma. Radar echo heights of these storms were commonly between 40,000 feet and 50,000 feet (Figure III.8).

The first step is to identify individual storm tops in the visible images. This is illustrated in Figure III.9.a using the 2015Z picture. Below the picture, the symbols mark the position of storm tops at this time. Top numbers 2 and 4 are SC at this time. Storm number 6 is MC, consisting of some shadows at 32°20'N and 101°53'W plus a dome about 7 miles to the south. Based on our earlier definition of a storm track, there are 5 such storms in this sequence. Note how a storm can undergo changes in time; storm 6 becomes MC as new domes develop on its south flank. Later these features vanish and it is again SC.

The next step is to determine if these storm tops can be seen in the IR data. This is done by comparing computer drawn maps of IR and visible brightness values, which are shown in Figures III.10.a to III.10.f (note: the 2018Z and 2024Z images had some bad scan lines which prevented the use of the plotting program). Visible brightness values range from 0 (darkest) to 256 (brightest). A program first averages the data (4 boxes to a point) and then draws the contour map of the averaged values. IR values range from 0 (+53°C) to 256 (-115°C). A contour map is also drawn of the raw IR values. The IR instrument has sensing gaps; not every digital value is attained. In this study these values are commonly seen: 204, 205, 207, 208, 210, 212, 213, 215, and 217. These correspond to specific temperature values: -63°, -64°, -66°, . . . -76°C.

On the visible maps, the brightness values of 190 or less (shaded areas) yield a pattern of dark areas similar to the shadows seen in the visible photos. By overlaying the IR maps on the visible, we can see whether a particular dark area has a cap corresponding to it.

In Figure III.11 is a graph of the history of each storm in this example.

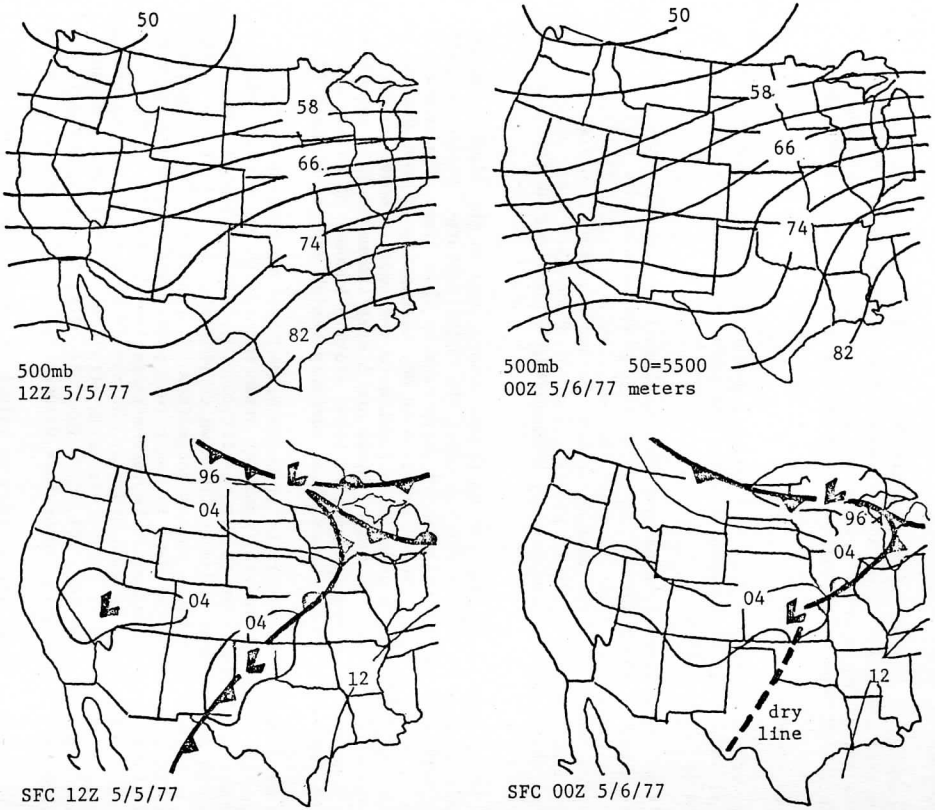

Figure III.7. Synoptic situation of 5 May 1977.

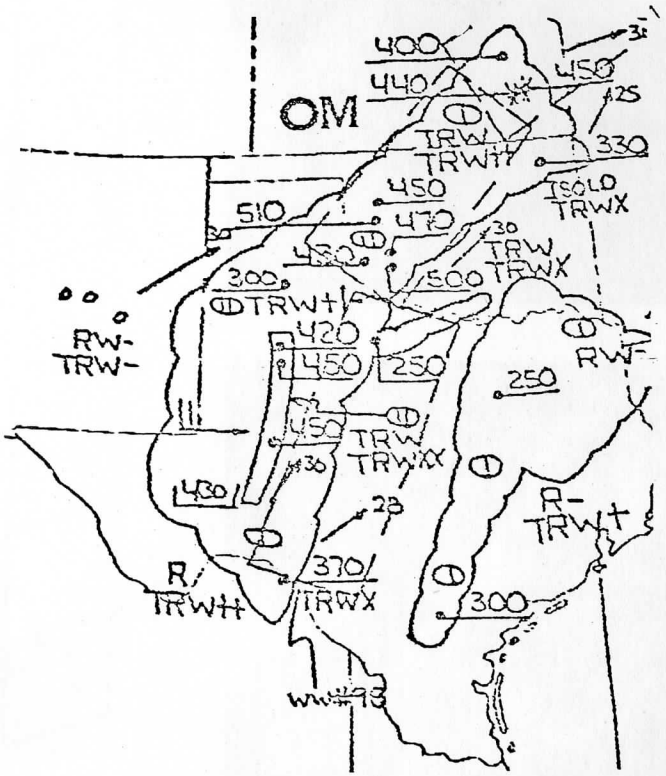

Figure III.8. National Weather Service radar summary at 2135Z on 5 May 1977.

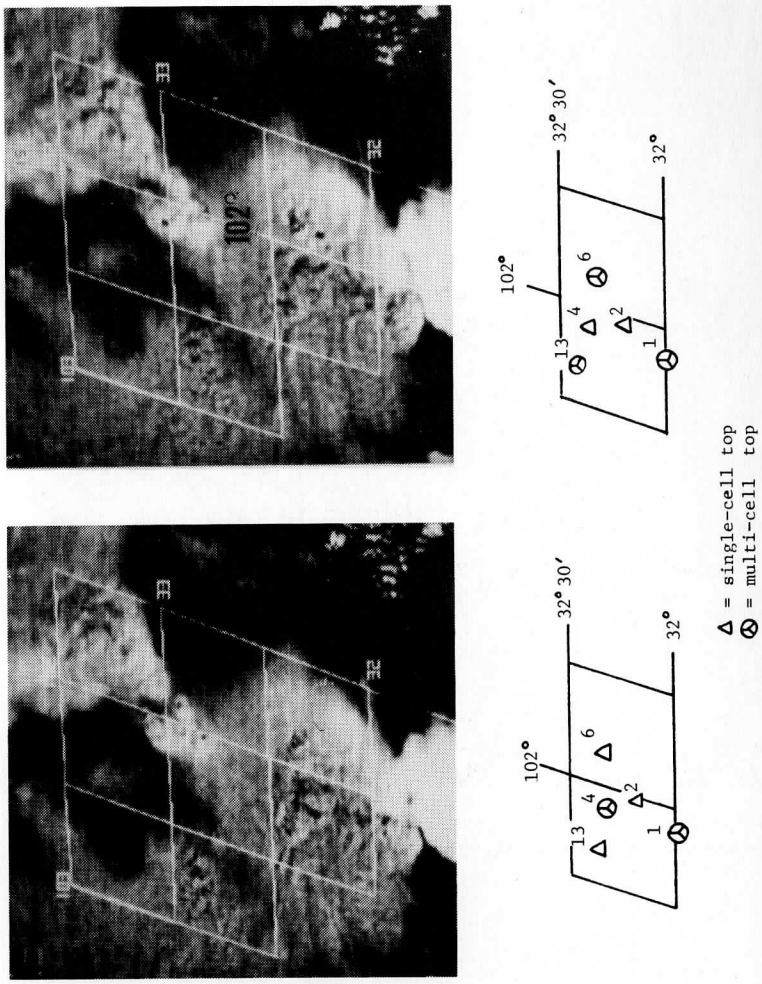

Figure III.9.a. 2012Z (bottom) and 2015Z (top) visible images and classification of overshooting features (based on Table III.1.).

Figure III.9.b. 2018Z (bottom) and 2021Z (top) visible images and classification of overshooting features (based on Table III.1.).

Figure III.9.c. 2024Z (bottom) and 2030Z (top) visible images and classification of overshooting features (based on Table III.1.).

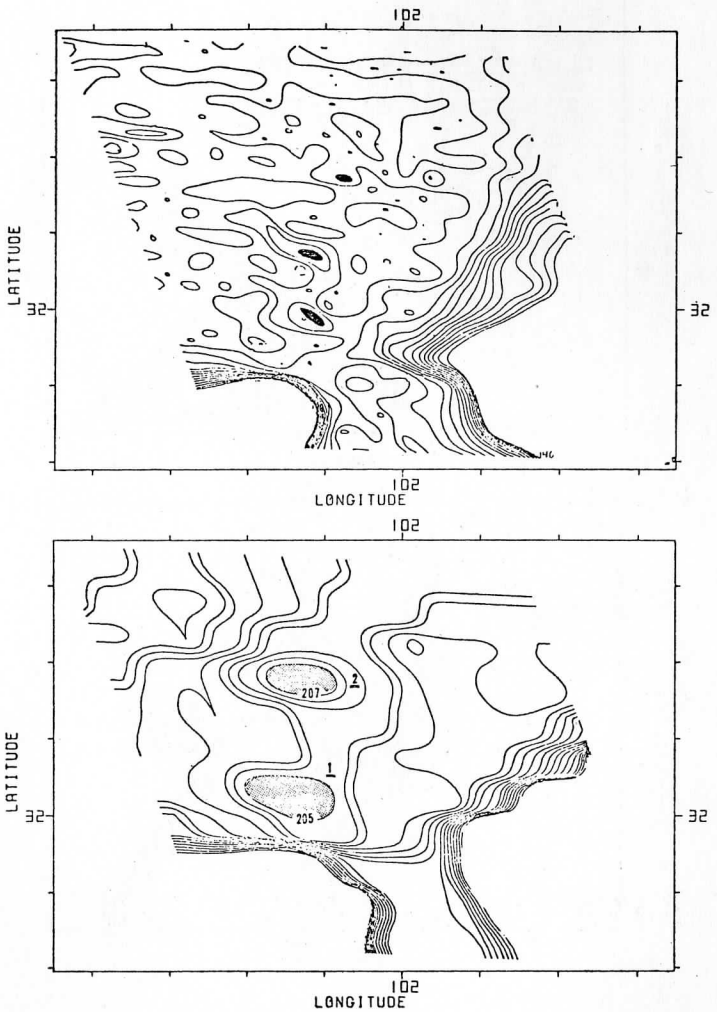

Figure III.10.a. Top: 2000Z visible brightness contours [140 (at anvil edge), 145, 150,... etc.]. Shaded regions are brightness values $\leq$ 190, within the anvil. Bottom: 2000Z IR brightness contours [190 (anvil edge), 191, 192... etc.] Shaded areas are brightness maxima in a storm cap, with storm number underlined.

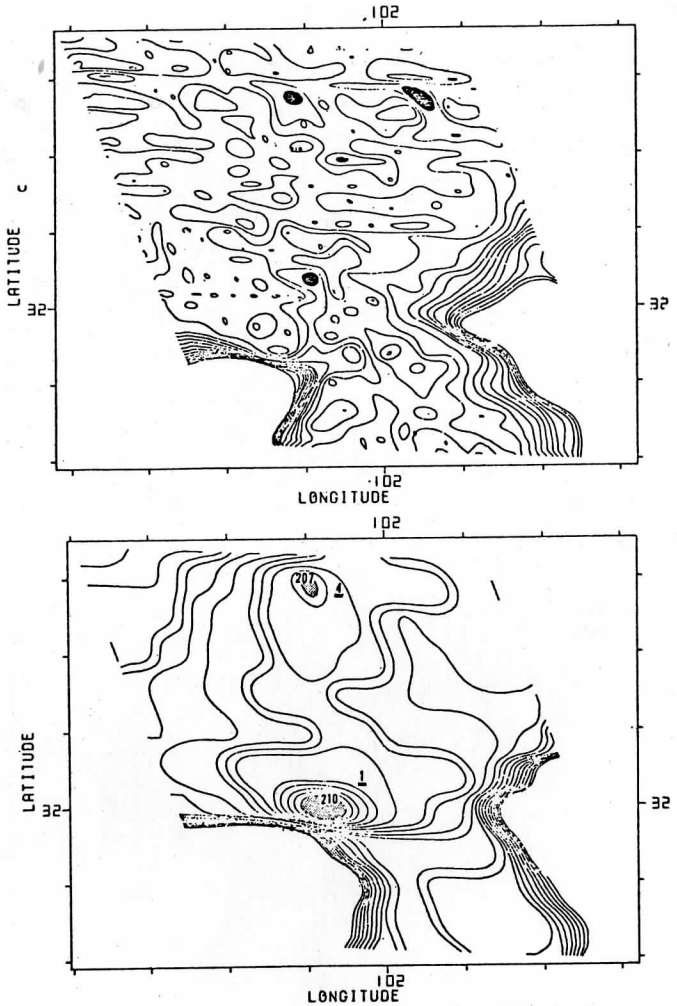

Figure III.10.b. Top: 2009Z visible brightness contours
Bottom: 2009Z IR brightness contours details, same as in Figure III.10.a.

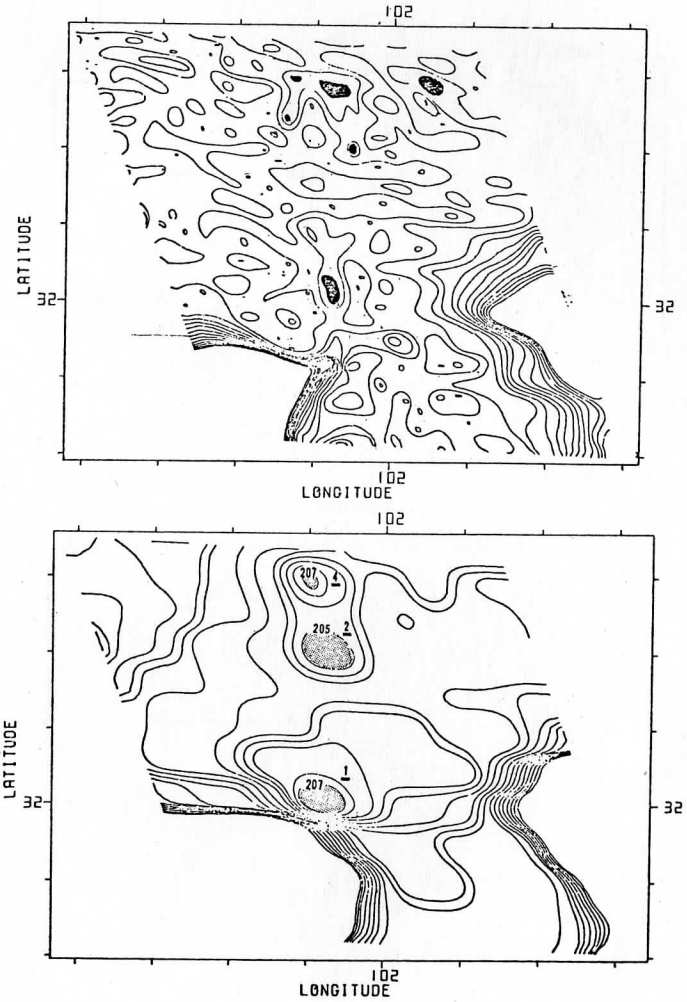

Figure III.10.c. Top: 2012Z visible brightness contours
Bottom: 2012Z IR brightness contours details, same as in Figure III.10.a.

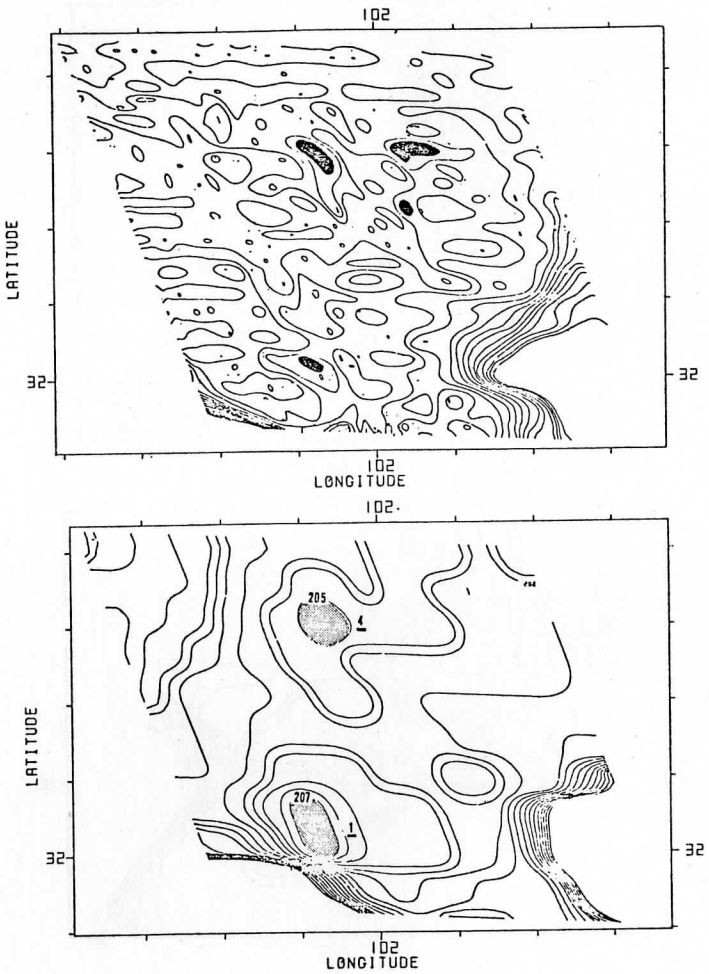

Figure III.10.d. Top: 2015Z visible brightness contours
Bottom: 2015Z IR brightness contours details, same as in Figure III.10.a.

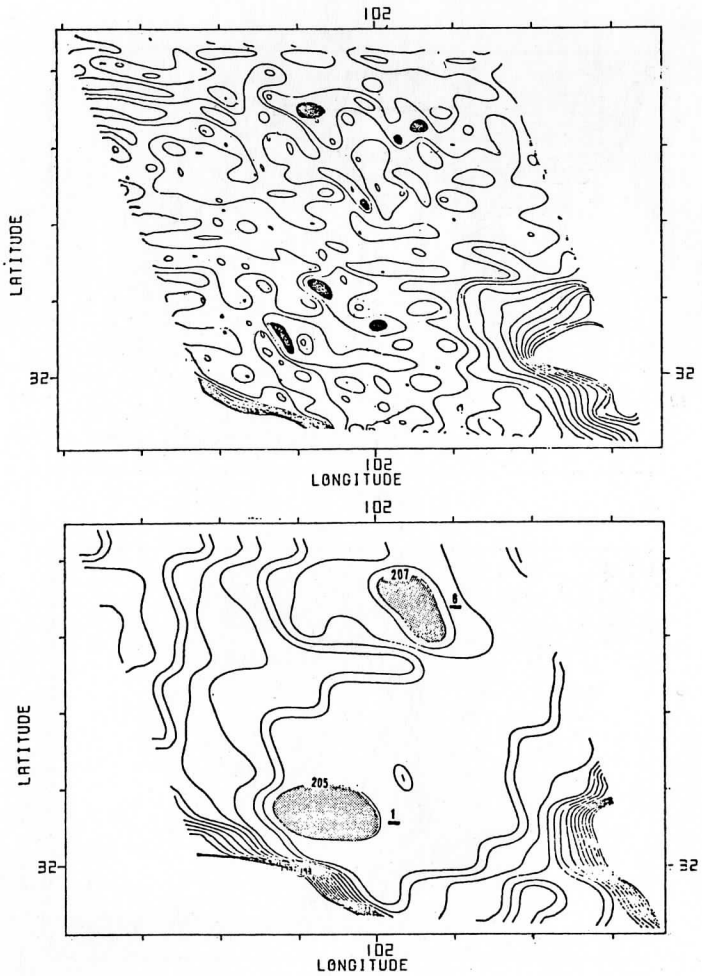

Figure III.10.e. Top: 2021Z visible brightness contours
Bottom: 2021Z IR brightness contours details, same as in Figure III.10.a.

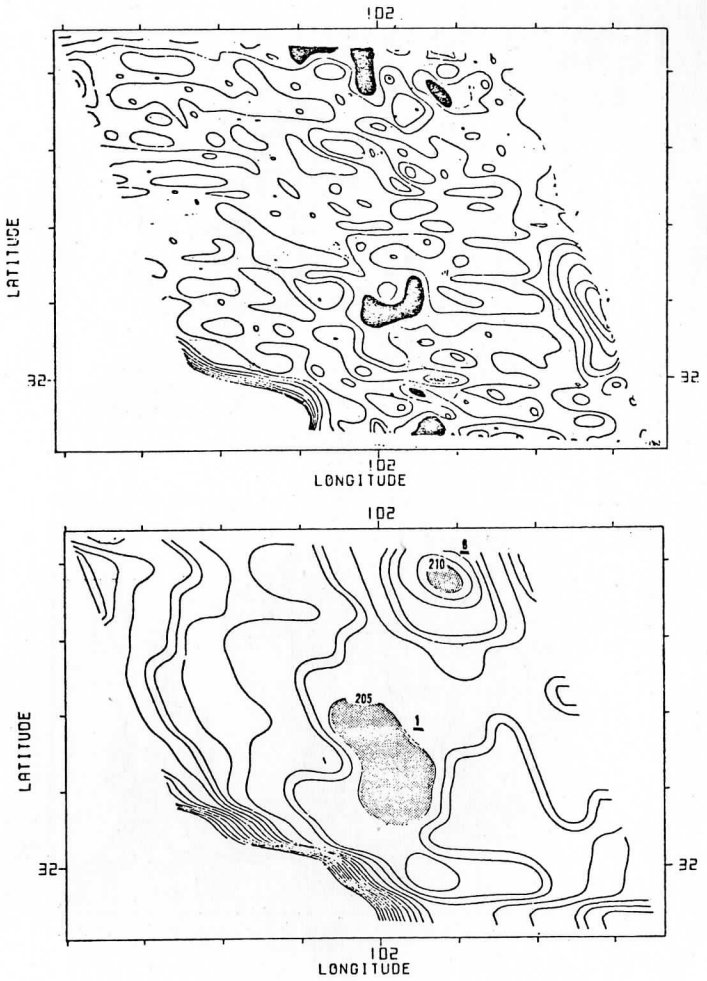

Figure III.10.f. Top: 2030Z visible brightness contours
Bottom: 2030Z IR brightness contours details, same as in Figure III.10.a.

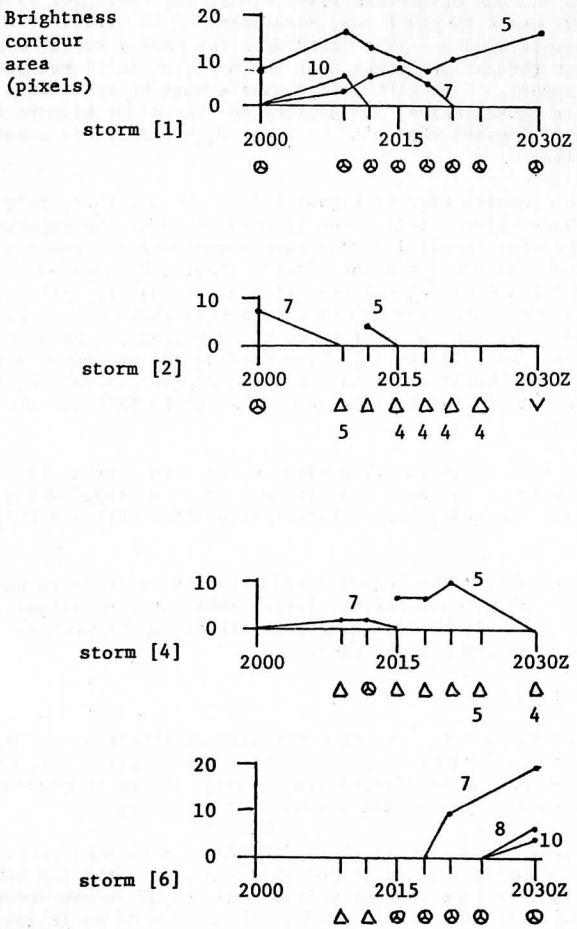

Figure III.11. Area (no. of pixels) of each brightness contour in storm cap, versus time. If a cap does not exist at a time, the brightest pixel within 6 miles of storm is listed below storm symbol. Brightness contours are: 4=204, 5=205,....etc.

For each time the visible classification of the storm is listed along with the number of pixels at each brightness level within the cap. For example, storm number 1 at 2009Z has a 24-pixel cap, consisting of 14 pixels at 205, 4 pixels at 207, and 6 pixels at 210. If a storm does not have a cap at a particular time, the coldest (brightest) pixel near its position is listed just below the classification symbol. Caps with just 2 pixels must be considered carefully. When an IR box is sensed twice, one sensing may be colder because of instrument noise. Therefore, 2-pixel caps will be plotted, but will not enter into any calculated results.

In the IR brightness maps of Figure III.10.a - III.10.f, -58°C corresponds to a 198 brightness value. This value is seen to be on the brighter (colder) edge of the brightness transition zone that represents the great temperature difference between the anvil and the ground. Thus, the anvil is very near the tropopause, and the overshooting domes are penetrating it. With cap values of 204 - 210, these domes are from 600 to 1200 meters above the tropopause, assuming moist adiabatic ascent (10°C per km at these heights). Because of the coarse resolution of the sensor in the IR, these dome height estimates may be too low, thus preventing measurement of actual height changes. Therefore, this study will look at the relative height changes evidenced by IR temperature variations of the storm tops.

Four of the five storms in this example are identifiable by a cap at sometime in this sequence. In these four storms, SC or MC tops have a cap 52% of the time, and each cap shows temperature changes that indicate height variations of the top.

Similar results, for the method applied to the entire data set, are presented in section III.A. But first, several inherent limitations in this particular data set make slight adjustments necessary in the method. These factors are discussed in the next section.

E. Data limitations

Two factors inherent in this data set have an effect on our method of determining storm top heights in the IR data. One concerns the speed of storm movement on 5 May and how it affects time changes of cap temperature. The other results from the uneven time intervals between images.

Consider first the effect of these factors on a SC storm top. The position of a dome as it moves through an IR box grid can affect the cap temperature. For instance, assume a dome remains at the same height in two consecutive images. In the first image the dome is centered in the middle of an IR box, and in the second image it has moved so that it is now centered between that IR box and an adjacent one. In the first image there is a cap of 4 pixels at a certain temperature, while the cap for the next image is 16 pixels at a warmer temperature. A warmer temperature occurs for a dome whose height is unchanged. This is a false descent.

The false descent phenomenon was studied in detail using dome movement representative of the majority of storms in the case study; the calculations are shown in the appendix. One result is that for 3-minute image intervals, false descent could occur in just one image. That is, a cap is warmer in one image than in the preceding and succeeding ones. Results also show that such a cap warming could occur over two consecutive 3-minute images. These events will be called 1-image and 2-image false descents.

The method is modified in several ways. First, real dome descents that are either 1-image or 2-image in length cannot be distinguished. Secondly, cap warmings lasting three consecutive 3-minute images or longer have a high probability of implying real descent. An event of this time length will be called a 3-image event.

As a result of this discussion, the method for determining dome height changes is modified in one important way. A given temperature in the cap must disappear for at least a 3-image interval in order to assume that a dome has descended. This brings us to the second data limitation, the fact that the image sequence is not a uniform 3-minute interval between pictures. The possibility of a 3-image descent occurring during the data gaps must be considered.

Consider the case where a cap warming appears in just two successive images, but at least one of the images is connected to a data gap (i.e., cap warming occurs in the 1921 and 1924Z images). If the 1927Z image were available, a 3-image cap warming might be observed. Such cases will be referred to as type-II descents, for they possibly indicate real dome descent. A type-I descent is an observed 3-image or longer cap warming.

This discussion has involved a SC storm top, a single dome. Analysis of the domes in a MC top is subject to the same limiting factors. Therefore, when examining these storms, the same method modification is made, type-I and type-II descents are distinguished.

III. RESULTS

In the first part of this section, storm height statistics that are obtained from the application of the method to the entire data set are examined. Next, severe weather reports are located in the images, and the features of the severe weather producing storms are described. Finally, several relationships between storm height and severe weather are determined. These relationships are compared to the results of other studies investigating such relationships with different methods.

A. Storm height statistics

Upon viewing and classifying domes in the entire visible sequence, 37 storm tracks are defined. These storms are separated into four groups, based upon locale and time of occurrence. Each group seems to represent a preferred

region of convection along the dry line, but the distance between weather stations in this area is greater than the size of each storm group. This prevents any attempt to analyze the dynamical cause of these four regions. Storm height statistics for each group and for all storms combined are presented in Table III.2.

An important goal of this study is to determine if individual thunderstorm tops can be identified in the IR data. On this day, 272 single-cell tops are seen in the visible pictures, and 128 (47%) have an IR cap. Two factors appear responsible for this result. First, small domes can escape detection in the IR sensing box. Second, two domes 10 miles apart (as required in the visible classification technique) can lie in adjacent IR boxes. This results in one cold region associated with the two domes rather than separate caps.

Multi-cell (MC) tops are as frequent as SC tops on this day; 290 are identified, with 142 (49%) having caps. Caps for MC tops average a little larger than SC caps as expected, since they consist of several domes.

Of the 37 storms, 30 (81%) have a cap associated with them sometime during their life. In these storms, the IR temperature changes indicate height variations of the storm top. There are 74 observed periods of ascent or descent in these 30 storms. For example, storm 1 in Figure III.12 has a descent (type-I) at 1948Z as the 207 value disappears and a type-II descent at 1951Z as the 205 value vanishes. Together these represent one descent period, an uninterrupted (no ascents) sequence of type-I or type-II descents. Similarly, an ascent period exists from 2000Z to 2009Z, consisting of the appearance of the 205, 207, and the 210 brightness values.

At this point it has been shown that the existence of caps on this day provides a convection intensity parameter for individual thunderstorms. Changes in the cap temperature reflect height variations of the overshooting top which depend on the strength of the storm's updrafts. The next step is to determine whether this parameter can be related to severe weather-producing storms on this day.

B. Severe storm statistics

Severe weather reports on this day include tornadoes, funnel clouds, and large hail. Report sources are MONTHLY STORM DATA and the National Severe Storms Forecast Center's report log on 5 May 1977.

In order to accurately place the location of these events in the visible sequence, the navigation of satellite images must be carefully considered. The positions of clouds are determined by their location with respect to known landmarks such as lakes and rivers that appear in the image. When viewing overshooting tops, as in Figure III.13, the navigated position of the top at point B is in error, due to a parallax effect. The storm top is actually located above point A.

For a 45,000 foot top, an average radar echo height on this day, point B

Area	A	B	C	D	All areas
# of storms in area	13	5	9	10	37
% of IR caps for:					
Single-cell tops	56/119 .47	22/44 .50	24/59 .41	26/50 .52	128/272 .47
Multi-cell tops	58/130 .45	3/7 .43	52/98 .53	29/55 .53	142/290 .49
All tops	114/249 .46	25/51 .49	76/157 .48	55/105 .52	270/562 .48
Average cap size (pixels)					
Single-cell tops	8.6	9.4	9.4	7.8	8.7
Multi-cell tops	11.9	11.3	11.5	9.3	11.2
All tops	10.2	9.6	10.8	8.6	10.0
% of storms with cap	11/13 .85	3/5 .60	8/9 .89	8/10 .80	30/37 .81
# of height changes					
Ascent periods	15	5	10	11	41
Descent periods	12	5	9	7	33

Table III.2. Storm height statistics, by area, and for all storms monitored in the data set.

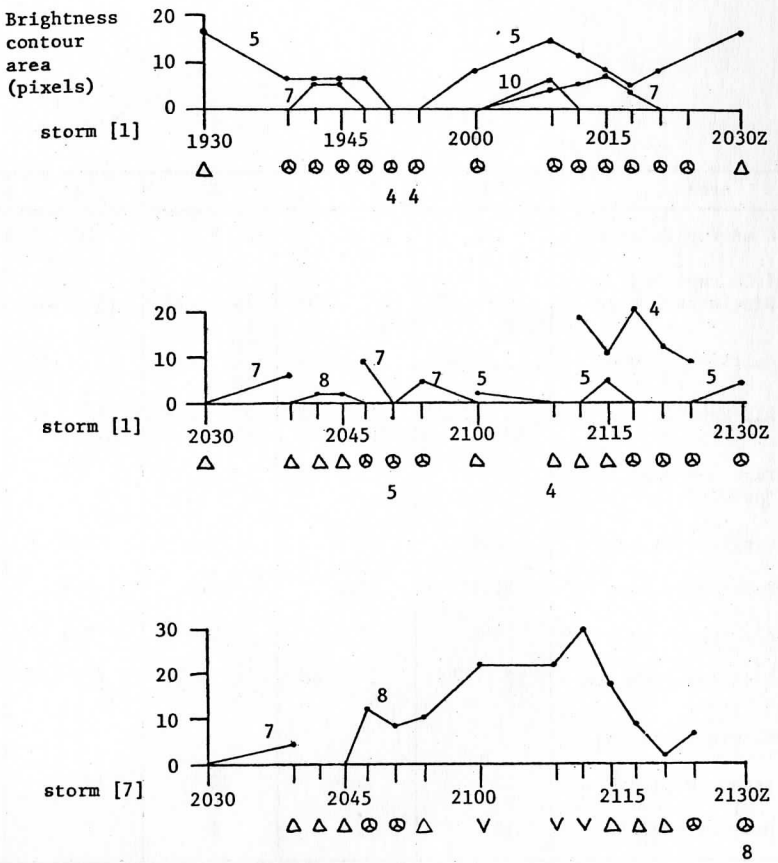

Figure III.12. Area (no. of pixels) of each brightness contour in storm cap, versus time. If a cap does not exist at a time, the brightest pixel within 6 miles of storm is listed below storm symbol. Brightness contours are: 4=204, 5=205,....etc.

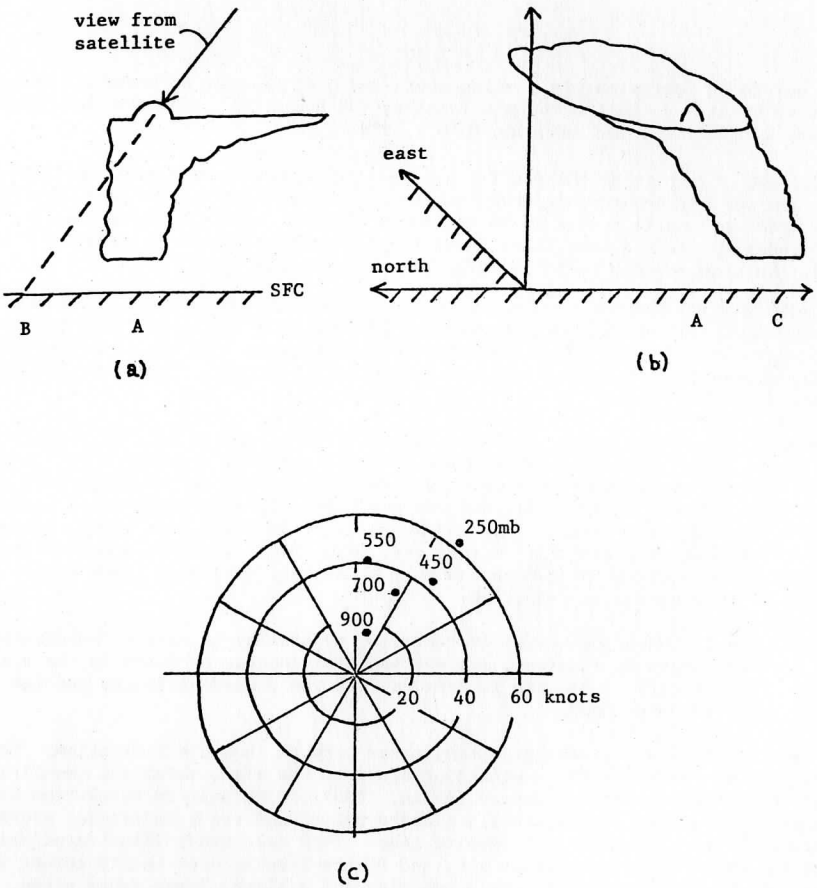

Figure III.13. a) Parallax error in viewing overshooting tops
b) Possible storm tilt on 5 May 1977
c) 1800Z hodograph at Midland, Texas.

turns out to be approximately 6 miles north and 5 miles west of point A. This can be calculated using the storm's locality (35°N & 100°W), and the satellite's altitude (36,000+ km) and subpoint (0°N & 75°W).

Instead of adjusting the positions of all monitored storms, the positions of severe weather reports are moved to the northwest. Additionally, a certain small error may still remain if the storm is sheared (see Figure III.13). An 1800Z hodograph at Midland, Texas shows that storm tilt may be towards the north. No precise adjustment is made for this possible error.

Important statistics concerning visible and IR characteristics of severe weather-producing storms are presented in Tables III.3 - III.6. These tables will be referred to throughout the rest of this section. Of the 15 severe events in the area of interest, 14 occur near a visible storm top. These are listed in Tables III.3 and III.5.

With the parallax error corrected, 10 of these 14 storms had the visible top less than 7 miles from the severe event's location at its reported time. Three of the other four cases had a storm top 10-15 miles northeast of the report at report time (storms no.9,30,&32) and one storm (no.15) was twelve miles northwest of its associated event. The northward error in these four cases could be partly explained by storm tilt on this day. Thus, with parallax error corrected, the position of overshooting tops can very accurately determine where severe weather at the surface is occurring.

This result should be useful in real-time monitoring of severe thunderstorms. Once a severe storm is reported, its overshooting top can be found in the visible image. The velocity of the top is derived from the preceding images and its future track is determined.

The current storm tracking system, radar network, has one limitation. The resolution of radar decreases with distance from the site, which can result in individual echoes appearing merged (Atlas, 1963). With uniform resolution over a large area, geostationary satellite could detect and track individual storms in areas where radar could not resolve them. This case study illustrated this situation well. Storms in areas B,C, and D were located near the SW corner of Oklahoma, directly between the Oklahoma City and Midland, Texas radar sites. Comparison of radar and satellite storm tracks is not possible, due to the infrequent radar pictures on this day.

Tables III.3 and III.5 describe the visible characteristics of the severe storm near report time. For example, storm 15 is single-cell at 2239Z, this image being considered "during" the event. In the preceding 3 images the storm is multi-celled, and in the succeeding 3 images the top is gone. Based on these subjective classifications the change from MC 2230Z to SC at 2239Z represents descent one minute before the event. That is, in going from MC to SC some domes must have disappeared. The complete disappearance of the top at 2242Z implies descent two minutes after the event. Analogously, a change from SC to MC, or the initial appearance of a top, is a sign of ascent. It is important to remember that this visible evidence is subjectively determined, and thus is supplementary to the quantitative IR evidence of height variations.

In Tables III.4 and III.6 information derived from the IR data is presented for the storms. Of the 14 storms, 11 have caps at the event time. The temperature of the cap at event time is compared to the minimum temperature observed in that storm's lifetime. This indicates whether the storm is at its maximum height when it produces the severe weather. Also, the temperature of other storm caps in the same convection group (A,B,C, or D) are listed. This determines if the severe weather is associated with the highest storm top in that area. For example, storm 1 (Table III.4) produces a tornado at 2100Z when it is well below its maximum height, indicating that the updraft is not at its maximum intensity. Also, there are two other storms in area A that are higher than storm 1 at this time.

Finally, the existence of a cap enables the determination of height changes of a severe storm's top. Ascent and descent periods are the same as previously defined for Table III.2, with descent periods including type-I or type-II descents. The timing of height changes is best illustrated by an example. Considering storm 1 and its 2100Z tornado, ascent occurs at 2039Z (21 minutes before the event) as the 207 value appears (Figure III.12). The following cap of two pixels at the 208 value is considered noise. Type-II descent occurs at 2100Z as the 207 value disappears. The graphs in Figures III.14 and III.15 enable this information to be determined for the other severe storms.

Conclusions based on the information in Tables 3-6 will be discussed in the next section. They will be compared with results of other studies relating storm height and updraft intensity to severe weather.

C. The relationship between storm height variation and severe weather

Based on Tables III.3 - III.6, visible and IR evidence relating height changes of the storm top to the timing of severe weather is presented in contingency table form in Table III.7. The number of observed ascent or descent periods in each time category is listed, along with their averaged time relative to the event. Results are presented separately for the hail event and for the tornado/funnel reports combined. Storm 1 at 2000Z has a tornado and hail reported at nearly the same time, therefore its height changes are entered in each of the two categories. A particular event may have more than one height change associated with it. In the IR evidence for example, storm 48 (Table III.6) has an ascent period and a descent period prior to its funnel at 2000Z. Similarly, multiple entries occur concerning the visible evidence.

Multiple entries are not allowed in true contingency tables, thus exact statistics can't be derived in this case, but certain relationships are suggested in our results.

For the hail reports, the largest table entry in the IR evidence is the four ascents before the event, averaging 14 minutes in advance. The visible evidence supports this finding, showing four instances of ascent, 13 minutes before the event. For the tornado/funnel category, IR again shows ascent prior to the event, five cases averaging 16 minutes in advance. But now there are five cases

Severe Weather Report	Time (GMT)	Location	Storm & Area	Storm classification relative to event			Visible evidence of storm height change (A=ascent, D=descent)		
				Before	During	After	Before	During	After
Hail & Tornado	2000 2005	near Midland, Texas	1-A	✇	✇	✇	--	--	--
Tornado	2100	32 miles ENE of Midland	1-A	✇	△	△	--	D :00	--
Tornado	2055	5 mi. S of Ackerley, Tx.	7-A	△ ↓ ✇	△	△ ↑ V	A :16 A :07 D :01	--	D :05 A :17
Hail	2057	Grassland Tx.	13-A	△	△	△	A :06	--	--
Tornado	2240	4 mi. W of Roby, Tx.	15-A	✇	△	V	D :01	--	D :02
Tornado	2300	Aspermont Tx.	9-A	✇ ↓ △	△	△	D :06	--	--
Tornado	2230	Tipton, Oklahoma	75-D	△ ↓ ✇	✇	✇	A :12	--	--

Table III.3. Severe weather events and parent storms. Visible height changes (A=ascent, D=descent) are in minutes relative to the event's time.

Severe weather Report	Time (GMT)	Storm & Area	IR cap temperature (°C) during report	IR cap temperature (°C) lifetime minimum	Other cap temp. in area--- during report	IR evidence of storm height change (A=ascent, D=descent) Before	During	After
Hail & Tornado	2000 2005	1-A	-66	-69	-66	D :12	A :00	--
Tornado	2100	1-A	-64	-69	-67 -72	A :21	D :00	--
Tornado	2055	1-A	-67	-67	-64 -72	A :07	--	--
Hail	2057	13-A	-72	-72	-64 -67	A :06	--	D :12
Tornado	2240	15-A	--	--	--	--	--	--
Tornado	2300	9-A	-71	-71	--	--	--	--
Tornado	2230	-D	--	--	--	--	--	--

Table III.4. IR cap characteristics for severe storms of Table 3. Height changes (A=ascent, D=descent) are in minutes relative to the event's time.

Severe Weather Report	Time (GMT)	Location	Storm & Area	Storm classification relative to event			Visible evidence of storm height change (A=ascent, D=descent)		
				Before	During	After	Before	During	After
Hail	1930	Crosbyton, Texas	30-B	✇	△	△	A :12	D :00	--
Hail	2010	10 mi. E of Crosbyton, Tx.	32-B	△	△	△	A :31	--	--
Tornado	1930	8 mi. W of Crowell, Tx.	49-C	✇	✇	✇	A :18	--	--
Tornado	1951	Quanah, Tx.	49-C	✇ ↓ △	△	△	D :03	--	--
Funnel	2000	El Dorado Oklahoma	49-C	✇	✇	V	--	--	D :12
Funnel	2000	Hollis, Okla.	48-C	✇	✇	✇ ↑ △	--	--	D :09 A :12
Funnel & Hail	2035 2038	near Willow, Okla.	48-C	△ ↓ ✇	✇	✇	A ;05	--	--

Table III.5. Severe weather events and parent storms. Visible height changes (A=ascent, D=descent) are in minutes relative to the event's time.

Severe Weather Report	Time (GMT)	Storm & Area	IR cap temperature (°C) during report	IR cap temperature (°C) lifetime minimum	Other cap temp. in area--- during report	IR evidence of storm height change (A=ascent, D=descent) Before	During	After
Hail	1930	30-B	-71	-71	-69	A :12	--	--
Hail	2010	32-B	-67	-69	-71	A :22 D :01	--	A :05 D :11
Tornado	1930	49-C	--	--	--	--	--	--
Tornado	1951	49-C	-71	-72	-72	A :09	D :00	--
Funnel	2000	49-C	-69	-72	-71	D :09	--	--
Funnel	2000	48-C	-71	-74	-69	A :21 D :09	--	--
Funnel & Hail	2035 2038	48-C	-72	-72	-72	A :17	--	--

Table III.6. IR cap characteristics for severe storms of Table 5. Height changes (A=ascent, D=descent) are in minutes relative to the event's time.

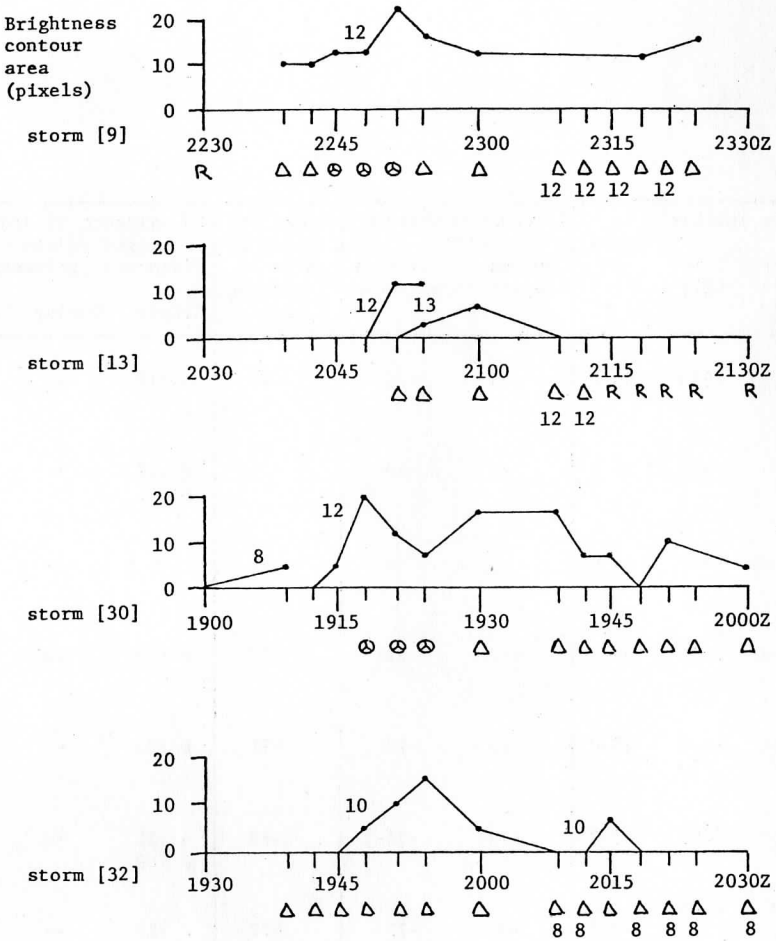

Figure III.14. Area (no. of pixels) of each brightness contour in storm cap, versus time. If a cap does not exist at a time, the brightest pixel within 6 miles of storm is listed below storm symbol. Brightness contours are: 8 = 208, 10 = 210, ... etc.

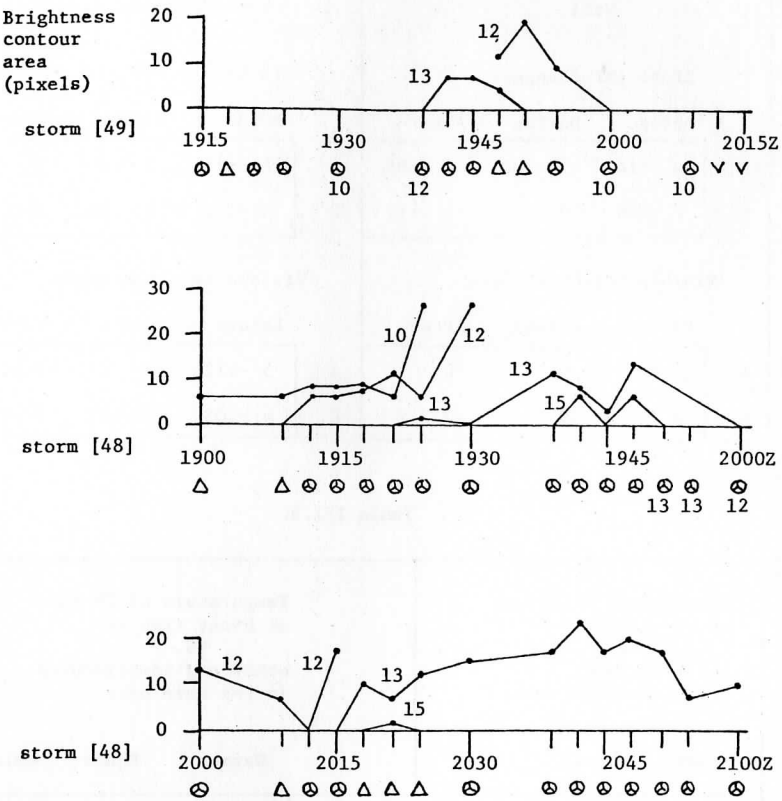

Figure III.15. Area (no. of pixels) of each brightness contour in storm cap, versus time. If a cap does not exist at a time, the brightest pixel within 6 miles of storm is listed below storm symbol. Brightness contours are: 8 = 208, 10 = 210, ... etc.

Table III.7.

	Hail				Tornado/Funnel			
	IR height changes				IR height changes			
	Before	During	After		Before	During	After	
A	4 -:14	1 -:00	1 -:05	A	5 -:16	1 -:00	0	
D	2 -:06	0	2 -:11	D	3 -:10	2 -:00	0	
	Visible height changes				Visible height changes			
	Before	During	After		Before	During	After	
A	4 -:13	0	0	A	5 -:12	0	2 -:12	
D	0	0	0	D	4 -:03	1 -:00	4 -:06	

Table III.8.

Temperature of IR cap at event time --- VS. cap's minimum lifetime temperature			Temperature of IR cap at event time --- VS. other cap temperatures in the same area		
Warmer	Equal		Warmer	Equal	Colder
2	3	Hail	1	2	3
5	3	Tornado/funnel	5	2	2

Tables III.7 and III.8. Height statistics for all severe storms. (A=ascent, D=descent; in minutes relative to the severe weather event).

of descent, 10 minutes or less in advance. Visible evidence supports this with three ascents 12 minutes in advance, and 9 descents within 6 minutes of the event. A difference between the hail and tornado/funnel storms is proposed by these results. Both types have an ascending storm top prior to the event, but only tornado/funnel reports have subsequent descent of the storm top very near the event's time.

Similar results have been found by other investigators studying severe weather. Adler & Fenn (1977) found 7 of 8 severe events occurring during or just after a rapid expansion of cold isotherms in satellite IR maps of anvil environment. These isotherms enclosed areas of up to 250 pixels, representing large regions of overshooting activity. The isotherm expansion indicates the ascent of new overshooting tops.

Fujita (1972) found decreased dome height in visible satellite images at the time of tornado production. Lear jet observations also capture this collapsing dome phenomenon, documented by Fujita (1973), Umenhofer (1975), and Fujita (1977).

Using Doppler radar techniques, Lemon et al. (1977) studied a storm which showed echo top and bounded weak-echo region descending during tornado production, thus supporting Fujita's observations.

Several hypotheses attempt to explain this unique feature of tornadic storms, the weakened updrafts implied by cloud-top or echo-top collapse. Fujita (1973) proposed the formation of a twisting downdraft by excessive water loading in the upper levels falling out of the storm. Burgess & Lemon (1976) suspect that the updraft is cut off when the storm's gust front occludes, assuming a mesocyclonic structure of the thunderstorm. These and other theories require further testing through detailed observational studies.

A result apparent in Table III.8 is that the temperature of a cap at the time of hail is equal to the minimum temperature reached during the storm's lifetime. For the two cases where this is not true, the cap's minimum temperature occurs less than 10 minutes from the event time. Pearl et al. (1975) observed domes reaching their maximum height at the time hail was reported beneath them. Also, tornado/funnel occurrences (Table III.8) are at a time when the cap temperature is warmer than the minimum, a sign of descent of the storm top.

Finally, when comparing cap temperatures at event time with other caps in the same area (Table III.8), hail reports come from the highest tops, while tornado/funnel events did not show this characteristic. This agrees with Bonner & Kempler (1971), using radar echo heights they found that tornado probability depends less on the extent of tropopause penetration than hail probability does. Another study of radar echo heights (Darrah, 1977) revealed that hailstorms had a higher penetration above the tropopause than tornadic storms. The mean penetration for 224 hailstorms was 1140 meters while the 126 tornado storms averaged just 350 meters above the tropopause.

IV. CONCLUSION

With the spatial resolution of SMS-1 rapid-scan images, overshooting thunderstorm tops are identifiable in infrared (IR) maps of anvil surface temperature. They appear as isolated cold regions, caps, which are colder than the surrounding anvil. Of the 562 storm tops seen in the 60 visible images, 48% had an IR cap. The IR resolution is the main factor that prevents the detection of more storm caps.

By observing changes in cap temperature, height variations of the storm tops can be detected. In the 30 storm tracks that had IR caps, 74 ascent or descent periods are observed. The IR resolution and the storm velocity combine to limit the time scale of height changes that can be detected. A top that shows descent (cap appears warmer) in just one image, or even two consecutive images, cannot be assumed to represent a true height change. We are limited to assuming that cap warmings lasting three consecutive images, or longer, are realistic descent.

These findings show that height variations of overshooting thunderstorms can be studied from geostationary satellite. They stress that increased IR sensor resolution would improve future use. Continuous three-minute images would also be beneficial, eliminating the uncertainties that arise during the data gaps. Increased time resolution may not be important, however, since it could be decreased by the same factors that limited the de facto time resolution in this study.

The placement of severe weather reports in the satellite images reveals two important facts. First, 14 of 15 events occur beneath an overshooting top. This suggests that geostationary satellite can be used to track severe storms. Secondly, several relationships between storm height change and severe weather substantiate the findings of other investigators. Hail events and tornado/funnel reports both have storm tops that ascend about 15 minutes before the event. But only tornado/funnel storms show a subsequent descent of the storm top near event time.

The observation of overshooting activity for a single- or a multi-cell storm is not a unique signature of a severe storm, as only 10 of 37 storms in this study produced severe weather. However, this parameter could serve as an imminent severe weather signal. In this case study, a false alarm rate (FAR) of 73% results from 27 of the storms not producing severe events. But 14 of 15 events would have been correctly predicted if an imminent severe weather warning had been issued for each of the 37 storms, a probability of detection (POD) of 93%. In contrast, Foster (1976) found that the current NWS severe thunderstorm radar warning criteria have a FAR of 85% and a POD of 47%. Further investigations of the use of the overshooting parameter as a warning signal are necessary to determine if it can be applied in real-time situations.

Perhaps it is not just the appearance of an overshooting top, but rather a characteristic of the top that could serve as an imminent severe weather signal. The height variations of the top may be this characteristic, as this study has shown relationships between height change of the top and severe weather. But

these relationships must be better defined to show statistical significance. This requires a larger data base for more case studies like this one. The development of an IR sensor with better resolution is the next step in attempting to improve the results of such studies.

APPENDIX

This appendix discusses the false descent phenomenon that was defined in Section II.C. By using variables determined from the data set, the unique characteristics of false descents in this case study will be derived. False descents depend upon dome characteristics and the time interval between images. The time interval between images is three minutes, and the dome characteristics are unchanging in time.

Based on Fujita's (1974) findings, a typical dome is six miles in diameter and one km above the anvil. Thus, assume a cylindrical dome, as discussed in Section II.C. A one km dome would be 10°C colder than its anvil for moist adiabatic ascent, but mixing with the nearly isothermal tropopause environment could decrease this figure. Therefore, consider a dome that is 5°C colder than the anvil. Cap brightness values ranged from 204 to 217 on 5 May, so put the dome at 210 (-69°C), and the anvil 5°C warmer at 205 (-64°C).

The dome just described is used in two examples, each having a different dome velocity. From visible storm tracks on 5 May, the majority had a speed near 30 miles per hour. Direction of movement was between north and east.

The first example is for a dome moving east (Figure III.1). At each time, the average brightness value of the two IR boxes is calculated. This is done by multiplying the percentage of the box sensing the dome by 210, and multiplying the remainder of the box by 205. The dome percentage is estimated by breaking the IR box up into 36 one mile square pieces, and estimating how many are covered by the dome. If the resulting box brightness is 207 or greater, a cap is defined. Recall that the values 206 and 209 are not measured by the sensor. The plot of cap brightness and area versus time reveals a one-image cap warming at t6. This is a false descent since the dome's height is unchanged. This result would be unchanged if the dome's movement was due northward.

In the second example (Figure III.A.2) the dome moves northeastward at 30 mph through a grid of four boxes. Cap brightness and size is calculated in the same manner. The resulting graph shows an apparent cap warming over two consecutive images. This is a two-image false descent.

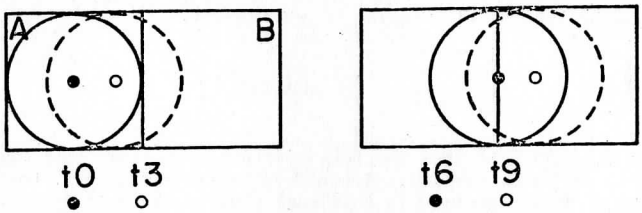

Time \ Box	A		B	
	Dome %	Bright. value	Dome %	Bright. value
t0	.78	208.9	.00	205.0
t3	.67	208.3	.11	205.6
t6	.39	206.9	.39	206.9
t9	.11	205.6	.67	208.3

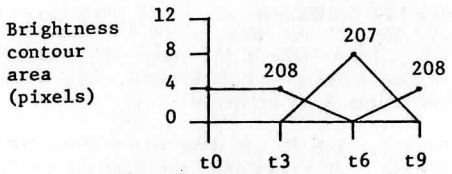

Figure III.A.1. Dome positions every three minutes and resulting IR box brightness values. Area (pixels) of each IR brightness contour in storm cap plotted against time.

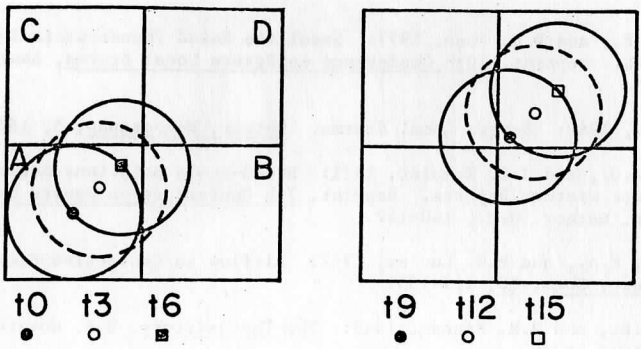

Box / Time	A		B		C		D	
	Dome %	Bright. value	Dome %	Bright. value	Dome %	Bright. value	Dome %	Bright. value
t0	.78	208.9	.00	205.0	.00	205.0	.00	205.0
t3	.61	208.0	.08	205.4	.08	205.4	.00	205.0
t6	.33	206.7	.17	205.8	.08	205.4	.11	205.6
t9	.14	205.7	.19	206.0	.19	206.0	.25	206.2
t12	.00	205.0	.14	205.7	.14	205.7	.50	207.5
t15	.00	205.0	.00	205.0	.00	205.0	.69	208.5

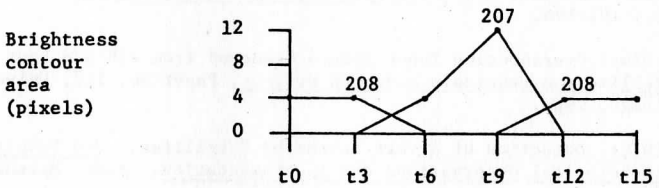

Figure III.A.2. Dome positions every three minutes and resulting IR box brightness values area (pixels) of each IR brightness contour in storm cap plotted against time.

REFERENCES

Adler, R.F., and D.D. Fenn, 1977: Satellite Based Thunderstorm Intensity Parameters. Reprint, 10th Conference on Severe Local Storms, Amer. Meteor. Soc., 8-15.

Atlas, D., 1963: Severe Local Storms. Meteor. Monographs, 5, 183pp.

Bonner, W.D., and J.E. Kempler, 1971: Broad-scale Relations between Radar and Severe Weather Reports. Reprint, 7th Conference on Severe Local Storms, Amer. Meteor. Soc., 140-147.

Browning, K.A., and E.H. Ludlam, 1962: Airflow in Convective Storms. Q. J. Royal Meteor. Soc., 88, 117-135.

Byers, H.R., and R.R. Braham, 1949: The Thunderstorm, U.S. Government Printing Office, 287pp.

Darrah, R., 1977: The Interaction of Severe Thunderstorms with the Lower Stratosphere, M.S. Thesis, University of Wisconsin-Madison, 69pp.

Donaldson, R.J., 1960: Radar Methods for Identification of Severe Thunderstorms. Reprint, Conference on Severe Local Storms, Amer. Meteor. Soc., 28pp.

Foster, D.S., 1976: Verification of Severe Local Storm Warnings Based on Radar Echo Characteristics, NOAA Tech. Memo., NWS TDL-60, 10pp.

Fankhauser, H.R., 1971: Thunderstorm-environment Interactions Determined from Aircraft and Radar Observations. Mon. Wea. Rev., 99, 171-192.

Fujita, T.T., 1972: Tornado Occurrences Related to Overshooting Cloud-top Heights as Determined from ATS Pictures. Satellite and Mesoscale Research Project, Paper No. 97, University of Chicago, 32pp.

_____, 1973: Proposed Mechanism of Tornado Formation from a Rotating Thunderstorm. Reprint, 8th Conference on Severe Local Storms, Amer. Meteor. Soc., 191-196.

_____, 1974: Overshooting Thunderheads Observed from ATS and Lear Jet. Satellite and Mesoscale Research Project, Paper No. 117, University of Chicago, 29pp.

_____, 1976: Detection of Severe Storms by Satellites. 3rd Symposium on Meteorological Observations and Instrumentation. Amer. Meteor. Soc., 5-9.

_____, 1977: Flight over a Tornado-bearing Thunderstorm. Bulletin of the Amer. Meteor. Soc., 608-609.

Kreitzberg, C.W., 1978: SESAME '77 Experiments and Data Availability. Bulletin of the Amer. Meteor. Soc., 1299-1301.

Lemon, L.R., D.W. Burgess, and R.A. Brown, 1978: Tornadic Storm Airflow and Morphology Derived from Single-Doppler Radar Measurements. Mon. Wea. Rev., 106, 48-61.

Newton, C.W., 1963: Dynamics of Severe Convection Storms. Meteor. Monographs, 5, 33-58.

_____, 1966: Circulation in Large Sheared Cumulonimbus. Tellus XVIII, 4, 699-712.

Pearl, E.W., W.E. Shenk, and W. Skillman, 1975: Cloud-top Parameters--a Hail Indicator. Reprint, 9th Conference on Severe Local Storms, Amer. Meteor. Soc., 464-467.

Remick, J.H., 1971: Radar Reflectivity Profile of Individual Cells in a Persistent Multicellular Alberta Hailstorm. Reprint, 7th Conference on Severe Local Storms, Amer. Meteor. Soc., 63-70.

Shenk, W.E., 1973: Cloud-top Height Variations of Strong Convective Cells. Reprint, 8th Conference on Severe Local Storms, Amer. Meteor. Soc., 80-83.

Smith, E.A., 1975: The McIDAS System, IEEE Transactions on Geoscience Electronics, GE-13.

Storm Data, May 1977: Environmental Data Service, Asheville, North Carolina.

Umenhofer, T.A., 1975: Overshooting Behavior of Three Tornado Producing Thunderstorms. Reprint, 9th Conference on Severe Local Storms, Amer. Meteor. Soc., 96-99.

FIGURES

TABLES

CHAPTER IV

GLOBAL WINDS, BY TRACKING METEOSAT WATER VAPOR PATTERNS

Larry Richard Johnson

ABSTRACT

Geostationary satellite images of water vapor fields show promise as tracers of air motion, even in cloud-free regions. In this study, wind vectors are calculated, using Meteosat water vapor images as passive tracers of air motion. Seven hundred and eighty-one individual wind vectors are obtained for the earth-disc view seen by Meteosat; this is nearly total and homogeneous spatial coverage, even in clear regions. A sample of these vectors is compared to radiosonde winds, yielding accuracies at least as good as from cloud-drift winds.

These winds represent tropospheric motions, but more precise height assignments are needed. Useful heights can be estimated for large scale area averages and for macroscale horizontal depictions, but they are not adequate for the vertical placement of wind vectors in baroclinic zones or in subsynoptic activity. Application of the water vapor sensor on the other geostationary satellites could allow accurate stereographic height estimates.

I. INTRODUCTION

Since the development of the geostationary satellite in the 1960's, examples of accurate cloud tracking have been successfully demonstrated, notably by Suomi and Parent (1967), Smith and Phillips (1972), Bauer (1976), Suchman and Martin (1976) and others. Useful cloud-motion vectors are now provided on a large scale, both operationally and in a research mode, to supplement conventionally-obtained observations. Generally, in areas where these cloud-motion observations can be derived, the spatial and temporal resolution of the winds are quite adequate. Gaps still do exist in cloud-free areas, suggesting an overall sampling bias toward stronger winds, upward motion, or cloud-covered areas (Hinton, 1977). This bias, or spatial aliasing, probably extends to geographic regions which favor the presence or formation of clouds, such as normal subtropical jet source regions.

Water vapor fields, derived from 6.7 micrometer water vapor channel radiometers aboard the Nimbus polar-orbiting series of meteorological spacecraft,

have been used for indicating the upper tropospheric field of motion (Allison et al., 1972; Steranka et al., 1973; and Mosher, 1976). In fact, the motion of these fields can be traced through time, providing wind measurements in cloud-free areas void of upper-air weather observations. This is important, since much of the earth's area falls into this category, particularly the subtropics, where the belt between 30 degrees north latitude and 30 degrees south latitude has comparatively fewer observations.

This study explores a new resource--the application of a 5.7-7.1 micrometer water vapor sensor to a European geostationary meteorological satellite, Meteosat-1. (For full details on Meteosat, refer to Appendix A.) The sensor offers increased spatial (5 km vice 25 km) and temporal (1/2 hr vice 12 hrs) resolution over the Nimbus data and provides the first opportunity to continuously observe these high resolution water vapor fields from a geostationary perspective (36,000 km above the crossing point of the equator and the Greenwich meridian). This is particularly useful in tropical regions, where polar orbiting satellites provide their poorest sampling.

The second section will document this research effort: Part A introduces the satellite-sensor combination and Part B describes the image data used for the study. Part C focuses on the creation of a wind vector data set from the water vapor images. It will demonstrate that accurate winds are obtained over virtually the entire viewing area of the satellite, regardless of cloud amount. Further, they are obtained from a weather-independent observation scheme, so they do much to approach a zero-bias wind data set. This lends the data to statistical averaging for climatological use. In part D, the question of height assignments is treated. Incorrect height estimates in a hyperbaroclinic zone would probably negate the effects of increased data coverage; it is therefore critical to seek as precise as precise an estimate as possible. Three examples of differing height accuracy requirements will be illustrated: First, where a knowledge of the water vapor weighting function is sufficient; second, where image calibration and a climatological standard atmosphere will provide a reasonable mapped height field; and third, where intense baroclinicity, sub-synoptic severe weather events, or small-scale image analysis requires height resolution not currently available. New methods should be investigated to improve upon current height accuracies. As an example, the application of the water vapor sensor to other geostationary meteorological satellites could provide the opportunity for accurate real time stereographic calculations of image heights.

The final section will summarize the evidence to show why the water vapor-derived winds have such potential value for future generations of geostationary meteorological platforms. The possibility of global winds at accurately-known heights would be of great benefit for meteorological applications, particularly considering the recently increased emphasis placed on understanding the global climate.

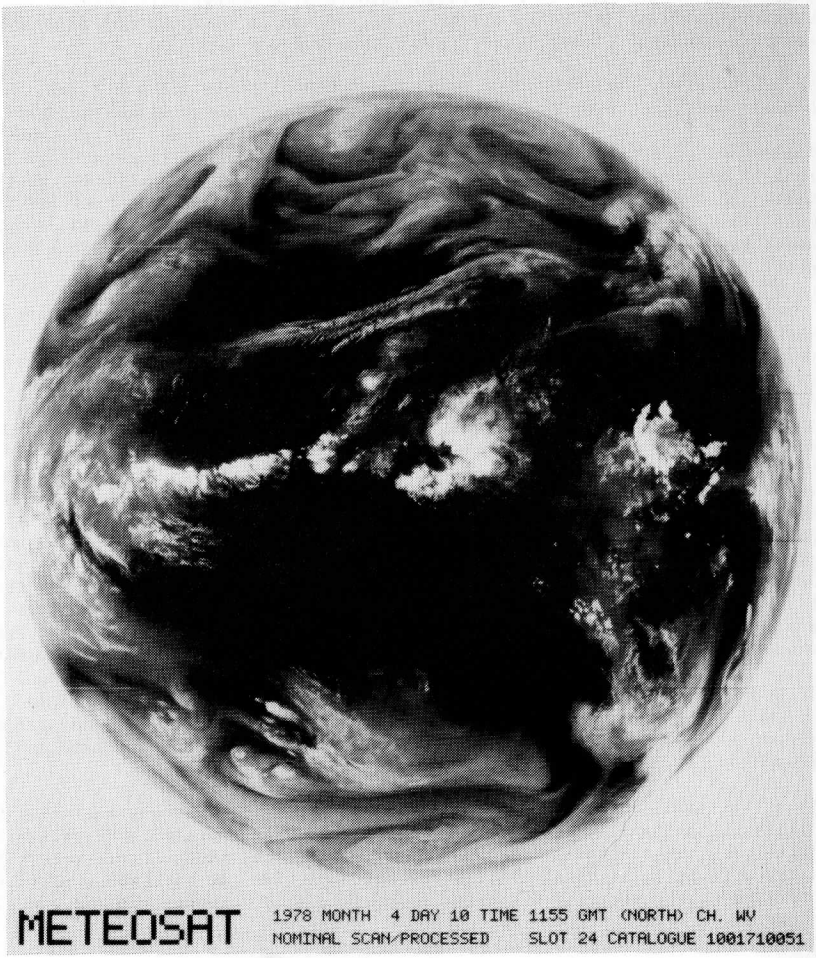

Figure IV.1 A typical water vapor image.

II. THE WIND VECTOR CALCULATIONS

Figure IV.1 is a Meteosat water vapor image obtained in April 1978. This startling perspective of the atmosphere reveals a filmy water vapor continuum, particularly in the mid- to high-latitudes, in which many different scales and waveforms coexist and intertwine. There also appears to be occasional coupling between tropical convective activity and mid-latitude storm systems. In general, the atmosphere appears quite complex, with interactions not normally seen using other forms of data.

A. The Satellite-Sensor Combination.

Meteosat-1 is one component of a global network of five geostationary meteorological satellites arranged in near-symmetric equatorial orbit, but is the only one with a water vapor channel. It was launched on 23 November 1977 from Cape Canaveral, Florida, and is operated by the European Space Agency (ESA). Located approximately 36,000 km above the equator and the Greenwich meridian, it overlooks all of Africa and the Atlantic Ocean, most of Europe and eastern South America. Appendix A describes Meteosat-1 system details and strikes comparisons with the U.S. GOES satellites.

The system component of interest here is the 5.7-7.1 micrometer water vapor absorption channel. This channel senses tropospheric water vapor emissions and produces mapped images for the earth's disc viewed by the satellite. Figure IV.2 shows the atmospheric emission spectrum, notably the region sampled by the water vapor sensor.

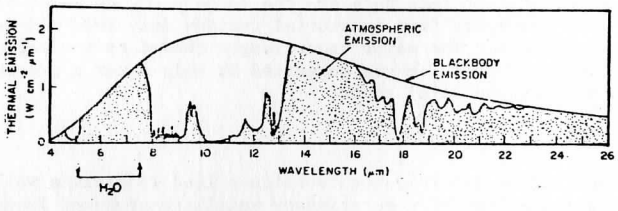

Figure IV. 2. Spectral distribution of radiation emitted by the atmosphere compared to that emitted by a black vapor body at the same temperature. Note the water vapor emission region sampled by the 5.7-7.1 micrometer radiometer. (From Coulson, 1975)

The energy received at the sensor will be representative of the mean black body temperature of the water vapor emissions. Since this involves a layer of moisture, some emissions will be colder where the layer is at higher altitudes, and some will be warmer when the layer is lower. The vertical

distribution of moisture is not likely to be homogeneous; rather, it will tend to be concentrated along selected isentropic surfaces. The temperature seen by the sensor need not be at the midpoint of the moisture layer.

In the water vapor images, bright scenes will represent colder temperatures, thereby indicating high, dense moisture fields (and often cloudiness). Conversely, dark areas will represent warmer temperatures from lower levels, suggesting shallow moisture layers. Since this water vapor mass tends to be conservative, streaks of water vapor can be traced as they moved along or through their isentropic paths. The time rate of change of a moisture field would indicate rising motion for increasing brightness and subsidence for decreasing brightness.

B. The Data Set

This study was based on a data set contributed by J. Morgan of ESA (Houghton and Suomi, 1978). Ten raw data tapes of water vapor (5.7-7.1 micrometer) and "window" (10.5-12.5 micrometer) images for the period 2100 GMT 24 April to 0130 GMT 25 April 1978 comprised the data set. All wind vector calculations were made using three consecutive water vapor images centered on 2300 GMT. This also provided relatively easy comparison with 0000 GMT radiosonde data.

As Figure IV.3 shows, the most striking feature of the water vapor, as compared to the window channel, is the continuous nature of the moisture fields. Mid- and high-tropospheric circulation patterns are suggested a priori from time-sequence water vapor images. Perhaps the most interesting meteorological features of this data are the large areas of moist high-tropospheric mass transport from equatorial regions deep into mid-latitude baroclinic disturbances. The water vapor images showed this clearly, but comparable infrared "window" images suggested it only after a preview was obtained from viewing the water vapor.

C. The Wind Calculation Method

Modern interactive man-computer techniques lend themselves well to the quantitative investigation of geostationary satellite-produced images, so the interactive capability of the Man-computer Interactive Data Access System (McIDAS) of the University of Wisconsin-Madison Space Science and Engineering Center (SSEC) was ideal as the prime investigative tool used for this study. The McIDAS system (Suomi, 1975; Smith, 1975; Chatters and Suomi, 1975) has an inter-active capability involving imagery storage, processing, and display on a mini/midi-size computer system. A meteorologist-operator, using a large repertoire of flexible commands, carries an image set through accurate navigation, enhancement, loop construction, and wind vector calculations, all the while viewing the product of his labors on a cathode ray tube (CRT).

The McIDAS system was essentially developed around the U.S. ATS and GOES satellite programs, so certain dissimilarities in the Meteosat system had to be satisfied. The different scan and spin directions of the spacecraft, the

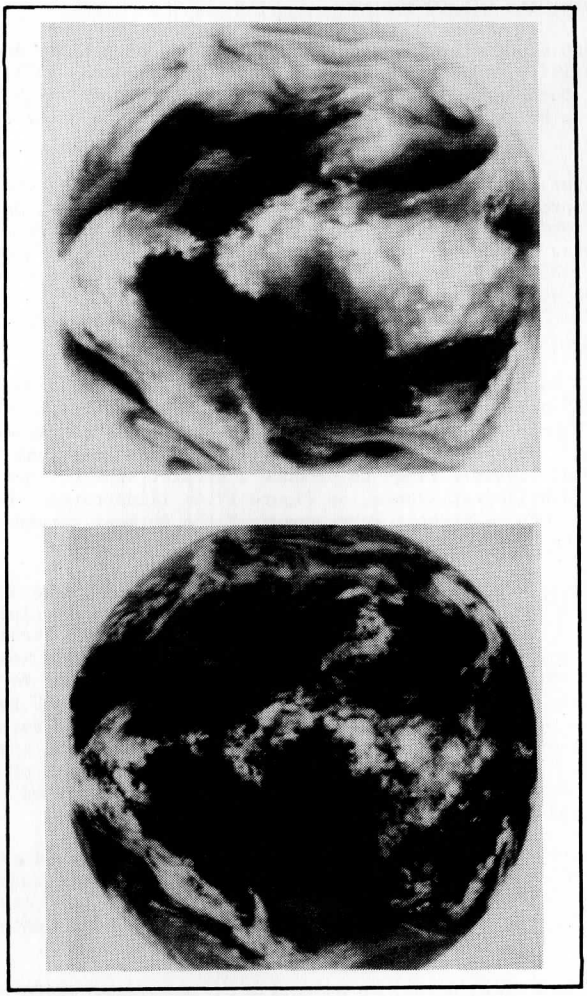

Figure IV.3 Comparison of the 5.7-7.1 micrometer water vapor imagery (top), with the coincident 10.5-12.5 micrometer "window" region imagery (bottom). Data are for 2300 GMT 24 April 1978.

dissimilar line count and timing, and the problems of accurate navigation without visual imagery (a common mode when the water vapor channel is operative) are examples. After resolving these complications, calculation of wind vectors was begun, using the WINDCO system.

The WINDCO cloud tracking system on McIDAS has been amply documented (Smith and Phillips, 1972; Chatters and Suomi, 1975; Smith, 1975). Studies by Bauer (1976), Suchman and Martin (1976) and others have shown that cloud drift winds can be as accurate as in situ measurements, such as radiosonde-derived winds.

Water vapor data form a passive tracer from which wind vectors can be derived. The process requires care, since water vapor fields, particularly in subsident regions, are quite "fuzzy" or "flat"; that is, they form a continuum, rather than a random array of discrete elements, and the gradient may be very slight. The tracking of features imbedded in this field takes on an element of subjectivity not experienced when tracking low level discreet cumulus clouds. Image enhancement techniques were therefore required and used to bring out the fine structure of the water vapor.

Figure IV.4a is a close-up of the subtropical South Atlantic area. The image is "flat" because it has a low contrast ratio; the brightest and darkest returns occupy only 20% of the total possible brightness range, as shown in the brightness histogram of Figure IV.4b. Image enhancement can "stretch" this across the total possible range to produce a greater apparent contrast between the darkest and brightest scenes, as Figure IV.4c illustrates. Other options are available, such as greater enhancement of the darkest returns (Figure IV.4d) or of the brightest ones.

The subjective nature of tracking the water vapor streaks and filaments required manual target identification. Therefore the single pixel (SP) tracking method was used for all wind vector calculations. These calculations were done using a horizontal image resolution of 10 km. This was chosen because the 5 km basic resolution: (1) involved considerably more time and expense to process, and (2) had an erratic "grainy" or "noisy" apearance. This latter problem may have been a manifestation of interference patterns documented in the ESA Meteosat-1 Calibration Report (ESA, 1979). At the time these data were collected, one regular pattern at a recurring wavelength of 2.5 picture elements and one random white noise pattern had been identified through spectral analysis.

The selection of 10 km resolution data necessitated dividing the earth's disc into seven overlapping areas. The overlap allowed independent intra-comparision of wind vectors calculated near the edges of each area, thereby providing an informal quality control mechanism as the wind vectors were calculated.

Based on experimentation, an objective of 100 edited winds per area was established as a minimum requirement to insure representativeness, sufficiency

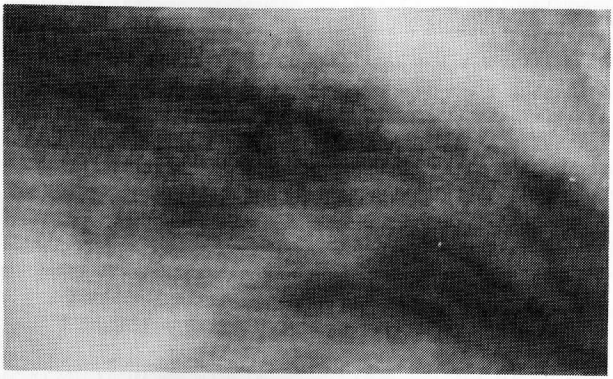

Figure IV 4a. Original water vapor image without image enhancement.

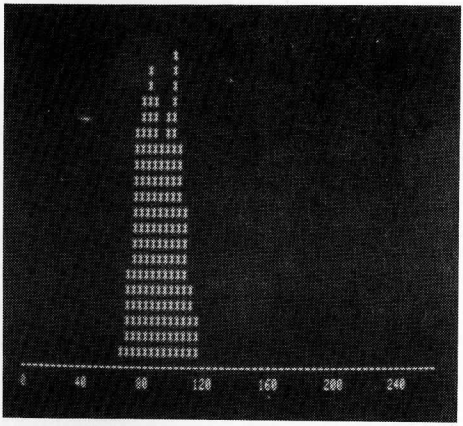

Figure IV.4b. Brightness histogram of image in Figure IV.4a. Entire brightness range is compressed into 20% of the total possible range.

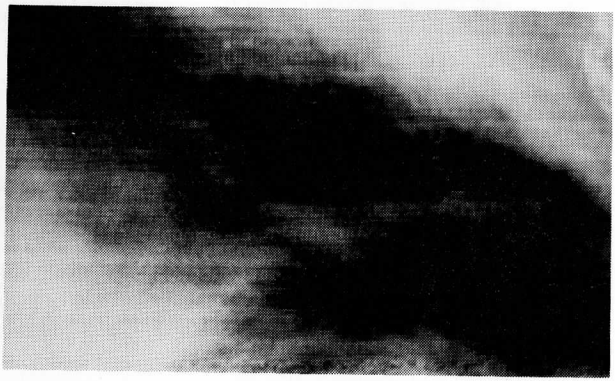

Figure IV.4c. Same as Figure 4a, except image enhancement applied.

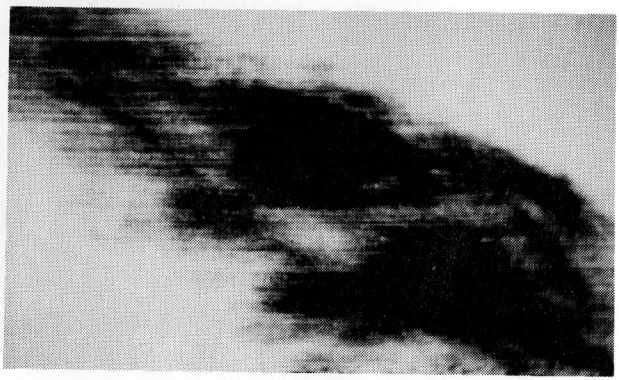

Figure IV.4d. Same as Figure IV.4c, except stronger image enhancement applied to darkest scenes.

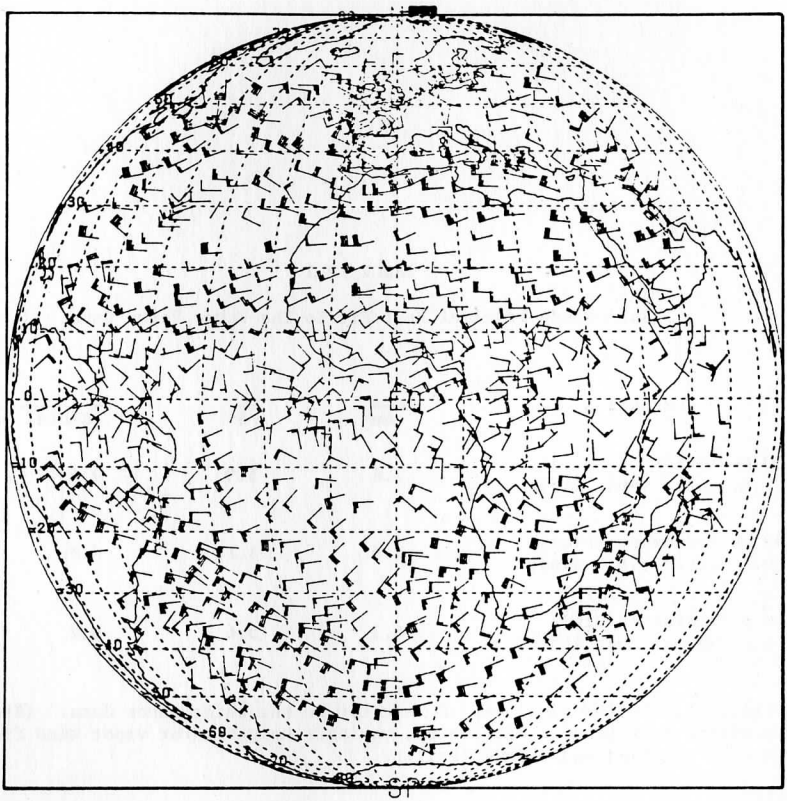

Figure IV.5. The final water vapor-derived wind set, plottted on the earth-disc viewed by Meteosat.

TABLE IV.1

Radiosonde Level of Best Fit To The Water Vapor Data

COMPARISON	$\overline{\Delta u}$	$\overline{\Delta v}$	$\overline{\Delta \text{total vel.}}$
300 mb radiosonde winds v.s. water vapor winds	7.6	5.9	9.6
400 mb radiosonde winds v.s. water vapor winds	4.6	5.1	6.9
500 mb radisonde winds v.s. water vapor winds	6.1	5.6	8.2

Table IV.1. Radiosonde level of best fit to the water vapor data. (Absolute rms differences (m/sec) between the variable-height water vapor wind field and each standard radiosonde level)

and homogeneity of data coverage. Generally, no winds were calculated for earth-satellite angles greater than 55 degrees. Random comparisons between "window" and water vapor-derived wind vectors were made throughout the wind data set generation, and there was consistently good agreement between the two.

Finally, the seven areas were merged, and 1823 total vectors had been calculated, which were then temporally averaged to produce 911 point winds. These were further edited for quality and reproducibility to a final 781 individual wind vectors for the full earth-disc view. More vectors could easily have been calculated.

Figure IV.5 shows this final water vapor-derived wind vector data set. There is nearly complete and homogeneous spatial coverage, regardless of geographical location or of cloud amount.

D. Wind Vector Quality and Limitations

Statements concerning the accuracy of water vapor winds must consider the differences in vector heights caused by the varying altitudes and layer thicknesses of the tracked moisture fields. This is a more difficult problem than the similar task of assigning heights to cirrus or cumulus cloud-derived wind vectors. It can be approached with varying degrees of accuracy, depending on user applications. The following are three possible examples:

Example 1: Since procedures for tracking the water vapor images are similar to cloud-tracking procedures, the results of cloud-tracking quality assessments are worth noting. Bauer (1976) found that rms differences between cloud-drift and radiosonde winds were about 6.4 m/sec for total velocity. Suchman and Martin (1976) determined accuracies of 8.9 m/sec for cirrus cloud comparisons.

Using a radiosonde data-rich section of Europe, brief comparisons were made between the variable-level water vapor-derived wind set and three standard radiosonde levels, at 300, 400, and 500 mb. By assuming the water vapor winds were at the same level as the radiosonde data, the radiosonde level of best fit could be found. Table IV.1 summarizes this comparison: The 400 mb level provided the best fit to the water vapor data, with a mean rms difference of 6.9 m/sec for total velocities. This suggests that 400 mb is probably a practical height assignment for large-scale statistical studies involving mean values, rather than point-by-point comparisons. (If the water vapor heights were known accurately, they could then be compared to equivalent-level radiosonde winds, and much smaller rms differences would be expected.)

Example 2: Large-scale horizontal mapping of the image height field can be accomplished through the use of radiometric image calibration data prepared by ESA (Morgan, 1979; ESA,1979). These data, in the form of a "calibration curve" (Figure IV.6), permit conversion of radiometric image brightness values to black body temperatures. These temperatures can then be converted to height

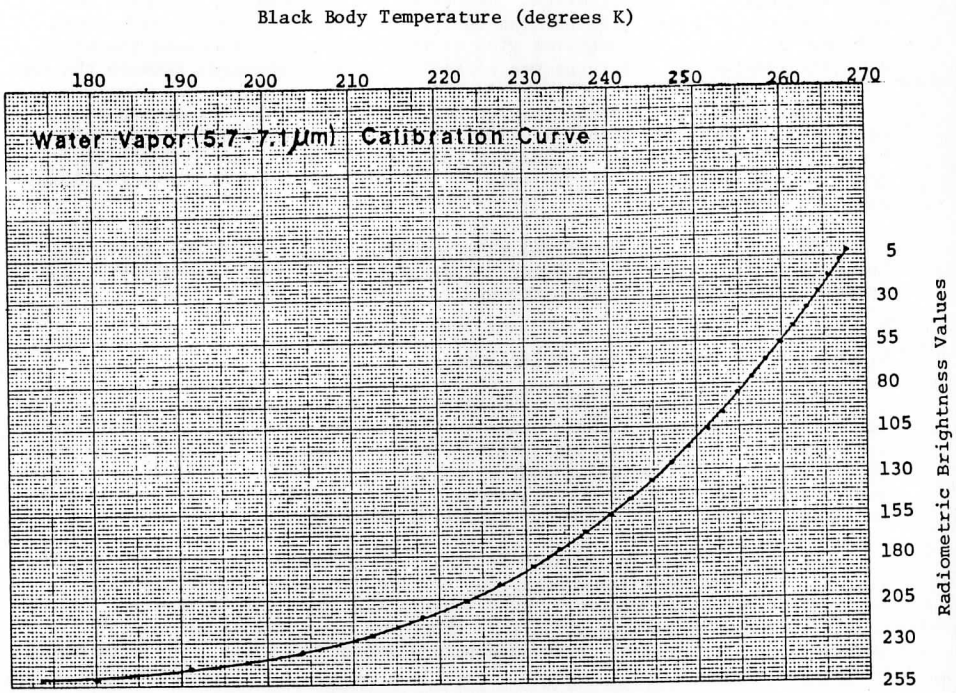

Figure IV.6. The 5.7-7.1 micrometer calibration curve for conversion of radiometric brightness to Planck-function black-body temperatures. (From ESA, 1978)

values through the use of a latitudinally-corrected standard atmosphere. This method relies on the principle of the water vapor weighting function and assumes a fairly uniform distribution of moisture about the mean layer height. This is probably realistic in widespread subsident areas, but is incorrect in convective or baroclinic regions.

The technique was applied to the water vapor imagery, and the resulting 2300Z image height depiction is shown in Figure IV.7. This depiction, when compared to the image in Figure IV.4, seems adequate as a large-scale, gross-resolution estimate, but little reliance could be placed on height values derived in active weather regions.

Example 3: For smaller-scale studies involving wind calculations at individual points, more precise height estimates are necessary. This is particularly true of hyperbaroclinic regions or subsynoptic severe storm systems. Wind vectors calculated in regions of strong vertical wind shear require improved height discrimination, since erroneous height assignments would likely negate the data's value. To demonstrate this point, a comparison was made of vertically-adjacent radiosonde levels over Europe. Using the 300, 400 and 500 mb level winds, a mean rms difference of 7.4 m/sec was found between consecutive levels. Much larger vertical wind shears would be expected in smaller scale hyperbaroclinic zones, demonstrating the critical necessity for accurate height assignments to wind vectors generated in these areas.

Even the water vapor weighting function (Figure IV.8), affords no hope at all for assigning precise height values to strongly baroclinic systems. The highly nonhomogeneous distribution of moisture in baroclinic systems, coupled with the broadness of that weighting function, limits its application to large-scale gross-resolution estimates of image heights.

It appears, then, that large-scale gross-resolution height assignments can be made for the water vapor wind data, but based on these three examples, "meteorologically active" regions or subsynoptic scale analysis will require a more sophisticated technique. If the data are to be given real-time use as a supplement to existing data sources, and if precise height assignments are necessary, some other means of providing it will have to be devised.

Application of the water vapor sensor to other geostationary meteorological satellites, for example, would permit real-time use of the more accurate stereographic height determination technique (Bryson, 1978).

III. SUMMARY AND CONCLUSIONS

The water vapor-derived wind set in Figure IV.5 speaks for itself. This type of continuous data coverage on a global scale would have a major impact on meteorology. These observations have been derived without regard to existing cloud amounts, and provide nearly total and homogeneous spatial coverage of the tropospheric area viewed by Meteosat. Accuracies of these vectors,

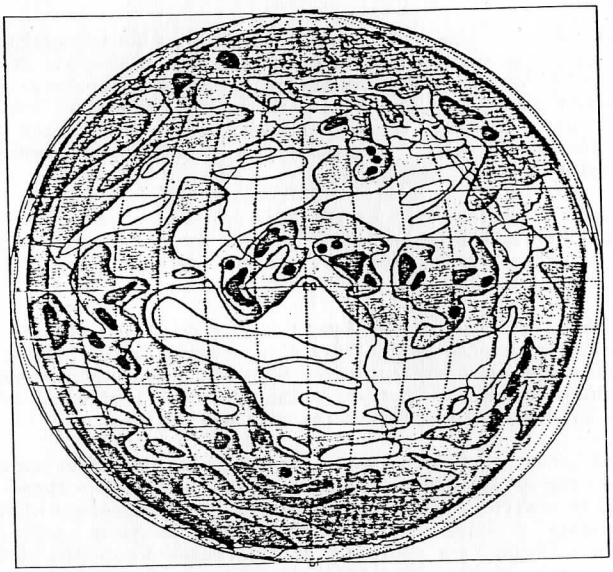

Figure IV.7. Calculated image height field, averaged to the nearest 100 mb layer.

LEGEND:

200 mb 300 mb 400 mb 500 mb 600 mb

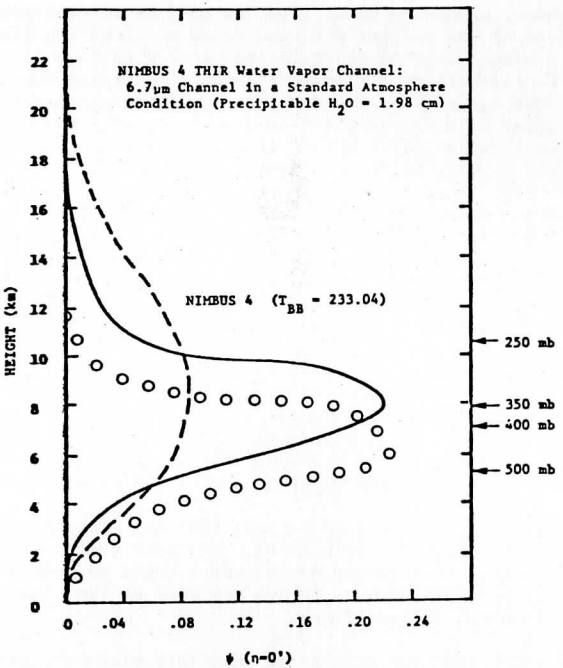

Figure IV.8. A plot of the weighting function, Ψ, showing the atmospheric emission distribution contribution at various altitudes in the 6.7 micrometer channel.

——— mean layer profile

– – – – alternative possibility based on greater vertical distribution of the moisture.

o o o o alternative possibility based on lower-altitude moisture layer.

(From Steranka et al. (1973), with modifications)

compared to radiosondes, appear to be at least as good as cloud-tracked winds. Further, they are free of the spatial aliasing found in cloud tracking and of localized geographic bias. This lends the water vapor wind data to climatological averaging, since there is little likelihood of aliasing the statistical conclusions. The key problem, however, is that of adequate height determination. In areas of large vertical wind shear or nonhomogeneous moisture distribution, heights are particularly hard to estimate. For real time data application, this is significant.

Routine, continuous water vapor observations, from the global system of geostationary satellites, would provide an excellent diagnostic capability over those portions of the earth where few observations now exist. The tropics are especially important, since they form the "heat engine" which drives the global circulation system. The ability to continuously monitor this region can bring meteorologists closer to understanding the earth's climate.

Even in mid-latitudes, water vapor-derived winds can improve upon existing data. Figure IV.1 clearly illustrates the fine structure of mid-latitude hyperbaroclinic zones. Water vapor winds can be selectively calculated at sufficient data density to provide a more refined description of these zones' structures. If the height of each vector could be determined accurately, a high-resolution three-dimensional representation could be constructed.

No method currently exists for precise real time calculations of water vapor image heights in highly baroclinic areas. Stereographic techniques might be a solution to this problem--an option which would be available if the water vapor sensor were included in future upgrades to the total system of geostationary meteorological satellites.

This study has shown that the ability to calculate clear-sky wind vectors, the absence of a spatial aliasing problem, the potential for increased discrimination of hyperbaroclinic zones, and the opportunity for more accurate image height estimates, all provide excellent reasons why the water vapor sensor has such potential for future generations of geostationary meteorological satellites.

APPENDIX A

Meteosat-1 Details

(*) indicates that comparative GOES data follows.

General

Program Manager	European Space Agency (ESA)
Controller	European Space Operations Center (ESOC)
Central Communications Site	Michelstadt, F. R. Germany

Vehicle

Launch Date	0130 GMT, 23 November 1977
Launch Site	Cape Canaveral, Florida, USA
Booster	Delta 2914
Life Expectancy	3 years
Apogee	35,692 km
Perigee	34,913 km
Subpoint	0 degrees latitude/0 degrees longitude
Spin Rate	100 rpm
*Spin Direction	East to West
*Scan Period	25 minutes
*Scan Direction	South to North
Image Interval	30 minutes

Sensors	Visible	IR(window)	IR(water vapor)
*Radiometer (micrometers)	0.4-1.1	10.5-12.5	5.7-7.1
*Resolution (kilometers)	**2.5	5.0	5.0
#Scan Lines/Image	***5000	2500	2500
Elements/Line	5000	2500	2500

Notes

** Resolution is achieved through 2-channel parallel scanning. Water vapor channel is activated at the expense of one of these channels. Visible resolution then decreases to 5.0 km north-south (across scan), but remains 2.5 km east-west (along scan).

*** May be reduced to 2500 scan lines/image. See note (**).

U.S. GOES Comparisons

Vehicle

*Spin Direction	West to East
*Scan Period	18.2 minutes
*Scan Direction	North to South

Sensors	Visible	IR(window)
*Radiometer (micrometers)	0.55-0.70	10.5-12.6
*Resolution (kilometers)	1	8
*Scan Lines/Image	****14,568	1,821

Notes

**** Resolution is achieved through 8-channel parallel scanning.

Reference: ESA (1978, 1979); Morel et al. (1978); Morgan (1978); Gatland (1978a, 1978b); Corbell et al. (1976).

REFERENCES

Allison, L. J., J. Steranka, G. T. Cherrix and E. Hilsenrath, 1972: Meteorological Applications of the Nimbus 4 Temperature-Humidity Infrared Radiometer, 6.7 micron Channel Data, Bull. Amer. Meteor. Soc., 59, 711-714.

Bauer, K. G., 1976: A comparison of Cloud Motion Winds with Coinciding Radiosonde Winds, Mon. Wea. Rev., 104, 922-931.

Bryson, W. R., 1978: Cloud Height Determination from Geosynchronous Satellite Images, Ph.D. Thesis, University of Wisconsin-Madison.

Chatters, G. C., and V. E. Suomi, 1975: The Applications of McIDAS, IEEE Transactions Geosci. Electronics, GE-13(3), 137-146.

Corbell, R. P., C. J. Callahan, and W. J. Kotsch, 1976: The GOES/SMS User's Guide, Nov. 1976, 118 pp.

Coulson, K. L., 1975: Solar and Terrestrial Radiation, Academic Press, p. 253.

Dubin, M., A. R. Hull, K. S. W. Champion, Chmn, 1976: The U. S. Standard Atmosphere, 1976, NASA, NOAA, USAF, Supt of Docs., Washington, D.C., 227 pp.

European Space Agency (ESA), 1978: Introduction to the Meteosat System, Meteosat Data Management Department, European Space Operations Centre, European Space Agency, Issue 1, Nov. 1978.

_____, 1979: Meteosat 1 Calibration Report, Issue 3, Meteorological Data Management Department, European Space Operations Centre, European Space Agency.

Gatland, K.W., Ed., 1978a: Europe's Weather Satellite, Spaceflight, The British Interplanetary Society, 20, Feb. 1978, 41, 48.

_____, 1978b: Meteosat: Europe's Geostationary Weather Satellite, Spaceflight, The British Interplanetary Society, 20, Apr. 1978, 127-134.

Haupt, I., 1977: Meteosat-der Erste Europäische Wettersatellit, Beilage zur Berliner Wetterkarte, des Instituts für Meteorologie, der Freien Universität Berlin, Dec. 1977, 2-6.

Hinton, B. B., 1977: Climatology Based on Winds Derived from Cloud Motions, Studies of Soundings and Imaging Measurements, Final Scientific Report on NAS5-21798, Space Science and Engineering Center, University of Wisconsin-Madison, 231-273.

Houghton, D. D., and V. E. Suomi, 1978: Information Content of Satellite Images, Bull. Amer. Meteor. Soc., 59, 1614-1617.

Howard, J. N., 1965: Transmission and Detection of Infrared Radiation, Handbook of Geophysics and Space Environments, Air Force Cambridge Research Laboratories, Office of Aerospace Research, USAF, 10.1-10.6.

Lorenz, E. N., 1967: The Nature and Theory of the General Circulation of the Atmosphere, No. 218, TP 115, World Meteorological Organization, 161 pp.

_____, 1969: The Nature of the Global Circulation of the Atmosphere: A Present View, The Global Circulation of the Atmosphere, Royal Meteorological Society, 3-23.

Mancuso, R. L., and R. M. Endlich, 1973: User's Manual, Wind Editing and Analysis Program, (WEAP-1A), Stanford Research Institute.

Morgan, J., 1978: Meteosat-1 in Orbit, WMO Bull., 27, 250-253.

_____, 1979: Personal Communication, (Meteorological Operations Manager, Meteosat Data Management Dept., European Space Operations Centre, European Space Agency), 19 Feb. 1979.

Morel, P., M. Desbois, and G. Szejwach, 1978: A New Insight into the Troposphere with the Water Vapor Channel of Meteosat, Bull. Amer. Meteor. Soc., 59, 711-714.

Mosher, F. R., 1977: Feasibility of Using Water Vapor as a Tracer to Obtain Winds from Satellite Observations, Studies of Soundings and Imaging Measurements, Final Scientific Report on NAS5-21798 (1974-6), Space Science and Engineering Center, University of Wisconsin-Madison, 1977.

_____, 1979: Cloud Drift Winds from Geostationary Satellites, Systems and Techniques for Synoptic Windfinding Issue, Atmospheric Technology, (NCAR), No. 10, Winter 1978-79, 53-60.

Palmen, E., and C. W. Newton, 1969: Atmospheric Circulation Systems (Their Structure and Physical Interpretation), Academic Press, 603 pp.

Phillips, D. and E. Smith, 1972: WINDCO: An Interactive System for Obtaining Accurate Cloud Motions from Geostationary Satellite Spin Scan Pictures, Measurements from Scientific Platforms, Annual Scientific Report on NAS5-11542, 1970-1, Space Science and Engineering Center, University of Wisconsin-Madison, 1972, 1-51.

Riehl, H., 1969: Mechanisms of the General Circulation of the Troposphere, World Survey of Climatology, Vol. 2, Elsevier Publishing Co., 1-37.

Rodgers, E. B., V. V. Salomonson, and H. Lee Kyle, 1976: Upper Tropospheric Dynamics as Reflected in Nimbus 4 THIR 6.7 micrometer Data, Journal of Geophysical Research, 81, 5749-5758.

Rossby, C. G., 1941: The Scientific Basis of Modern Meteorology, Climate and Man: Yearbook of Agriculture, U. S. Dept. of Agriculture, Washington, D. C., 1941, 599-655.

_____, 1959: Current Problems in Meteorology, The Atmosphere and the Sea in Motion, Scientific Contributions to the Rossby Memorial Volume, The Rockefeller Institute Press, in assoc. with Oxford University Press, 9-50.

Sabins, F. F., Jr., 1978: Remote Sensing Principles and Interpretation, Freeman and Co., 429 pp.

Smith, E. A., and D. R. Phillips, 1972: Automated Cloud Tracking Using Precisely Aligned Digital ATS Pictures, IEEE Trans. on Computers, C-21, No. 7, July 1972, 715-729.

_____, 1975: The McIDAS System, IEEE Transactions Geosci. Electron., GE-13(3), 123-136.

Steranka, J., L. J. Allison, and V. V. Salomonson, 1973: Application of Nimbus 4 THIR 6.7 micrometer Observations to Regional and Global Moisture and Wind field Analysis, J. Applied Meteor., 12, 386-395.

Suchman, D., and D. W. Martin, 1976: Wind Sets from SMS Images: An Assessment of Quality for GATE, J. Applied Meteor., 15, 1265-1278.

Suomi, V. E. and R. J. Parent, 1967: Proposal to NASA for an ATS Technological Experiment, Unpublished.

_____, 1975: Man-computer Interactive Data Access System, (McIDAS), Final Report Contract NAS 5-23296 for Goddard Space Flight Center, Space Science and Engineering Center, University of Wisconsin-Madison.

LIST OF FIGURES

LIST OF TABLES

CHAPTER V

A DERIVED 850 MILLIBAR CHART FOR THE WESTERN UNITED STATES AND SOME DIAGNOSTIC USES *

Carl S. Bullock

and

John A. Young

ABSTRACT

Various methods for representing detailed synoptic-scale fields near the earth's surface in elevated terrain are examined. Special attention is given to techniques which yield realistic horizontal pressure-gradient forces based upon surface data alone. An 850 mb chart is derived for the western United States using hourly surface observations and a simple reduction technique. This chart is found to (1) be more representative of surface temperature and pressure gradients than the sea-level pressure map, (2) to possess superior space-time resolution compared to the National Meteorological Center 850 mb chart produced from upper-air stations, and (3) to be more convenient for dynamical calculations than the sigma (σ = 1) surface map.

The data from the derived 850 mb map are generally realistic and give many meteorological fields that are useful in diagnosis and potentially useful in short range forecasting. These data are dense in space and time allowing high resolution down to the subsynoptic scale. The horizontal pressure-gradient force is obtained from the gradient of the 850 mb height field, in contrast to the sigma system where two variable fields are required and where the surface geostrophic wind is divergent. The derived 850 mb map is greatly superior to the sea-level pressure map for representing pressure gradients and hence is useful for wind forecasting. Calculations of geostrophic and ageostrophic motions are made for case studies; they demonstrate the potential for short range diagnosis and forecasting after improved frictional formulations have been developed.

I. INTRODUCTION

One of the basic problems of synoptic meteorology is proper representation of meteorological fields near the earth's surface. Parameters such as

* This work was partly supported by National Science Foundation Grant ATM 73-06635 to the Department of Meteorology and NOAA Grant 04-158-61 to the Space Science and Engineering Center. The participation of Carl S. Bullock was made possible through a National Weather Service full-time scholarship.

pressure, temperature, water vapor pressure, and wind vary greatly with height; this is especially true of pressure. These data must be reduced to a common level or they must be dealt with in a more complex coordinate system whose surface is at or near the earth's surface.

Traditionally, surface data such as pressure have been reduced to sea level so that data from all stations may be utilized and compared. However, this procedure has serious drawbacks when applied over elevated regions such as the western United States. Little and Vernon (1934, p. 149) have commented:

> "In the study of synoptic maps for the western portion of the United States, especially in connection with airways work, meteorologists repeatedly have been confronted with the imperfect state of the barometry of the plateau region. Probably the most conspicuous examples of the imperfection are to be found in certain instances in which various elements such as wind directions and state of weather indicate the presence of a cyclone over the plateau while the existence of the cyclone is not shown by the sea-level isobars. Other instances have been noted in which the sea-level pressure charts showed enclosed lows over the plateau when their existence was not substantiated either by wind circulation or by other meteorological elements. Indeed, the inaccuracies in the configurations shown by the sea-level pressure charts for the plateau region, particularly for that portion lying to the west of the Continental Divide, tend to lead those who believe in them to the conclusion that the usual concepts of the relationship of various meteorological elements to pressure configurations apply only to a very limited degree over the plateau. However, it is rather to be expected that the dynamic processes involved in producing various types of weather over the plateau are substantially the same as those involved elsewhere."

The reduced sea-level pressure field often does not resemble the "true" pressure field on an elevated horizontal plane near the surface. The following example illustrates why this is so. Suppose there are two stations at the same elevation separated by a mountain range. Suppose further on a given day the station pressure is the same at both stations, but that the surface temperature at one station is colder than at the other. When the two pressures are reduced to sea level the station with the colder surface temperature will almost always have a higher sea-level pressure. In principle, differences in sea-level pressure could also arise from different temperature lapse rates assumed for the two fictitious air columns.

With the problems in reducing pressure to sea level apparent, some meteorologists tried a different approach, "reduction" of surface data to a level other than sea level (the term reduction is commonly used for both upward and downward extrapolation of data). Bigelow (1900-01) was responsible for the standardization of barometry practices for most of North America; he was the first to experiment by reducing surface data to the 3,500 (1067m) and 10,000 foot (3048m) levels (Bigelow, 1904). These reductions were made in

connection with an international cloud observation program.

Meisinger (1922) tried reduction to the 1 and 2 kilometer levels over the central and eastern United States using a reduction scheme whose assumed lapse rate was based on wind direction and speed. This work was based on kite observations of temperature in the free atmosphere. Despite encouraging results during the three month test period, these charts never became operational and plans to extend them to the western United States were never realized. This work was dropped after the untimely death of Dr. Meisinger in 1923 during a balloon research flight.

Little and Vernon (1934) introduced a system of reduction to the 5000 foot (1524m) level to facilitate aviation forecasting in the western United States. The reduction level was changed to 850 mb in the early 1940's. This system was used operationally with very satisfactory results for over 30 years ending in 1967.

In late 1967 Weather Bureau offices in the western United States were polled about discontinuing computed 850 mb heights. An 850 mb chart was being produced at the National Meteorological Center (NMC) in Washington D.C. This chart was available twice daily using data from radiosonde stations. 850 mb heights calculated from surface data were reported only four times daily and required that the user plot and analyze the data. Very few stations responded in favor of continuing these reports, and it was decided to terminate them (Snellman, 1977). It seems unlikely that this would represent a modern opinion, since the calculations and analyses could now be done automatically at a central computer.

Harrison (1957, 1970) has proposed alternative schemes for reduction to sea level based on a rational (versus an empirical) technique. The temperature parameter used in this reduction is a continuous function of station coordinates determined by a least squares method over the area of concern. The horizontal gradient of sea-level pressure thus derived, when combined with precisely specified terms of temperature and station geopotential, is independent of the temperature parameter used for reduction; it also yields the true surface horizontal pressure gradient. It is somewhat analogous to the sigma system in that two terms are necessary to fully define the true surface pressure gradient. This reduction technique has not yet been fully tested having been considered too "radical" by other investigators.

With the advent of numerical weather prediction the sigma (σ) coordinate system (Phillips, 1957) was introduced. In this system the vertical coordinate is pressure normalized by surface pressure. A smoothed representation of the earth's surface is the lowest boundary. The formula for sigma (σ) is:

$$\sigma = p/p_{surface}$$

so that the smoothed earth's surface is represented by $\sigma = 1$. Rather than reduce station pressure to another constant level, the horizontal pressure gradient at locations along the sloping surface of the earth can thus be directly calculated. Sangster (1960) designed his system specifically for this purpose. The problems of reduction at most places are virtually eliminated using this method. There are disadvantages, however. The equations defining geostrophic wind and its vorticity are much more complex than in constant pressure coordinates. At least two fields are required for the horizontal pressure gradient and the geostrophic wind, which is generally divergent in this system. The vorticity on the sigma surface is generally influenced by vertical wind shear in the presence of sloping terrain. The simple relationship between constant pressure height contours and the geostrophic wind does not hold in this system.

The present study reexamines use of the "derived" 850 mb chart. A simple method of reduction is devised. The method may be empirically "tuned" for lapse rate variations by comparing derived heights with radiosonde observations. Several advantages appear: (1) since the 850 mb height is relatively close to most station elevations in the western United States, reduction errors are minimized and the pressure-gradient force from this 850 mb chart is thus much more realistic than that from the sea-level pressure map; (2) the data are relatively dense in space and time, allowing some subsynoptic features to be distinguished; (3) the 850 mb chart is convenient since it is familiar to meteorologists and the height field alone allows easy indication of winds and associated dynamical processes. Advantages (1) and (2) are also found for the sigma system; advantage (3) is unique to the derived 850 mb chart.

The derived 850 mb chart is the basis for several meteorological fields which are investigated later in this work. Geostrophic vorticity is found to be useful in tracking surface circulation centers associated with low and high pressure centers, and changes in vorticity often indicate likely areas of cyclogenesis/cyclolysis. Quasi-geostrophic theory is used to estimate the divergence that could occur above the friction layer based on the 850 mb height field and its changes. An 850 mb potential temperature field is also constructed and is shown to be very useful in frontal analysis. A discussion of the potential applications of these fields in analysis and forecasting is given in the last section. Also, suggestions for improvements in the reduction scheme, data base, etc., are included. Instructions for using the derived 850 mb computer programs at the University of Wisconsin-Madison McIDAS facility also appear in Appendix I.

This study was undertaken with the intent of deriving a useful operational tool. It is based on a chart used by aviation forecasters for many years in the western United States. This study goes beyond the previous work in that the 850 mb height data is used to construct many meteorological fields representative of those near the earth's surface.

With Automation of Field Operations and Services (AFOS) in the National Weather Service, data from surface observations will be readily available for

computer manipulation. It is hoped that this work will serve as the basis for a regional 850 mb software package to supplement the reduced sea-level chart in the western United States.

II. ESTIMATION OF SYNOPTIC SCALE HORIZONTAL PRESSURE GRADIENT FORCE FOR ELEVATED REGIONS

A fundamental problem for surface forecasting is how to obtain accurate representation of fields at or near the surface of the earth, particularly the pressure field. The problem is particularly acute in elevated mountainous regions. In this section the equations for the two main methods in current use (sea-level pressure and the Sangster sigma method) are examined.

All of the terms in the sea-level pressure reduction scheme used in the United States are presented with their physical basis providing a framework for later discussion. Similar terms may be found in most reduction methods. Some of these terms may give rise to spurious components in the reduced sea-level pressure gradient. The basic equations of the Sangster method are also examined. While this method is capable of giving the precise horizontal surface pressure gradient, it is not as convenient as the constant pressure system. The relative merits of the various methods are detailed in this section.

The fundamental equation upon which barometry rests is the hydrostatic approximation, derived for conditions of negligible vertical acceleration. Scale analysis for synoptic systems shows that to a very high degree the atmosphere is in hydrostatic balance, i.e. the gravitational force due to the mass of the air is balanced by the vertical pressure gradient force:

$$\frac{\delta p}{\delta z} = -\rho g.$$

Substituting from the ideal gas law:

$$p = \rho RT$$

and integrating from one pressure to another holding x, y, and t constant:

$$RT_{mv} \ln(p_2/p_1) = (\Phi_1 - \Phi_2). \qquad (1)$$

Here, R = gas constant for dry air, T_{mv} = a mean virtual temperature, Φ = geopotential. T_{mv} is defined (List, 1968, p. 292):

$$T_{mv} = \frac{\int_{p_1}^{p_2} T_v \, d \ln p}{\int_{p_1}^{p_2} d \ln p}$$

Equation (1) is the formula used as the basis for reduction of pressure. By using geopotential, variations of gravity with height and latitude are taken into account. T_{mv} must be specified in order to solve for pressure at a known geopotential level for the geopotential height at a given pressure (1000 mb, 850 mb).

A. Reduction to Sea Level

The sea-level pressure reduction currently used in the United States was originally formulated by Bigelow (1900-01). He stated (p. 25) that the main problem in making these tables was computing T_{mv} which depends upon the complete distribution of T(p) assumed for the fictitious air column:

> "The primary practical difficulty in forming station reduction tables for pressure on a plateau or otherwise elevated region consists in determining the mean temperature of the air column to be substituted for the plateau itself, where an observation of temperature can be made only upon the surface of the ground, and the corresponding sea-level temperature can only be indirectly inferred. If the plateau temperature does not agree with that of a free-air column at the same elevation, in what ratio does it differ from it, and how is the difference to be obtained in any exact way that will not be the result of conjecture merely?"

Generally there are three main components of T_{mv}: (1) T_s, the station temperature argument, (2) an assumed lapse rate, (3) a humidity component. The station temperature argument, T_s, may be further subdivided into two parts: (1) the surface air temperature or some time average of it, (2) a function F. In the United States the average of the current temperature and the temperature 12 hours previous is used. F as defined by the World Meteorological Organization (1964, p. 23) is: "F = a function, in K°, of parameters found to give T_s the desired properties for special orographic situations." Usually the desired property is that the reduced pressure pattern be smooth and the annual variation of mean monthly sea-level pressure fall within a value considered reasonable by the investigator. Components of F may or may not have a physical basis.

The function F, which is part of T_s, is used in the United States sea-level pressure reduction method. Two kinds of adjustments are included in F. There is a correction to the assumed lapse rate, and the so-called plateau correction. Station elevations greater than 305 m require a correction to the assumed lapse rate of 6.5°K per km. The correction depends on geographic location, elevation, and climatological conditions (Saucier, 1955 p. 57):

"In elevated regions where marked extremes of temperature occur, better results are obtained by this procedure than by assuming the lapse rate is a constant. The method which has been used in the United States for finding the relationship between T_s and the lapse rate, or between T_s and $(\overline{T} - T_s)$, is very involved, requiring extensive compilations of comparable data for regions including both high- and low-level stations. The principle used is that the synoptic reduced, sea-level pressures, P_o, for all stations when plotted on a weather map should be self consistent, and yield reasonably smooth isobars in harmony with the prevailing distribution of cyclones and anticyclones, both on a monthly average basis and during extremes of low temperatures. The values of P_o for low stations establish the reference basis to which the values of P_o for high stations must conform since the former are reliable because $Z_s/2$ must be small and discrepancies therein can produce little error in $\overline{T}$."

$\overline{T}$ is the mean temperature of the fictitious air column. Z_s is the station elevation above mean sea level. While it can be argued physically that the mean monthly lapse rate will vary widely from place to place and month to month, the method for determining those variations is strictly empirical. The guiding principle is that the reduced pressure pattern be spatially smooth and the annual variation of reduced pressures for high altitude stations be similar to that for low-lying stations. The lapse rate for a station will depend on its temperature (T_s) through a complicated system of relationships determined statistically at the turn of this century (Bigelow, 1900-01).

The plateau correction is somewhat of a misnomer. It is a correction which is applied to all stations, not just to those on a plateau. The concept of the plateau correction was introduced by Ferrel (1886). He reasoned that the proper temperature to be used in reduction was that of the free-air column replacing the plateau if it could be moved away. He argued further that the temperature of a free-air column changes much less rapidly and its changes are less extreme than those of air at the immediate surface of the plateau. Consequently he reasoned that the surface temperature in summer was too high and that of winter too low compared with the free-air temperature that would exist if the plateau were removed. Use of these strongly varying surface temperatures resulted in reduced sea level pressure differences for elevated stations which showed summer to winter changes 3 or 4 times as great as those for stations near sea level. Feeling that these differences were too great, the plateau correction was applied. According to Harrison (1963, p. 7-7):

"In brief, the correction for the so-called 'plateau effect' is employed so that the amplitude of the annual variation of pressure reduced to sea level shall be approximately the same at all stations in North America, regardless of elevation. If this

correction were omitted, elevated plateau stations (say at 7000 feet on the western plateau region) would report mean monthly reduced pressures which were about 15 mb higher in January than in July. However, sea-level stations in the same latitude yield a typical difference of about 5 mb between these months. Use of the correction for the 'plateau effect' assumes that the reported differences are maintained at about the latter value in all cases."

It is probably true that the surface temperature is subject to greater extremes than that of a free-air column which Ferrel suggests is the proper temperature to use in reduction. However, it is not clear that the average difference in sea level pressure between January and July should be the same for high stations as it is for low stations, especially if the stations are widely separated. The formula for plateau correction (P.C.) in millibars is

$$P.C. = .000210\ (T_s - T_{sn})\ Z_s,$$

where T_{sn} is the annual normal surface air temperature (°C) and Z_s is station elevation (m).

The inclusion of F in T_s and averaging the station temperature decreases the effect of abnormal temperatures. However, true diurnal and annual variations in pressure are often eliminated, according to Harrison (1960, p. 18):

"...experience has shown that the employment of this argument [$(T_s = (T + T_{12})/2 + F)$] causes an apparent 'damping out' of the actual diurnal and annual variations in the pressure field. Thus, the dynamical significance of these variations may be overlooked."

A study by Sangster (1967) of the diurnal variation of surface geostrophic winds over the Great Plains revealed an average diurnal variation of 18 knots (9.3 m/s) during the period studied. The reduced sea-level pressure chart using time-averaged and F-corrected T_s values gave a variation of only 2 knots (1 m/s). Thus, the use of T_s smoothed out real physical variations as well as spurious ones.

In addition to affecting the pressure gradient and therefore the geostrophic wind, centers of high and low pressure may be displaced in the reduction process (Harrison, 1960, p. 16):

"On the basis of the foregoing considerations it is concluded that centers of action cannot be realistically represented or tracked over high landbodies by means of the apparent field of pressure reduced to sea level which involves the assumption of a 'mean virtual temperature of the fictitious air column, T_{mv},' characterized by a variable distribution over space and time."

The second constituent of T_{mv} is an extrapolation of T_s through the fictitious air column. The lapse rate used in the United States is 6.5°K per km. As has been mentioned already a correction to this assumed lapse rate is applied in the F term for stations above 305 meters. The correction differs from station to station (see p. 10).

The third part of T_{mv} is the humidity term. This correction is needed to change the mean column temperature into a virtual temperature. It allows the use of the gas constant of dry air (R) in the hypsometric equation instead of a variable coefficient. This component, like the previous two, is a function of station temperature T_s. A mean moisture content is assumed based on T_s. This component is generally small (less than 1 mb) outside of tropical regions.

The current method of reduction is designed to produce a smooth pressure field. High and low pressure centers will not necessarily be preserved in the reduction process. The true pressure-gradient force near the surface may not be preserved either as vector errors due to the gradient of T_{mv} are introduced. These errors will be discussed in Section V.

B. Alternatives to Reduced Sea Level Pressure

Several alternatives to reduced sea-level pressure have been developed by various investigators. With faster computers, it became feasible to calculate the horizontal pressure-gradient force at the surface of the earth without first reducing the pressure to a common level. Such methods generally employ sigma (σ) surfaces, where sigma replaces pressure as the vertical coordinate. The lowest sigma surface ($\sigma = 1$) represents some smoothed representation of the earth's surface.

Sangster (1960) developed one such method specifically to represent the pressure-gradient force at the earth's surface, based on the altimeter correction system of Bellamy (1945). Simpler and more accurate computations may be obtained by representing pressure and temperature at a station as departures from a standard or reference atmosphere. As formulated by Sangster, the horizontal pressure-gradient force per unit mass in sigma coordinates is:

$$\nabla_p \Phi = \nabla_\sigma D - S_v \nabla_\sigma \Phi_r \qquad (2)$$

where Φ is geopotential height above sea level, Φ_r is geopotential height of reference atmosphere corresponding to given pressure of the sigma surface at that point, $D = \Phi - \Phi_r$; $S_v = (T_v - T_r)/T_r$, the specific virtual temperature anomaly; T_v = virtual temperature; T_r = virtual temperature in the reference atmosphere corresponding to a given pressure of the sigma surface at that point. Note that there are two vector fields required to represent the pressure-gradient force at the $\sigma = 1$ surface. The first term on the

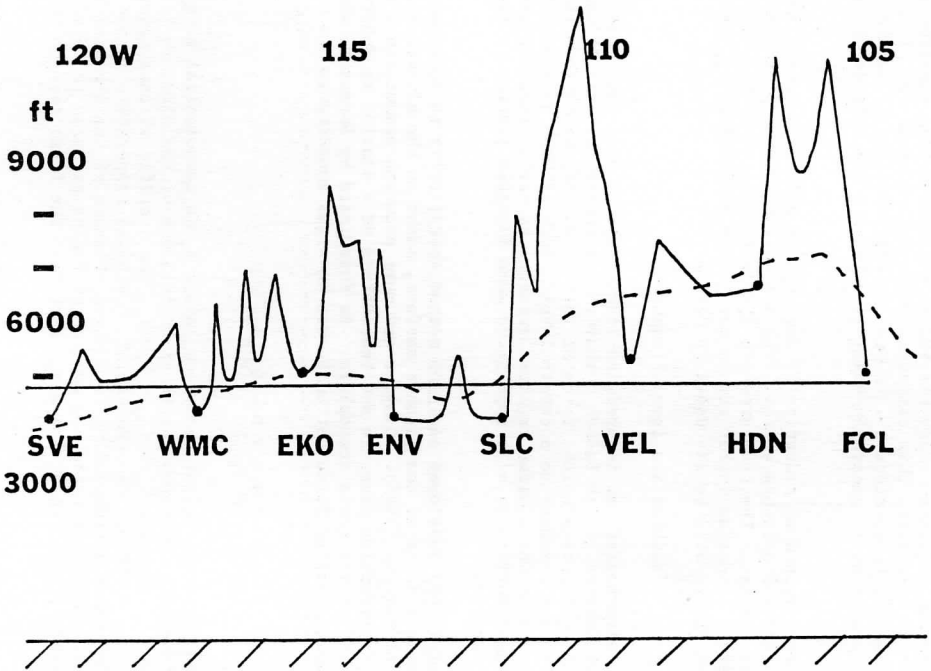

Figure V.1 Relation between earth's surface and meteorological reference surfaces over western U.S. Irregular solid line is actual terrain averaged within 20 miles north and south of 40°40'N. Dashed line is current sigma (σ=1) surface along same latitude. Horizontal lines are 850 mb surface from standard atmosphere and mean sea level, respectively.

righthand side of Equation (2) is the counterpart of the pressure-gradient force expressed in pressure or height coordinates, since it remains even when the terrain is flat. The second term is a vector with direction perpendicular to the lines of constant topographical elevation of the earth's surface; its sense is determined by the sign of S_v. The product g S_v (g from the geopotential term) is a kind of reduced gravity associated with synoptic temperature deviations. The effect of this entire second term is to produce a force directed downhill (uphill) when the temperature anomaly is cold (warm). Another form of Equation (2) may be found in Haltiner (1971, p. 194):

$$\nabla_p \Phi = \nabla_\sigma \Phi + \frac{\partial \Phi}{\partial \sigma} \nabla \sigma .$$

As in the previous equation two variable fields are required for the horizontal surface pressure-gradient force.

Once the temperature departures at the station are determined they must be used to estimate temperature on the smooth sigma representation of the earth's surface. In regions where the actual terrain is reasonably regular this is fairly simple, and the distance between the actual surface and the smoothed sigma representation of the earth's surface is small. This is the case for most of the area east of the Rockies. The problem becomes more difficult where the terrain is irregular. This is illustrated in Figure V.1 for a cross section from northern California to Colorado. The plotted terrain is averaged over a band 40 miles (64 km) wide centered on latitude 40°40' N. This terrain profile is seen to be quite irregular. The dashed line is the current σ=1 surface used in the Sangster method. While the Sangster sigma surface follows the general trend of the actual terrain, it is much smoother. The height of the 850 mb surface in the standard atmosphere is shown as the horizontal line just below 5000 feet (1524 m). The distance through which reduction is required is roughly comparable over-all for the 850 mb surface and the Sangster surface. More importantly, note that both require a much smaller reduction distance than the sea-level pressure chart, so that they are much less sensitive to assumptions about fictitious air columns.

Once the pressure-gradient force is known, the geostrophic wind may be calculated. For the Sangster method this is the geostrophic wind at the sloping earth's surface. From Equation (2) it is given by

$$\vec{V}_g(\sigma = 1) = \frac{1}{f} kx[\nabla_\sigma D - S_v \nabla_\sigma \Phi_r]. \qquad (3)$$

It differs from that on a constant pressure surface in that it is generally divergent. Hence it must be represented by both a stream function and velocity potential (Sangster, 1960). This divergence is not due to the variation of the coriolis parameter or the curvature of the earth. Neglecting these, there still remains divergence in this surface geostrophic wind, which from Equation (2) is

$$\nabla_\sigma \cdot \vec{V}_g = \frac{1}{f} \vec{k} \, (\nabla_\sigma S_v \times \nabla_\sigma \phi_r). \qquad (4)$$

This is most significant when the "isotherms" of S_v cross topographical contours of the earth's surface; it is positive when warm anomalies are found to the left of an observer facing downhill in the Northern Hemisphere. Despite these disadvantages the Sangster method gives the actual surface pressure-gradient force, assuming the $\sigma = 1$ surface is representative.

There is yet another alternative. Instead of reducing station pressure to sea level, one may "reduce" station pressure to a level near the average surface height or pressure for a region. As can be seen from Figure V.1, the 850 mb surface is relatively near the elevation of most stations in the plateau region of the western United States, so that reduction errors are relatively small. While this method will not give the actual pressure gradient at the surface, it usually gives a very close approximation which is superior to the gradient from the sea-level pressure chart. Such a method has the advantage that the gradient of only one scalar field is needed to represent the horizontal pressure-gradient force, and the associated geostrophic wind is essentially nondivergent. Many parameters can easily be calculated from this one field.

Table V.1 summarizes some of the advantages and disadvantages of these various systems. Sea-level pressure is the least advantageous of the three, as it is subject to large errors. The Sangster method is the most accurate but least convenient requiring two variable scalar fields. The 850 mb method is almost as accurate as the Sangster method and is more convenient.

The need for a better pressure-gradient representation than that obtained from sea-level pressure prompted the method outlined for the western United States by Little and Vernon (1934). Tables were constructed for reduction of station pressure to the 5000 foot (1524 m) level. Stations between 3259 feet (993 m) and 6374 feet (1934 m) were used. The 12 hour averaged temperature was employed despite the fact that it produces an oscillation in T_{mv} which does not resemble the true temperature oscillation. This choice was a matter of convenience since this was the temperature argument used for sea-level reduction. They found the most correct diurnal profile was given by,

$$T_s = [2T(t) + T(t - 4) + T(t - 12)]/4;$$

T = station temperature; t = time in hours; T_s = station temperature argument used for reduction. Monthly mean lapse rates were computed for stations from the tables produced by Bigelow (1900-01). A suitable correction for moisture was included in T_{mv}. The plateau correction was not included.

METHOD	REMARKS ON PRESSURE GRADIENT FORCE	NUMBER OF SCALAR FIELDS FOR GEOSTROPHIC WIND	GEOSTROPHIC VORTICITY	GEOSTROPHIC DIVERGENCE	TERRAIN FIELD REQUIRED	REDUCTION DISTANCE
SEA LEVEL PRESSURE	NOT AT EARTH'S SURFACE LARGE ERRORS LIKELY	ONE	LARGE ERRORS	≈ 0	NONE	LARGE
CONSTANT PRESSURE (850)	NOT AT EARTH'S SURFACE SMALL ERROR	ONE	SMALL ERRORS	≈ 0	NONE	SMALL
SIGMA = 1 SURFACE (SANGSTER)	APPROXIMATELY AT EARTH'S SURFACE ERROR DEPENDS ON TERRAIN ROUGHNESS, USUALLY VERY SMALL ON THE SYNOPTIC SCALE	TWO	NOT VERTICAL COMPONENT	$\neq 0$	YES SMOOTHED	SMALL

Table V.1. Summary comparison of the three methods of representing the surface pressure gradient and geostrophic wind.

Pressure fields at 5000 foot (1524 m) were reported as part of the aviation observation beginning in the late 1930's. Since reduction errors were small, the pressure gradient on the 5000 foot chart was representative of that near the surface. The agreement between observed surface winds and the pressure field was much better for the 5000 foot chart than the sea-level pressure chart. In the early 1940's constant height charts were replaced by constant pressure charts, and the 5000 foot chart became the 850 mb chart. 850 mb heights at selected stations were reported with each synoptic observation until late 1967. These data were widely used by aviation forecasters in the western United States through the early 1960's. With the advent of 850 mb charts produced by the National Meteorological Center twice daily, support for continuing the synoptic 850 mb reports dwindled. This was partly due to the fact that, at that time, synoptic reports required plotting and analysis by the local user. The resulting chart was much more detailed than the NMC chart but was obtained at great time expense. Since the NMC chart came ready-made on the facsimile circuit, it replaced the synoptic 850 mb reports in routine forecasting. Thus, convenience of the moment triumphed over utility. Since recent technical advances have made data collection, processing and analysis simpler and essentially do not involve preparation on the local station level, it would appear that use of the NMC 850 mb chart alone no longer possesses an advantage of convenience.

The following chapters contain discussion of techniques for obtaining an 850 mb geopotential field from surface observations and various derived fields which have utility for subsynoptic applications in the western United States.

III. DERIVED 850 MB FIELDS BASED UPON HOURLY SURFACE DATA

The starting point for the reduction method used in this study is a form of the hypsometric equation (Equation 1) similar to that given in the Smithsonian Meteorological Tables (List, 1968, p. 203),

$$(\Phi_2 - \Phi_1) = 67.442\ T_{mv}\ \log_{10}(p_1/p_2).$$

T_{mv} is the mean virtual temperature instead of the adjusted mean virtual temperature used in the Smithsonian Tables. The difference is not significant for these reductions. By substituting 850 mb as p_2 and surface pressure as p_1, the formula gives Φ at 850 mb provided geopotential height at the station is known.

In deriving data at the 850 mb level from elevated surface data, the problem of determining T_{mv} is again a basic one which must be addressed. Since p_2 and p_1 are closer together than in the case of reduction to sea level, errors introduced by making assumptions about T_{mv} have much less impact

in this case. The approach used for this study is relatively simple. The current surface temperature is used, instead of the 12 hour average. The assumed lapse rate is one half the dry adiabatic value. This value is a compromise between the dry adiabatic lapse rate and isothermal conditions, the two diurnal extremes characteristic of the boundary layer in springtime. Spring data were used in this study. The humidity correction applied to obtain the mean virtual temperature from the mean temperature is that recommended by the World Meteorological Organization (1964, p. 25), a suitable constant (.12°C/mb) determined by elevation of the station is multiplied by the surface vapor pressure. Vapor pressure is calculated from the surface dewpoint using Teten's formula (Saucier, 1955, p. 9):

$$e = 6.11 \text{ mb} \times 10^{aT_d/(T_d + b)}$$

where a = 7.5 and b = 237.3° for vapor pressure over water, and T_d is the dewpoint in °C.

Use of the current surface temperature alone in calculating T_{mv} causes problems. The oscillation of the mean temperature of the surface to 850 mb air column does not have as large an amplitude as that of surface temperature. This effect is illustrated schematically in Figure V.2. The solid lines represent the vertical temperature profile for early morning and afternoon. The dashed slanting line is a dry adiabat taken from an emagram. Diurnal heating produces slightly super-adiabatic conditions during the afternoon below 850 mb. Radiative cooling during the night usually produces inversion conditions near the surface. The difference between the oscillation of surface temperature and mean virtual temperature of the column is illustrated by the two sets of vertical lines. The surface temperature is seen to undergo a greater diurnal variation. In the afternoon, use of the surface temperature and one half the dry adiabatic lapse rate would make T_{mv} too warm; in the morning T_{mv} would be too cold. This difference causes calculated 850 mb heights to be too high in the afternoon when the temperature is hot and the lapse rate is adiabatic or greater. The reverse is true in the morning when inversion conditions are often present.

This was verified by comparing the calculated heights with radiosonde observed heights at a number of stations (see Table V.2). Some correction to the current surface temperature is needed to obtain a more accurate estimate of T_{mv} between the surface and 850 mb. The correction used is a sinusoidal function of time with a 24 hour period. Initially the amplitude of the correction term was set at 2°C. The sine function phase lag is 4 hours relative to International or Greenwich Meridian time. The correction has no effect at 04 GMT and 16 GMT, and a maximum additive (subtractive) effect at 10 GMT (22 GMT). This correction improved average error and root mean squared error. The bottom two rows indicate the mean and standard deviation for the diurnal sine correction using 2°C amplitude and for no correction, respectively. Based on this a better estimate for the amplitude was determined to be 2.9°C.

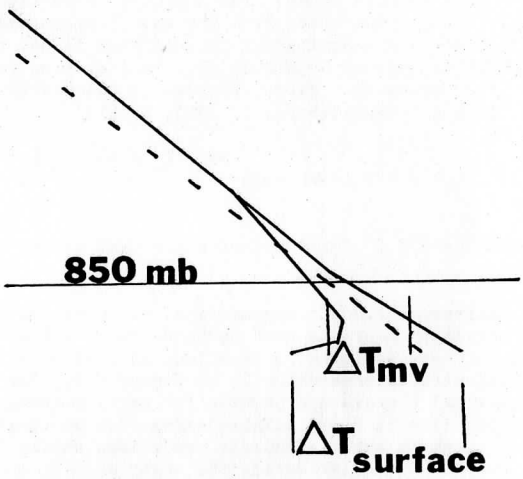

Figure V.2. Typical diurnal variation of surface temperature and surface-850 mb mean virtual temperature. Dashed line represents dry adiabatic lapse rate. Station elevation is 2868 ft (874 m).

STATION	HEIGHT	# OF CASES	00GMT AVG. DIFF. (m)	STAND. DEV. (m)	# OF CASES	12GMT AVG. DIFF. (m)	STAND. DEV. (m)
DODGE CITY, KANSAS	790m	12	.8	2.9	7	1.7	4.6
MIDLAND, TEXAS	872m	11	.4	2.2	8	- .8	6.7
AMARILLO, TEXAS	1098m	12	3.5	2.0	9	8.0	2.6
RAPID CITY, S.DAKOTA	965m	12	-1.9	1.9	9	-2.0	6.0
NORTH PLATTE,NEBRASKA	850m	11	- .1	4.3	9	1.1	5.3
BOISE, IDAHO	874m	12	3.1	2.7	8	.5	7.5
SPOKANE, WASHINGTON	721m	11	1.9	3.5	8	4.3	5.8
GREAT FALLS, MONTANA	1115m	11	.2	3.5	9	- .8	3.1
SALT LAKE CITY, UTAH	1288m	12	.4	1.8	8	- .1	1.6
WINNEMUCCA, NEVADA	1315m	12	1.3	4.5	9	1.8	2.0
YUCCA FLATS, NEVADA	1197m	11	-4.0	2.5	9	-6.4	3.7
TUCSON, ARIZONA	779m	11	1.4	3.3	9	2.9	8.7
EL PASO, TEXAS	1194m	12	- .7	2.5	9	2.4	3.4
OVERALL, diurnal correction amplitude 2.9°C		150	.5	3.0	111	1.0	4.8
OVERALL, diurnal correction amplitude 2.0°C		129	1.7	3.9	109	-1.0	7.1
OVERALL, no diurnal correction		164	3.3	5.3	123	-5.2	9.3

Table V.2. Difference of estimated 850 mb heights using station data and radiosonde observed 850 mb heights (estimated - observed). Period used was 25 March to 18 April 1977. Data was not available for all days.

This further improved the results; the final forms are shown in Table V.2. The data used were for March and April 1977. The mean and standard deviation are for the calculated 850 mb height minus the radiosonde observed height. Overall, it appeared that the diurnal correction of 2.9°C was optimum. It should be noted that the results at 12 GMT were more variable, as evidenced by the higher standard deviation. Also significant are the systematic errors at several stations. For example, Amarillo, Texas has consistently high estimates, especially in the morning. Closer analysis showed that the lapse rate there was usually greater than that assumed. Thus the estimated T_{mv} was higher than the actual T_{mv}, resulting in higher estimated heights. Comparison of average lapse rates for several previous years at Amarillo showed that this year (1977) was anomalous during the period studied.

Another case is Yucca Flats, Nevada. The observed lapse rate indicated frequent inversion conditions in the lowest layers. Even afternoon soundings were relatively stable compared to the other stations used in the study. Estimated T_{mv} is seen to have been lower than observed T_{mv}, resulting in lower estimated heights. Comparison with previous years showed that this is normal for Yucca Flats.

While the assumptions used in determining T_{mv} are somewhat crude, the results are reasonably good. Potential improvements to this method will be discussed in Section VI.

With these four ingredients (T_s, humidity correction, assumed lapse rate, and the diurnal correction) the formula for 850 mb geopotential becomes similar to that recommended in World Meteorological Organization Technical Note #61 (1964, p. 25):

$$\Phi_{850} = \Phi_s - \frac{\log_{10}(\frac{850}{p_s})(T_s + ec)}{(K-(a/2)\log_{10}(\frac{850}{p_s})} \qquad (5)$$

where Φ is geopotential height above sea level in m; p_s is surface station pressure in mb; T_s is given by:

$$T_s = T \text{ (current surface temperature °C)} - 2.9°C \sin [\frac{2\pi}{24}(t-16)],$$

t is time in hours (GMT); e is vapor pressure at the surface; c is a constant, .12°C/mb; K is the hypsometric constant, .0148275 °C/meter; and a is the assumed mean lapse rate, 5°C/km. The diurnal correction is not applied if the windspeed is greater than 14 knots between 04 GMT and 16 GMT. In this case the lapse rate is usually more than one-half the adiabatic value and adding the correction would make T_{mv} too warm.

The data for computing 850 heights are obtained from surface aviation observations transmitted on Service A teletype circuits. Station pressure is recovered from the altimeter setting by reversing the procedure used to calculate the altimeter setting. The formula may be found in the Smithsonian Meteorological Tables (List, 1968, p. 269). Rearranging and solving for station pressure p_s

$$p_s = (A^n - \frac{(p_o^n a)}{T_o} H)^{1/n}$$

A = altimeter setting (inches of mercury), p_o = standard sea level pressure (29.921 inches mercury), T_o = standard sea level temperature (288.15°K), a = lapse rate of standard atmosphere (.0065°K/meter), H = station elevation in meters (elevation for which station pressure is given), n = constant $= \frac{aR}{g} = .1902632$. The values for the constants are from Manual of Barometry (Harrison, 1963, p. 8-68).

One difference from the Smithsonian equation is that .01 inch is no longer subtracted from the station pressure before computing the altimeter setting. Apparently most aircraft altimeters in the early days of aviation were about 9 feet off the ground. By subtracting .01 inch the aircraft altimeter would read the height of the runway when sitting on the ground instead of the runway height plus 9 feet. Altimeters in current aircraft are at widely varying heights above the ground so this practice was discontinued.

Thus far in this chapter only the equations necessary to compute the 850 mb height have been presented. A prime factor in the demise of the previous 850 mb chart was that the data and chart were manually produced requiring considerable time. The 850 mb chart in this study is automated, requiring little or no human time for calculating and plotting of data. The data are decoded and filed by the Man-computer-Interactive Data Access System (McIDAS) at the University of Wisconsin-Madison. At present the decoding program will not accept reports from Automatic Meteorological Observing Stations (AMOS). Not all of the stations decoded were available to the map plotting program. In particular most military stations were not available. Only those military stations located in data sparse areas were included. Mexican stations are received on teletype but were not decoded on the McIDAS system at the time of this work (Spring 1977).

Figure V.3 is a computer printout of the map background and the stations available for use. The three character alphanumeric station identification is that used on the airways observation circuit. The contours represent approximate height above sea level. Two contours are shown, 750 m and 2100 m. The average height of the 850 mb surface is approximately 1460 meters in the standard atmosphere, relatively close to the average station height of 1330 meters.

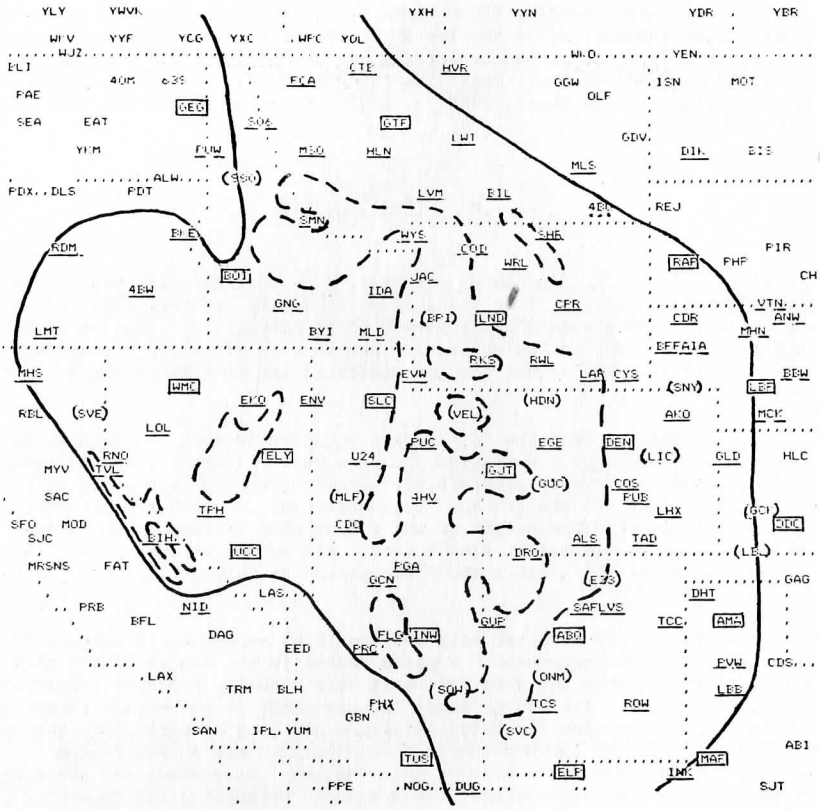

Figure V.3. Map background with available stations. Boxed stations report hourly surface observations 24 hours/day and take two radiosonde observations per day as well. Underlined stations take hourly surface observations 24 hours/day. Dashed underline stations take less than 24 but 12 or more surface observations per day. Remaining stations in parentheses report fewer than 12 surface observations per day. The solid line is the 750 m height contour. The dashed line is the 2100 m contour.

The boxed stations in Figure V.3 are raob sites. The underlining below the station indicates the number of daily scheduled surface observations (see figure legend). Within the area enclosed by the 750 m contour there were originally 108 stations available, of which 70 (65%) reported each hour. A subsequent revision eliminated stations higher than 2060 meters since it was felt that the reduction distance beyond this was too great and would result in substantial errors. Other stations previously unavailable to the computer plotting program were added, bringing the total to 111. Of these 77 (69%) report hourly. Most of the remaining stations report at least 12 times daily.

The remainder of this chapter discusses errors in derived 850 mb heights and temperatures. The original pressure information comes from the altimeter setting which is reported to the nearest one-hundredth of an inch. Assuming this is accurate to $\pm$.005 inch mercury, the absolute limit of accuracy for 850 height computations is about 1.5 meters. Allowing for slight instrument errors and reading errors the practical limit of accuracy in 850 heights obtained from surface pressure observations is 2-3 meters.

As discussed earlier, additional larger errors are introduced when the assumed mean virtual temperature differs from the actual value. This can occur when the actual lapse rate differs greatly from half the adiabatic. The lapse rate in the boundary layer undergoes considerable diurnal variation. This is somewhat accounted for by the correction previously mentioned. The assumed lapse rate is one-half the dry adiabatic value. Figure V.4 shows errors as a function of true lapse rate for various station heights. The effect of the temperature correction at its maximum value is shown as the dashed line. If the true lapse rate were half the adiabatic and no correction were applied then there would be zero difference (0 on the ordinate) between the estimated and actual 850 mb heights. If the true lapse rate were zero (isothermal profile) and no correction were applied, then estimated 850 mb heights would be about 7 m lower than the true 850 mb height for a station at 700 m above sea level. At its maximum positive value the correction effectively compensates for an inversion of 5°C/km when the 850 mb surface is 550 m above the station elevation (about 1000 m). An inversion of 10°C/km is compensated for by the diurnal correction at its maximum positive value when the station is 380 m below the 850 mb surface (about 1180 m).

The diurnal correction cannot account for large departures from the assumed lapse rate, e.g. a very strong inversion. A case in point is 12 GMT on 23 March 1977. At Dodge City, Kansas the temperature at the surface was 1°C while at 170 m above ground it was 11°C. The derived 850 height was 22 m lower than the correct value given by the raob. Fortunately such an inversion often (but not always) affects neighboring stations as well so the error in the height gradient is not so extreme. For this same case the calculated height at Scottsbluff, Nebraska was 21 m lower than the raob (radiosonde observed) height, while Rapid City, South Dakota was 16 m lower. Since the gradient is used in most diagnostic fields, and since it depends upon differences (5 m in this example) this type of error has a diminished effect.

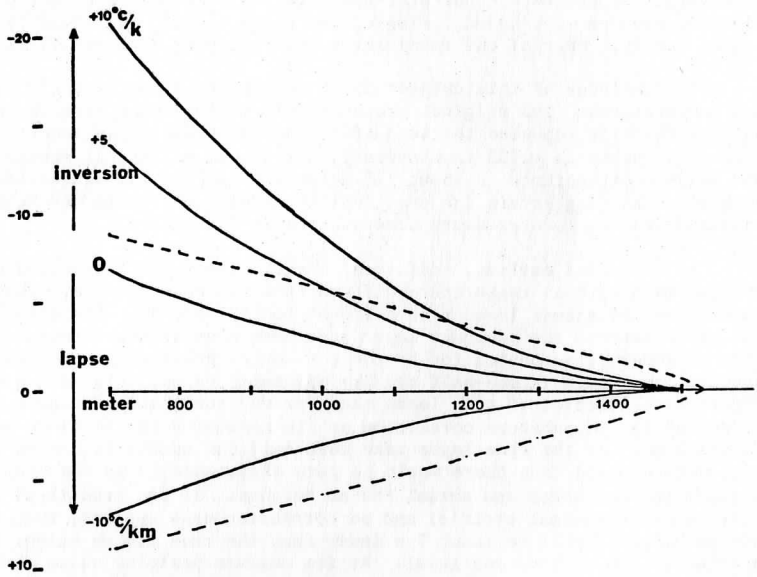

Figure V.4. Maximum likely height errors for various vertical temperature gradients as a function of station elevation. Ordinate gives difference (estimated-actual) in height for various temperature gradients (curves) compared to assumed lapse rate of 5°C/km. Abscissa is station height in meters. Dashed line gives maximum effect of diurnal correction term. Assumed altimeter setting is 30.30 inches Hg, assumed surface temperature is 0°C.

Before diagnostic fields are computed the data are interpolated to one degree-spaced latitude and longitude grid points. The analysis scheme is of the Cressman (1959, p. 369) type with a variable influence radius.

$$Z \text{ grid} = \frac{\sum_{i=1}^{7} W_i Z_i}{\sum_{i=1}^{7} W_i}, \qquad W_i = \frac{N^2 - d_i^2}{N^2 + d_i^2}.$$

For each grid point the radius N is the distance midway between the seventh and eighth closest stations. The distance between the grid point and station i is d_i. The nearest seven stations are used in the scheme. Thus unrepresentative localized effects are smoothed out somewhat. After the analysis a five point two dimensional filter is passed over the data:

$$V = (1.5V_{i,j} + V_{i-1,j} + V_{i+1,j} + V_{i,j-1} + V_{i,\,j+1})1/5.5.$$

The divergence, vorticity, and deformation fields receive an additional pass of this filter after they are computed.

Occasionally the data in the surface observation will be incorrect. Errors in the altimeter setting have the most pronounced effect. Large errors are detected by an error checking program. During the interpolation procedure the average of 5 of the 7 stations is calculated. The highest and lowest values are not included in the average. If any of the seven heights differs by more than 99 meters from the average it is not used in computing the grid point value. Smaller errors will not be thrown out. For example, the altimeter setting may be reported as 30.80 inches instead of 29.80 inches. The height calculated from this value would be thrown out. If it were reported as 30.20 inches instead of 30.02 inches, it would not be thrown out. Errors of this type will be evident on the geostrophic relative vorticity chart, since it is a measure of the Laplacian of geopotential. The sudden appearance of a strong vorticity extremum which greatly exceeds the coriolis value is usually caused by local errors in the altimeter setting. The error can be verified by checking altimeter setting reports at preceding observation times. The data editing feature on MCIDAS permits rapid correction of such errors.

An additional control of the data may be accomplished by examining 850 mb potential temperature charts. Potential temperature at 850 mb is calculated using Poisson's equation

$$\theta_{850} = T_{850}\left(\frac{1000}{850}\right)^{R/C_p}.$$

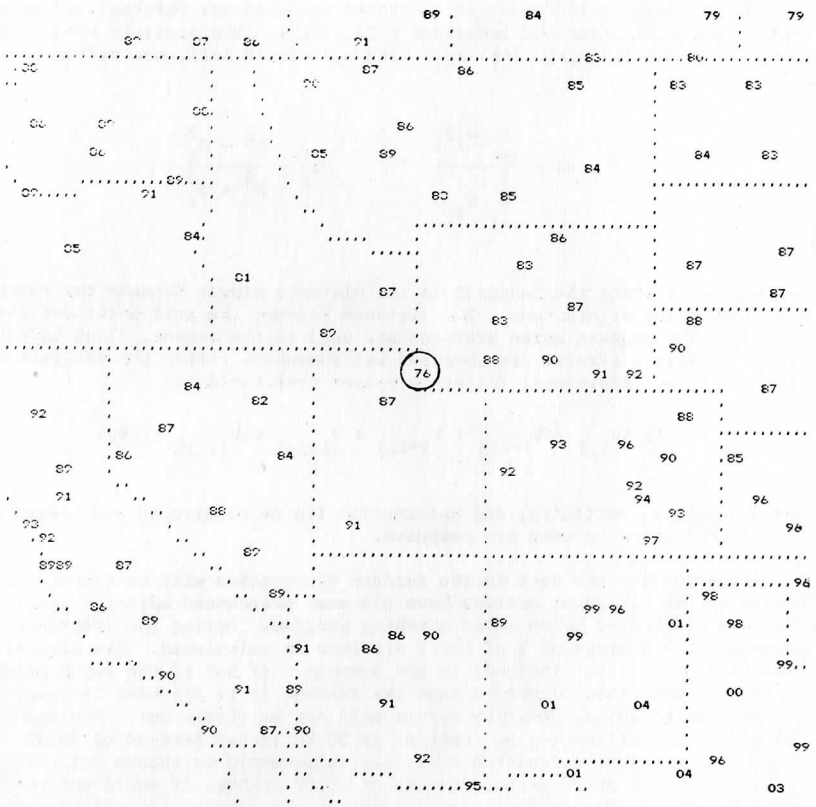

Figure V.5. Derived 850 mb potential temperature for 09 GMT 26 March 1977. If value is less than 50 add 300, otherwise add 200 to get °K. The circled value is for Evanston, Wyoming.

Temperature T_{850} is the station temperature plus the diurnal correction reduced to the 850 mb level using half the dry adiabatic lapse rate. Unrepresentative surface temperatures will appear as isolated maximum or minimum values. Figure V.5 illustrates such an example. Strong radiational cooling occurred at Evanston, Wyoming (southwest corner) following a snowfall earlier in the day 25 March 1977. By 09 GMT on the 26th the surface temperature had fallen to -15°C, much colder than any of the surrounding stations. This is clearly shown as a minimum of 276°K at Evanston on the 850 mb potential temperature chart despite the addition of the diurnal correction. This caused the 850 mb height to be about 20 m higher than it would have been if a more representative temperature had been used.

Most of the errors discussed previously involved the calculated 850 mb height and the raob determined height. The nominal times were at 12 GMT and 00 GMT. However, in reality the data are not observed at the nominal time. The information relayed on the surface observations is actually observed within 15 minutes preceding the hour. The raob on the other hand has an official release time at 2330 GMT and 1130 GMT, but it may be released up to one half hour before or one hour after this time. In practice the release usually occurs 20-30 minutes before the official release time. At stations where these comparisons were made, the 850 mb height is reached in 4 minutes or less. Thus the 850 mb height reported from raobs is usually reached about 40-50 minutes before the pressure is read for the surface observation. The raob time is thus actually closer to 11 GMT and 23 GMT. The final set of statistics in Table V.2 for amplitude of 2.9° used these hours for comparison. Frequently the raob height was intermediate between the 11 GMT and 12 GMT or 23 GMT and 00 GMT calculated heights. This suggests that the errors should be less than indicated in Table V.2. One further complication arises when the station pressure is within 0.5 mb of 850 mb. The raob height reported is then the station height, even though it may be incorrect by up to 5 meters.

IV. DIAGNOSTIC WIND FIELDS ON THE DERIVED 850 MB SURFACE

A distinct advantage of the constant pressure chart is that many diagnostic fields can be quickly and easily produced. A variety of winds can be computed and used to calculate advections or differentiated to give vorticity, divergence, and deformation. The formulas and some discussion of these fields are given in this section and examples of them are discussed in Section V. Because the 850 mb height is available each hour, time differencing and averaging are easily accomplished; this provides tremendous flexibility.

The geostrophic wind and two ageostrophic wind estimates are computed from the 850 mb height field. They are frictionless synoptic-scale winds. The formula for the geostrophic wind is

$$\vec{V}_g = \frac{1}{f} \vec{k} \times \nabla \Phi .$$

The two horizontal wind components at a grid point are computed using centered differencing on a one degree grid. Thus the effective interval for computing winds is two degrees of latitude or longitude, a distance comparable to the typical spacing between surface stations.

In addition to the geostrophic wind two ageostrophic wind estimates are computed. These estimates are based on frictionless quasi-geostrophic theory. The first may be termed an inertial type correction $\vec{V}_{in}$. It results from balancing the coriolis force associated with the ageostrophic $\vec{V}_{in}$ with the inertial acceleration estimated using the geostrophic wind field. Since accelerations are most significant on a smaller scale we may take f as locally constant. The equation used is

$$\vec{V}_{in} = \frac{1}{f} \vec{k} \times [(\vec{V}_g \cdot \nabla)\vec{V}_g] .$$

The second ageostrophic wind component is the isallobaric wind:

$$\vec{V}_{is} = - \frac{1}{f^2} \nabla \frac{\partial \Phi}{\partial t} .$$

It is significant when a pressure system moves rapidly, is deepening, or weakening. The time scale for $\frac{\partial \Phi}{\partial t}$ should be on the order of f^{-1} (3 hours at midlatitudes) or longer. The isallobaric wind uses the field of difference in 850 mb heights between two specified hours. To be consistent for comparison, the other two winds ($\vec{V}_g$, $\vec{V}_{in}$, and their derivatives) may also be computed from time-averaged height fields over the same time interval. Time averaging is also useful for interpolating missing data from surrounding hours. Figure 6 compares the derived 850 mb height field for 26 March 1977 at 15 GMT with a time-averaged field (dashed lines) based upon data at 13 GMT and 17 GMT. The general patterns are very similar with the greatest differences in areas of weak gradients.

Relative vorticity (ζ) is calculated from the wind. The vertical component of vorticity is found from the horizontal wind (u,v) components via:

$$\zeta = \frac{\partial v}{\partial x} - \frac{\partial u}{\partial y} .$$

Vorticity at a grid point is determined by taking centered differences of the wind components. Vorticity may be calculated from either the geostrophic wind (ζ_g) or the inertial correction type wind $\vec{V}_{in}$; the allobaric component V_{is} is irrotational when small variations in f are ignored.

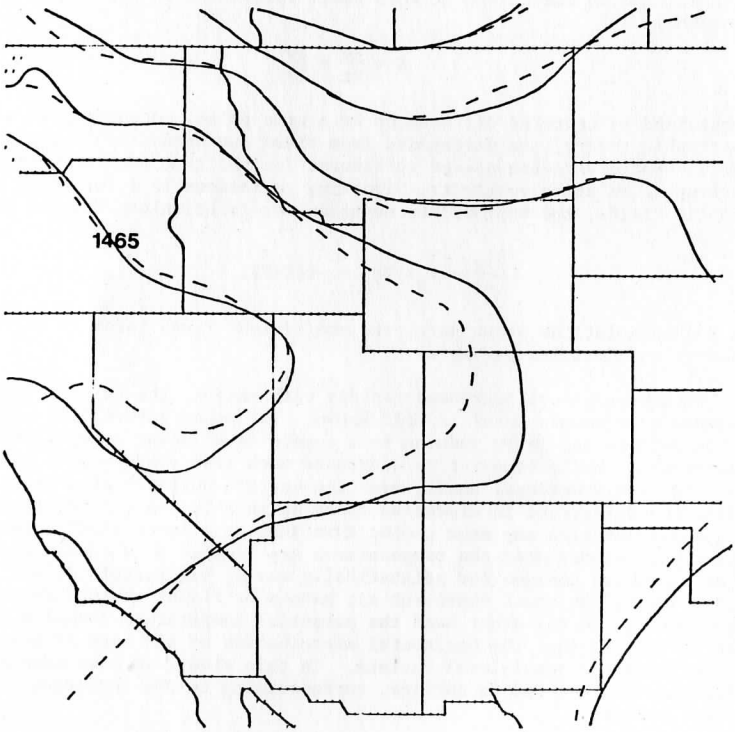

Figure V.6. Derived 850 mb height fields for 15 GMT 26 March 1977. The solid lines are the instantaneous 15 GMT contours while the dashed lines are time averages based upon 13 GMT and 17 GMT data. Contour interval is 30 meters.

Divergences can be computed for the two ageostrophic winds; the geostrophic wind is non-divergent when small variations in f are ignored. The divergence

$$\delta = \frac{\partial u}{\partial x} + \frac{\partial v}{\partial y}$$

is obtained by centered differences at a grid point. According to quasi-geostrophic theory, the divergence from these two ageostrophic winds is exactly that divergence needed to account for the time rate of change of geostrophic relative vorticity. Ignoring variations in f for these subsynoptic fields, the appropriate equation for frictionless flow is then:

$$\frac{\partial \zeta_g}{\partial t} + \vec{V}_g \cdot \nabla \zeta_g = -f(\nabla \cdot \vec{V}).$$

For the calculations shown here, the coefficient f was taken to be the local value of the Coriolis parameter.

Because pressure decreases rapidly with height, the need to reduce pressure to a common level is well known. Yet other information observed at the surface should be reduced to a common level also; a key variable is temperature. While temperature decreases much less rapidly with height than pressure on a fractional basis, over the western United States there is sufficient difference in elevation to be noticeable. A surface temperature at a higher station may seem cooler than that at a lower station but actually be warmer when the temperatures are reduced to a common level. Since elevation changes for adiabatically moving air parcels do not result in θ changes, one could represent air masses by fields of surface potential temperature. On the other hand the potential temperature normally increases with height, so that the horizontal distribution of air mass is best viewed by considering a quasi-level surface. In this study, we have chosen to represent θ on the 850 mb surface, corresponding to the temperature field on that surface.

The horizontal advection of θ (850 mb) by any of the three winds can be calculated. The wind components at the central grid point multiply the gradient determined by centered differencing of θ values.

Shearing and stretching deformation can also be computed. Stretching deformation is given by

$$\frac{\partial u}{\partial x} - \frac{\partial v}{\partial y} .$$

Shearing deformation is computed using

$$\frac{\partial u}{\partial y} + \frac{\partial v}{\partial x} .$$

Both terms are generally nonzero for both geostrophic and ageostrophic components. They are calculated by finite differences in a manner similar to vorticity and divergence. The optimum form for use of these "components" is to use them to calculate fields of (a) deformation magnitude and (b) angular orientation of local dilitation axis.

Thus far we have considered only frictionless winds. Recalling that the average station elevation (for this sample) in the western plateau is 1330 m and the 850 mb height in the standard atmosphere is 1460 m, we should expect that the 850 mb surface will be in the frictional boundary layer near most stations. The actual winds at 850 mb will thus differ markedly from the geostrophic winds at 850 mb.

Assuming that (1) the wind is approximately geostrophic above the boundary layer, (2) the geostrophic wind is constant through the boundary layer, and (3) the boundary layer wind is balanced, an Ekman spiral solution can be obtained. Choosing typical values of 5 m^2/sec for eddy diffusivity, the top of the surface layer at 40 m, and the height of the 850 mb surface 90 m higher, one may calculate an ageostrophic wind about 3/4 the magnitude of the geostrophic wind at 850 mb when no-slip conditions at the surface layer too are imposed. Taking a more general approach (Young, 1973) which allows for some slip ($\hat{\delta}$ = .13-.50) gives an ageostrophic magnitude of 1/2 to 2/3 the geostrophic magnitude. This is somewhat larger than typical frictionless inertial corrections (1/4-1/2) or isallobaric corrections (1/8-1/4) found in examples to be presented later.

The addition of frictional effects to the geostrophic wind produces a divergence pattern proportional to the geostrophic vorticity pattern. This is referred to as Ekman pumping. For the 850 mb surface the divergence is about 1/5 the geostrophic vorticity on the average as estimated from information presented by Young (1973, p. 1587 see Table V.1 or Equation (3.2)).

The effect of friction on the ageostrophic winds calculated from frictionless theory can also be estimated. Young (1973) treats the isallobaric frictional case showing a reduction in the divergence predicted by the frictionless isallobaric wind. Mahrt (1975) treats frictional influences on the inertial accelerations which cause a reduction in Ekman pumping effects.

V. CASE STUDY EXAMPLES USING THE DERIVED 850 MB FIELDS

As noted earlier, the derived 850 mb chart is much more representative of surface fields over elevated regions in the western United States than the sea-level pressure chart. A brief discussion of the errors in the sea-level pressure gradient is presented along with case studies showing these errors. The derived 850 mb height field is also compared to the NMC 850 mb chart and is shown to have greater spatial resolution. Examples of the various parameters discussed in Section IV are presented; as well as time sequences of them.

The 5000 foot chart introduced in the early 1930's was an attempt to supplement the reduced sea-level map with one that was more representative of surface conditions over the plateau region of the western United States. Aviation forecasters recognized that the sea-level pressure map did not correlate well with surface winds and that spurious lows and highs were sometimes present. Harrison (1957, p. 49) has shown that, even over level terrain, reduction of surface pressure to sea level introduces an error in the sea-level pressure gradient whenever there is a gradient in the mean temperature field used for reduction. Since sea-level pressure ($P_o(x,y)$) is a function ($F(p_s, T_{mv}, Z_s)$) of station pressure (p_s), mean virtual temperature (T_{mv}), and geopotential height of the station (Z_s) then the horizontal gradient of sea-level pressure may be expressed as

$$\nabla_h p_o = \frac{\partial F}{\partial p_s} \nabla_h p_s + \frac{\partial F}{\partial Z_s} \nabla_h Z_s + \frac{\partial F}{\partial T_{mv}} \nabla_h T_{mv} \ .$$

(1) (2) (3)

Thus in general the reduced sea-level pressure gradient is a function of the station pressure gradient (term 1), the slope of the terrain (term 2), and the gradient of mean virtual temperatures (term 3). Assuming for the moment that the terrain is level (term 2=0), there still remain two terms in the equation for the sea-level pressure gradient. Since we have assumed level terrain the first term is the surface pressure gradient. This is the physical force that must be represented in order to study surface winds. The remaining term is the gradient of mean virtual temperature used for reduction. If it is nonzero then a vector error is introduced in the sea-level pressure gradient. This error is also a function of column thickness and hence station height through the $\frac{\partial F}{\partial T_{mv}}$ term. Stations at high elevations such as found on the plateau region of the western United States may have a significant error, especially when extreme surface baroclinity exists, as in the winter season.

One example is given by the case of 14 April 1977 at 18 GMT. A surface cold front moving eastward existed between Salt Lake City and Grand Junction. The difference between surface temperatures was 17°C. By averaging over 12 hours and adjusting to the level (1381 m) midway between station elevations via the adiabatic lapse rate the horizontal difference was about 9.4°C. Assuming this same temperature difference existed for T_{mv}, the average gradient of T_{mv} was 2.5°C/100 km. At the average height between these stations this corresponded to a 4.6 mb error in the sea-level pressure, or a gradient of 1.25 mb/100 km. The total difference in sea-level pressure was 12.2 mb. An estimate of the actual horizontal pressure difference obtained by reducing a very short distance to the mean height between stations was 7.9 mb. The derived 850 mb height difference was 70 meters corresponding to a pressure difference of 7.5 mb between Salt Lake and Grand Junction. Since the elevation of the 850 mb surface is about 1460 m, and since the mean level for this reduction was 1381 m, the difference in elevation was

small enough that actual baroclinity would not significantly alter the pressure differences. Thus, the derived 850 mb height difference was nearly identically equivalent to the pressure difference at a mean level while the pressure difference given by the sea-level map had a large error (~50%) caused by the gradient of mean temperature used for reduction. The temperature gradient was only moderate in this example. Much stronger gradients and hence much larger errors could occur.

Another example is 24 March 1977 at 00 GMT. A cold front moving rapidly eastward had crossed northern Nevada. Between Winnemucca, Nevada and Salt Lake City, Utah there was 11.7°C difference in surface temperature. Twelve hour averaging reduced this difference to 7.5°C. Assuming this difference for T_{mv} would result in a 3.4 mb "error" in the reduced sea-level pressure between stations. The difference in sea-level pressure was 6.3 mb. The actual pressure difference reduced slightly to a mean level (1302 m) was 3.3 mb. Using the geostrophic winds from the Sangster chart gave an average equivalent 28 meter height difference along the line between the two stations, corresponding to 3.0 mb in horizontal pressure difference. By comparison the derived 850 mb height difference (time averaged) was 31 meters or 3.3 mb. Thus, the derived 850 mb height differences yielded horizontal differences comparable to those obtained at a mean level or from the Sangster chart.

In this case the 850 mb height difference from the 00 GMT raob was only 14 m or 1.5 mb. This value is smaller than any of the others. The reason for the discrepancy may be the times at which raobs are taken. As mentioned previously, the release time may be an hour before or 29 minutes after the nominal reporting time. This hour and a half window can make a significant difference. In this case the pressure was falling at Salt Lake City and rising at Winnemucca. A difference of one hour changed the height difference between stations by 10 to 30 m. For example the derived 850 mb height difference (Winnemucca minus Salt Lake City) was -8 m at 22 GMT, 20 m at 23 GMT, 31 m at 00 GMT, and 41 m at 01 GMT.

These two examples clearly show that the sea-level pressure map is inadequate for determining the surface-pressure gradient force. They also suggest that the derived 850 mb chart does much better and is usually close to the true surface gradient as estimated from the Sangster sigma coordinate calculations or from reduction to a mean level. This is better seen on Figure V.7. The derived 850 mb contours are drawn for 00 GMT 24 March 1977. Because of data problems and the desire to be consistent with the data base used for the isallobaric winds, the 850 mb heights are time averaged from 22 GMT to 02 GMT. The dashed contours show the 4 hour height change pattern. The 4 hour interval was chosen to minimize effects from possible subsynoptic gravity-wave activity, which often shows periods of 1-4 hours. The solid contours are the time averaged derived 850 mb height contours. Winds from the raobs are plotted also. These winds are at the 850 mb height (1320-1470m) or 1524 m or 1829 m (5 or 6 thousand feet). They are at least 305 meters (1000 feet) above the surface to minimize frictional influence and hence provide an estimate of the surface geostrophic wind.

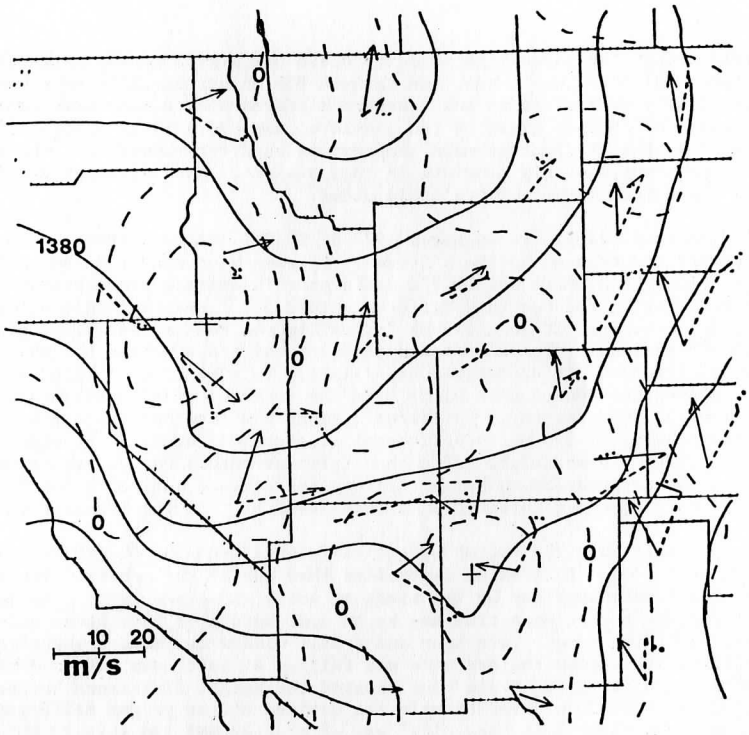

Figure V.7. Derived 850 mb height and wind data for 00 GMT 24 March 1977. Solid lines are derived 850 mb height contours time averaged two hours before and after 00 GMT, at 30 meter contour intervals. Dashed continuous lines are 4 hour height change pattern. Contour interval is 10 meters/4 hours. Arrows are observed winds at 850 mb, 5 or 6 thousand feet (1524 or 1829 meters). Theoretical frictionless wind components from estimated 850 mb fields are geostrophic (dashed line), ageostrophic inertial correction (solid line), and isallobaric (dotted line), plotted in that order. The point of origin is at the beginning of the dashed line.

For comparison the three theoretical wind components calculated from the derived 850 mb height fields are also plotted. The geostrophic wind is the dashed line, the inertial correction is the solid line, and the isallobaric wind is dotted. With the exceptions of local and frictional effects these are usually the three most important wind components.

These three wind components are more easily visualized in the natural coordinate system. Ignoring vertical advection, the frictionless horizontal equations of motion may be written as:

$$\frac{\partial \vec{V}}{\partial t} + (\vec{V}\cdot\nabla)\vec{V} + f\vec{k}\times\vec{V} = -\nabla\Phi$$

or in quasi-geostrophic form (Young, 1977) as

$$\frac{\partial \vec{V}_g}{\partial t} + (\vec{V}_g\cdot\nabla)\vec{V}_g + f\vec{k}\times\vec{V} = -\nabla\Phi = +f\vec{k}\times\vec{V}_g$$

(1) (2) (3) (4)

Complete knowledge of the geopotential field allows terms 1, 2 and 4 to be estimated, and the total wind vector $\vec{V}$ may then be obtained from term 3. Thus the total wind may be thought of as that arising from term 4 (geostrophic wind), term 1 (ageostrophic isallobaric wind), and term 2 (ageostrophic inertial correction).

Term 4 yields the geostrophic wind. It is the only wind component if there is no curvature, spreading of geopotential lines, or time changes of the geopotential field. The geostrophic wind is the dashed vector in Figure V.7, and is everywhere parallel to the geopotential pattern (solid contours).

Term 1 yields the isallobaric wind. It is directed toward relative minima in the height change pattern and away from relative maxima. This is easily seen in the isallobaric wind field (dotted vectors). The time changes in the height pattern are usually largest with fast moving troughs. In this example the largest height change gradient (dashed contours) is along the northern Utah-Nevada border. Here the isallobaric wind component is the dominant one since the 850 mb geopotential gradient is weak. The isallobaric wind is seen to point toward the height change minimum located in central Utah.

Term 2 yields the inertial correction. It's most convenient to portray term 2 in natural coordinates:

term 2a: $V_g \frac{\partial V_g}{\partial S_g}$ along the flow

term 2b: $\frac{V_g^2}{R_g}$ normal to the flow (positive to the left)

Here V_g is the speed of the geostrophic wind ($|\vec{V}_g|$), S_g is distance along the geostrophic streamline (which is identical with the geopotential contour), and R_g is the radius of curvature of the geostrophic streamline (not the trajectory).

The inertial correction is large where the geopotential curvature is strong (term 2b) or where there is a confluent/diffluent geostrophic flow (term 2a). The sharpest curvature is located around the trough and ridge axes. The acceleration vector points towards the low center in cyclonic flow and towards the high center in anticyclonic flow. The ageostrophic component of the inertial correction wind is 90° to the left of the acceleration vector. Thus in cyclonic flow the ageostrophic wind points in the opposite direction of the geostrophic wind making the total wind subgeostrophic. The opposite is true for anticyclonic curvature. The senses of those corrections are identical to those of the gradient wind. For confluence the acceleration vector is in the same direction as the flow, while for diffluence it opposes the flow. A good example of the inertial correction type wind is found near the eastern limit of the Colorado-New Mexico border in Figure V.7, where the inertial correction wind associated with strong cyclonic curvature is nearly as large as the geostrophic wind. Another case is found in southeastern Utah. Here the inertial correction is due mainly to diffluence of the contours associated with deceleration along the flow. Since the ageostrophic inertial correction wind points 90° to the left of the acceleration vector, in this case it is directed to the right of the geostrophic wind, toward higher heights.

The derived 850 mb chart has some advantages over the National Meteorological Center (NMC) 850 mb chart. It is capable of greater spatial resolution. Within the area outlined in Figure V.3, there are 19 raob stations. Four of those must normally extrapolate downward using an assumed atmosphere to reach the 850 mb level. The derived chart uses 111 stations within this same area, or nearly 6 times as many. Of course, not all of these stations will be available each hour, nor are the stations evenly distributed. It is clear that the derived chart can resolve much smaller scale features, down to the subsynoptic scale: 00 GMT 24 March 1977 is an example (Figure V.8), where the derived 850 mb height field is depicted by the solid contours. The NMC analysis (obtained from a facsimile chart) is shown by the dashed contours. There is a trough in Colorado east of the Rockies and another in northwest New Mexico as well. They are well depicted in the derived 850 mb analysis but are not well defined in the NMC 850 mb analysis. The station data for both the derived and NMC charts (not shown) supported the trough in New Mexico. In fact a weak closed low may have existed as Albuquerque's raob wind near the surface was from the east (see Figure V.7).

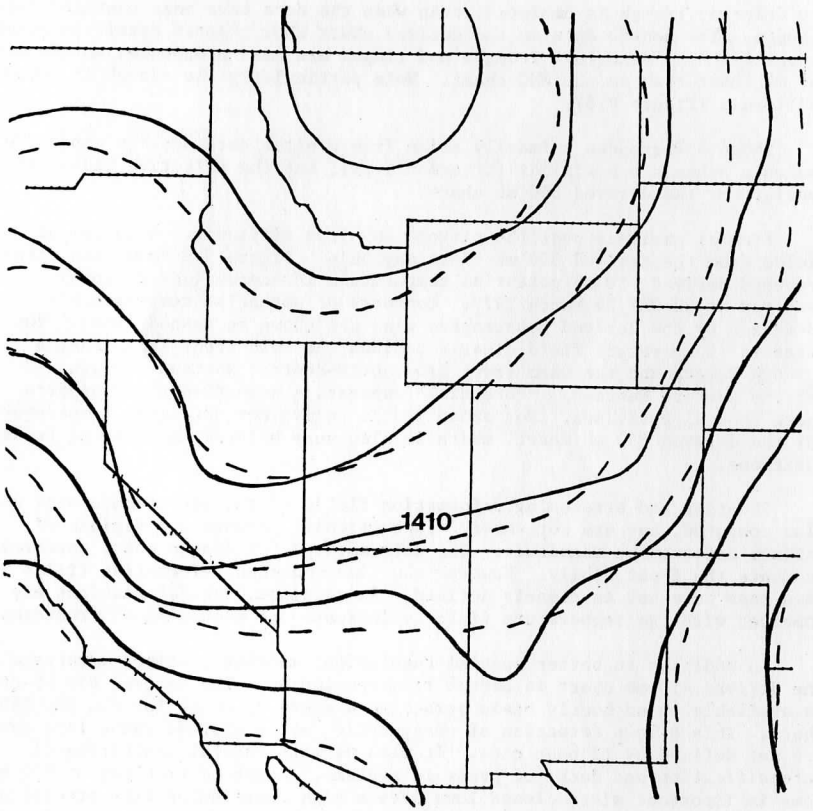

Figure V.8. Comparison of derived 850 mb contours (solid lines) and NMC 850 mb contours from radiosonde stations (dashed lines) for 00 GMT 24 March 1977. Derived 850 mb height is time averaged two hours before and after 00 GMT. Contour interval is 30 meters.

The trough in Colorado was smaller scale and was located between raob stations. Since the data on the derived chart are six times as dense, the Colorado trough is depicted, even when the data have been averaged over 4 hours. The denser data on the derived chart show greater detail in other synoptic-scale features. Troughs and ridges are more pronounced on the derived 850 mb chart than on the NMC chart. Note particularly the trough in Nevada-California (Figure V.8).

These differences primarily arise from greater data density since the analysis schemes are similar (Cressman type), but the effective radius is smaller for the derived 850 mb chart.

Frontal analysis over the plateau is often difficult. A number of fields from the derived 850 mb chart may help. Figure V.9 shows the time-averaged derived 850 mb potential temperature isotherms (solid lines) centered at 00 GMT 24 March 1977. Contours of potential temperature advection by the derived geostrophic wind are shown as dashed lines. The potential temperature field clearly defines the cold front from Montana through Nevada and the warm front from north-central Montana through extreme western Nebraska. Potential temperature advection also supports these frontal positions. Not shown is the equivalent potential temperature for the derived 850 mb chart, which is also very helpful in locating frontal positions.

Shearing and stretching deformation fields of the geostrophic wind were also computed, but are not shown. Theoretically, fronts are regions of maximum deformation magnitude. The deformations for single hours appeared to indicate the front nicely. However the time-smoothed deformation fields in this case were not as clearly defined. In addition, the deformations may be combined with the temperature field to indicate one mechanism of frontogenesis.

In addition to better spatial resolution, another distinct advantage of the derived 850 mb chart is better time resolution. The derived 850 mb chart is available on an hourly basis versus once every 12 hours for the NMC 850 mb chart. This allows detection of subsynoptic scale systems whose life cycles are not defined by 12 hour data. It also permits careful monitoring of intensification and decay of pressure systems. Accurate tracking of 850 mb lows is important since closed lows have a high correlation with precipitation over the plateau region of the western United States (Jorgensen, et al., 1969).

This is illustrated by Figure V.10, which is a time cross section of derived 850 mb heights approximately along a line between Idaho Falls, Idaho and Roswell, New Mexico. Each hour is plotted for the 24 hour period between 16 GMT 14 April 1977 and 15 GMT 15 April 1977. A low in south-central Wyoming initially drifted southward to southwest Colorado with slight intensification, then began to fill after 00 GMT 15 April 1977. The 850 mb height at Durango, Colorado fell to 1359 M at 23 GMT and then slowly increased. High pressure is shown increasing along the cross section from the northwest. Heights at Evanston, Wyoming rose from 1420 m to near 1500 m in 12 hours. The pressure increased so rapidly that a strong pressure gradient was produced across northeastern Utah, with a 98 m height difference between

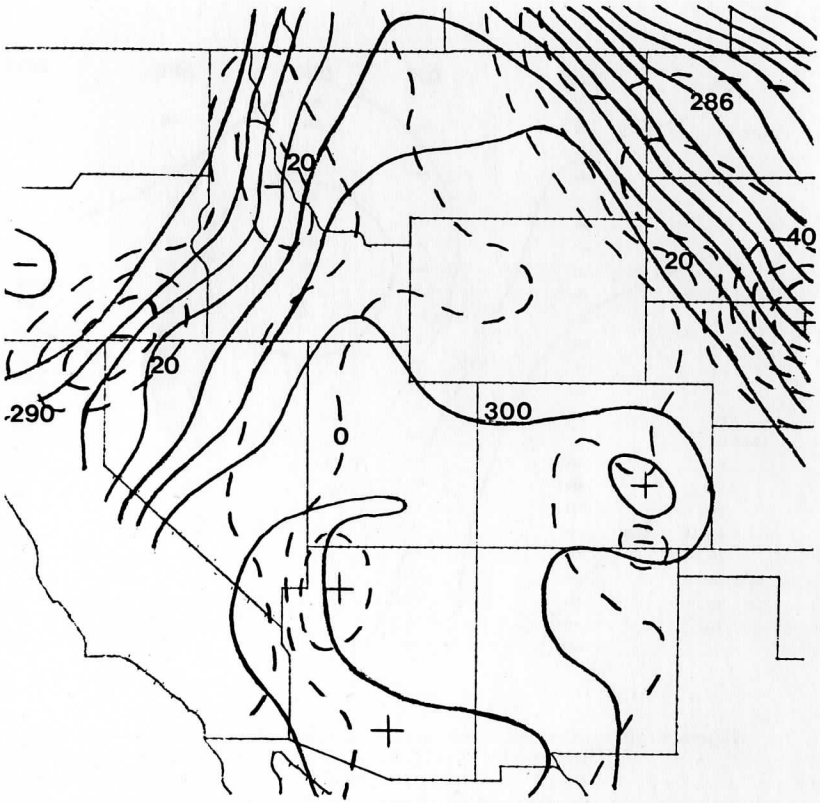

Figure V.9. Derived 850 mb potential temperature (solid lines) and geostrophic potential temperature advection at 850 mb (dashed lines) for 00 GMT 24 March 1977 time averaged two hours before and after 00 GMT. Contour intervals are 2°K and 10°K/day.

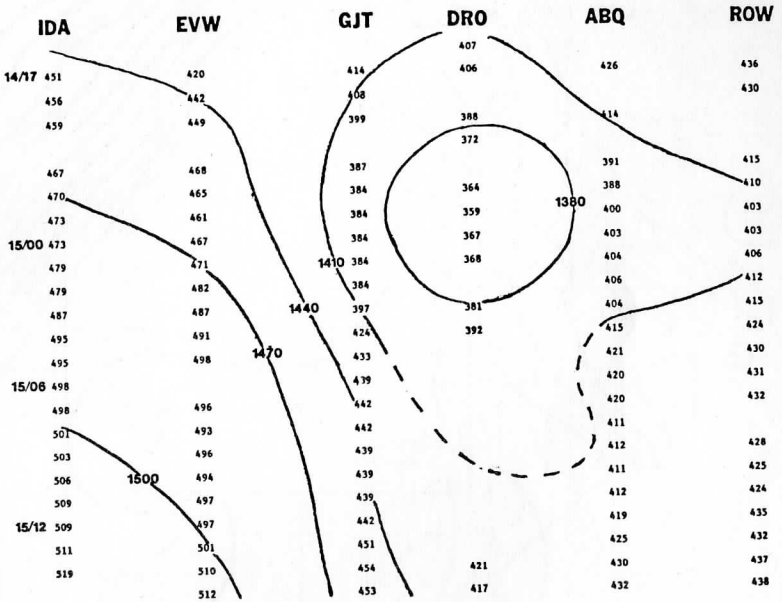

Figure V.10. Distance/time cross section from 16 GMT 14 April to 15 GMT 15 April 1977. Cross section runs from NNW to SSE. Stations are Idaho Falls, Idaho (IDA); Evanston, Wyoming (EVW); Grand Junction (GJT) and Durango (DRO), Colorado; Albuquerque (ABQ) and Roswell (ROW), New Mexico. Derived heights (m) minus 1000 are shown. Contour interval is 30 m.

Evanston, Wyoming and Grand Junction, Colorado at 02 GMT on the 15th.

A 24 hour map sequence at 3 hour intervals is shown in Figures V.11 through V.18. The time period is approximately the same as that used in the time cross section, 18 GMT 14 April 1977 to 15 GMT 15 April 1977. Each figure has three panels: the derived 850 mb height, derived geostrophic relative vorticity at 850 mb, and a theoretical time-averaged 850 mb divergence. The height field shows the low in south-central Wyoming moving to the Colorado-New Mexico area with slight intensification. High pressure was increasing in the Pacific Northwest behind a cold front. The sequence is evident in the vorticity patterns as well as the height field. The vorticity maximum in southwest Wyoming stretched southward and then split, with the northern maximum weakening rapidly. It should be noted that vorticity is the second spatial derivative of pressure and therefore sensitive to even slight pressure perturbations. The potential utility of this fact will be discussed further in the next Section.

The divergence shown in Figures V.11 through V.17 is from the quasi-geostrophic estimates of the isallobaric and the inertial correction type winds. The divergence of the inertial correction type wind is found from the divergence formula mentioned in Section IV. The divergence of the isallobaric wind is obtained from:

$$\delta_{is} = -f^{-2} \nabla^2 \frac{\partial \Phi}{\partial t} .$$

The time interval used for this divergence was 3 hours. For consistency the inertial correction type wind is time-averaged over the same three hour period. The vorticity and geopotential fields in Figures V.11 through V.17 are based on single hour data only.

If frictional effects and the beta effect are ignored in the quasi-geostrophic vorticity equation, the local change of geostrophic vorticity is caused by advection of geostrophic vorticity and divergence:

$$\frac{\partial \zeta_g}{\partial t} = -\vec{V}_g \cdot \nabla \zeta_g - (\nabla \cdot \vec{V})(\zeta_g + f)$$

Here we have included ζ_g in the coefficient multiplying the divergence although strictly speaking it should not be present in a quasi-geostrophic formulation. This has the effect of enhancing the impact of divergence on vorticity changes in cyclonic areas. If the relative geostrophic vorticity term is dropped from the divergence coefficient, it can be shown that the local change of geostrophic vorticity is equal to the divergence of the isallobaric wind; the remaining two terms, the advection of geostrophic relative vorticity by the geostrophic wind the divergence of the inertial

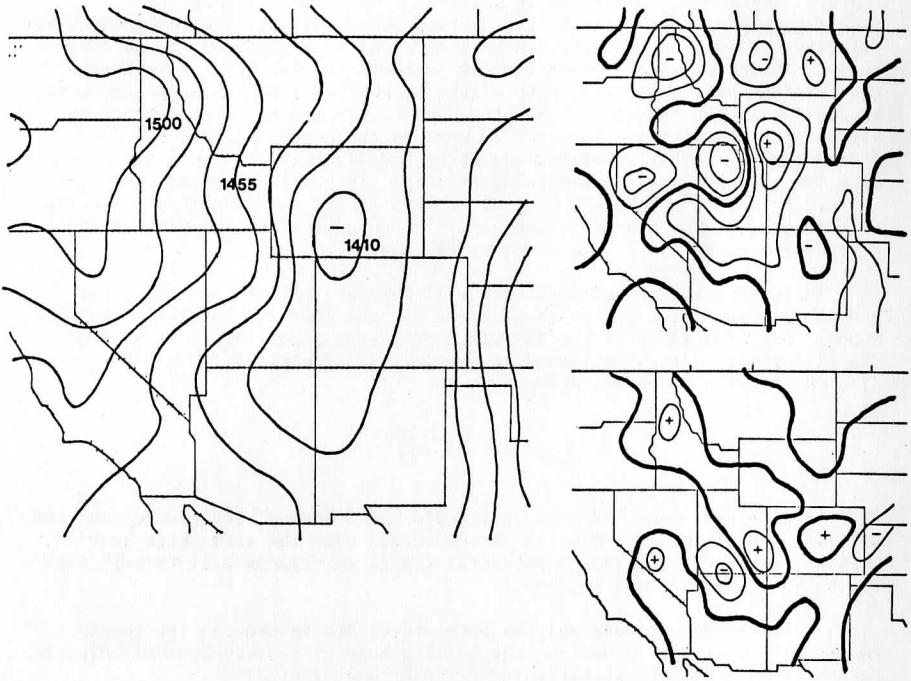

Figure V.11. Derived 850 mb fields for 18 GMT 14 April 1977. Left: derived 850 mb height, contour interval 15 meters. Top right: derived geostrophic relative vorticity for 18 GMT 14 April 1977. Bottom right: quasi-geostrophic divergence for 18-21 GMT 14 April 1977. Heavy lines are zero contours. Contour interval is 4×10^{-5} s^{-1} for vorticity and divergence.

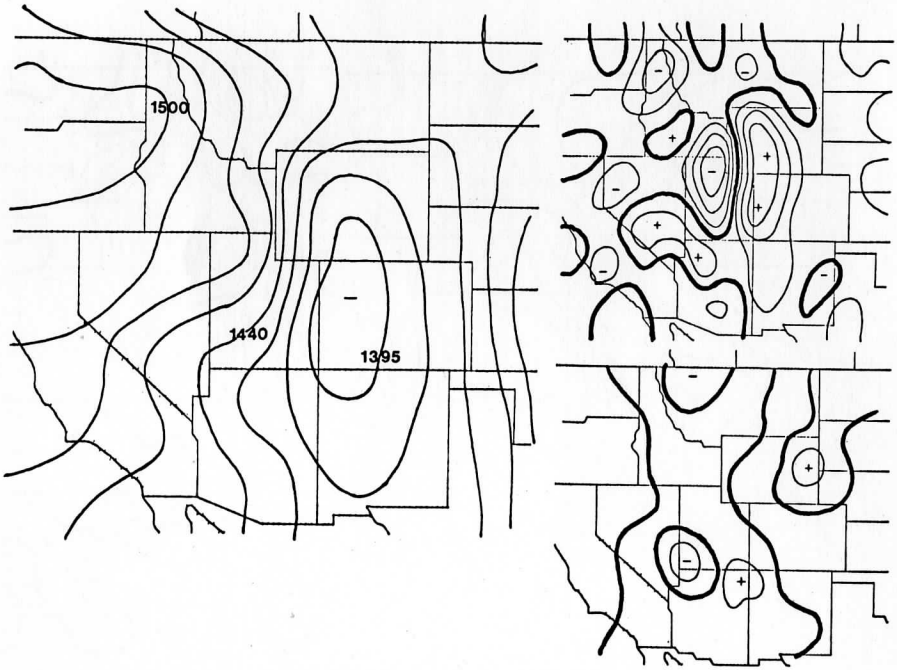

Figure V.12. Same as Figure V.11 for 21 GMT 14 April 1977 and 21 GMT 14 April-00 GMT 15 April 1977.

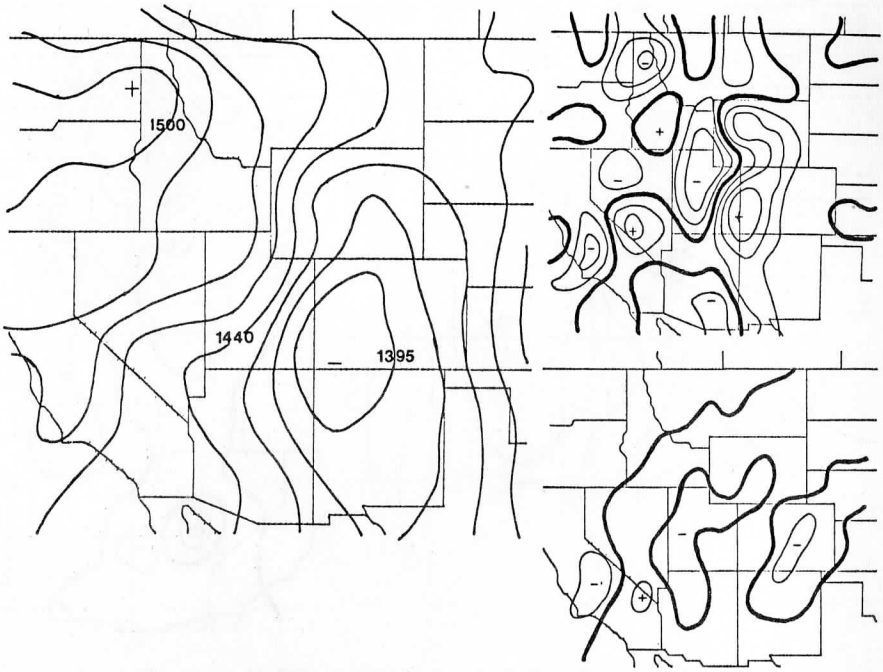

Figure V.13. Same as Figure V.11 for 00 GMT 15 April 1977 and 00-03 GMT 15 April 1977.

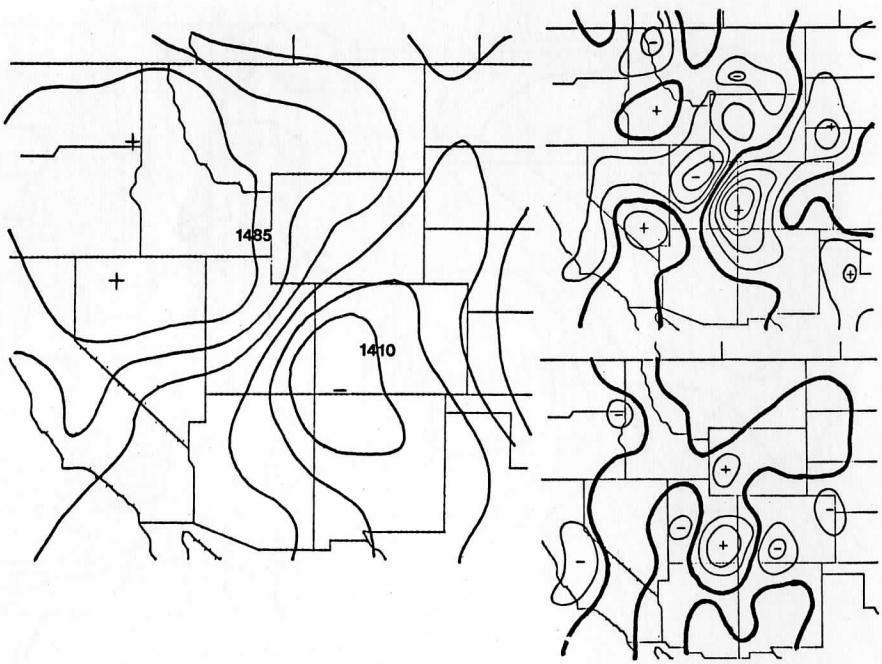

Figure V.14. Same as Figure V.11 for 03 GMT 15 April 1977 and 03-06 GMT 15 April 1977.

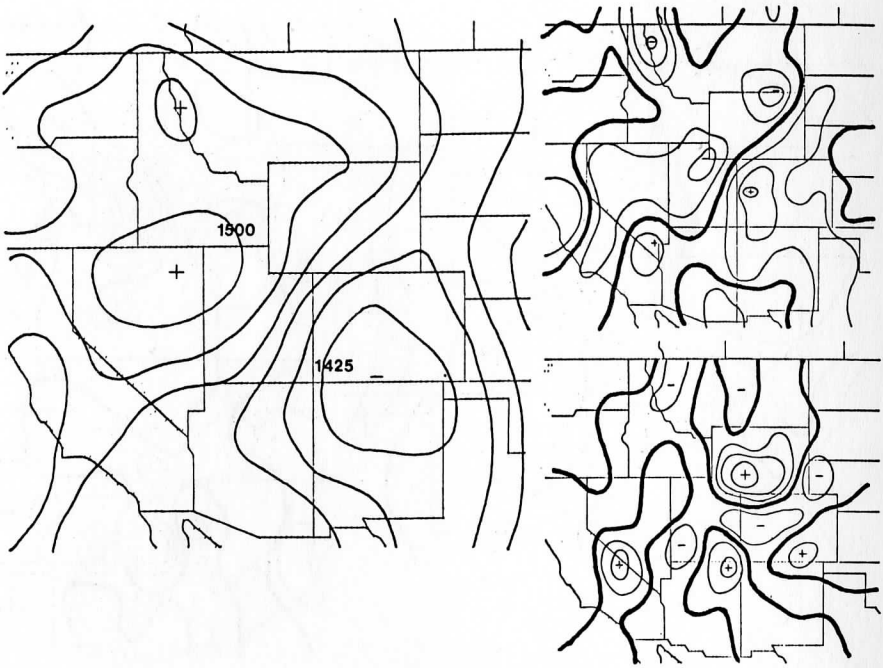

Figure V.15. Same as Figure V.11 for 06 GMT 15 April 1977 and 06-09 GMT 15 April 1977.

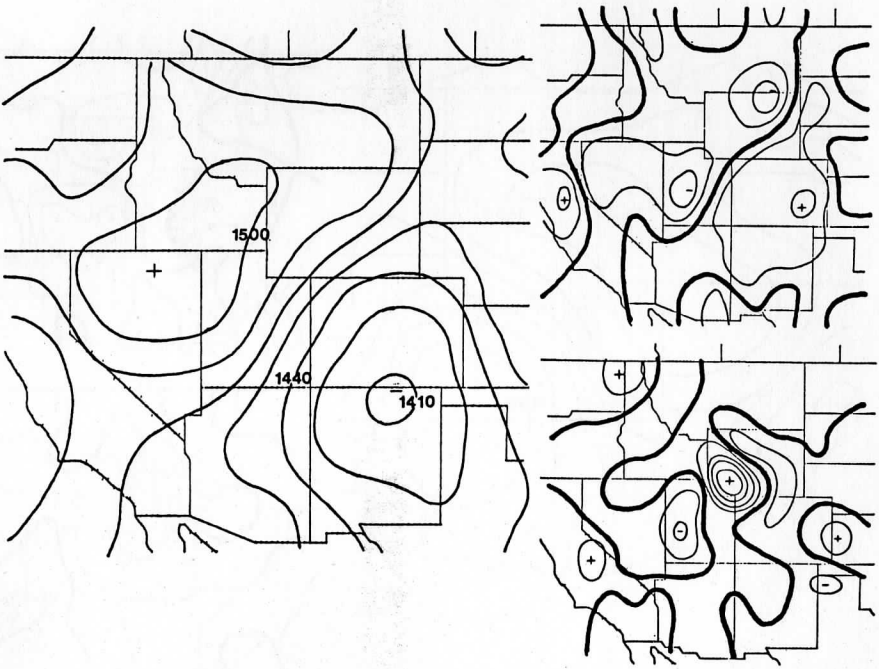

Figure V.16. Same as Figure V.11 for 09 GMT 15 April 1977 and 09-12 GMT 15 April 1977.

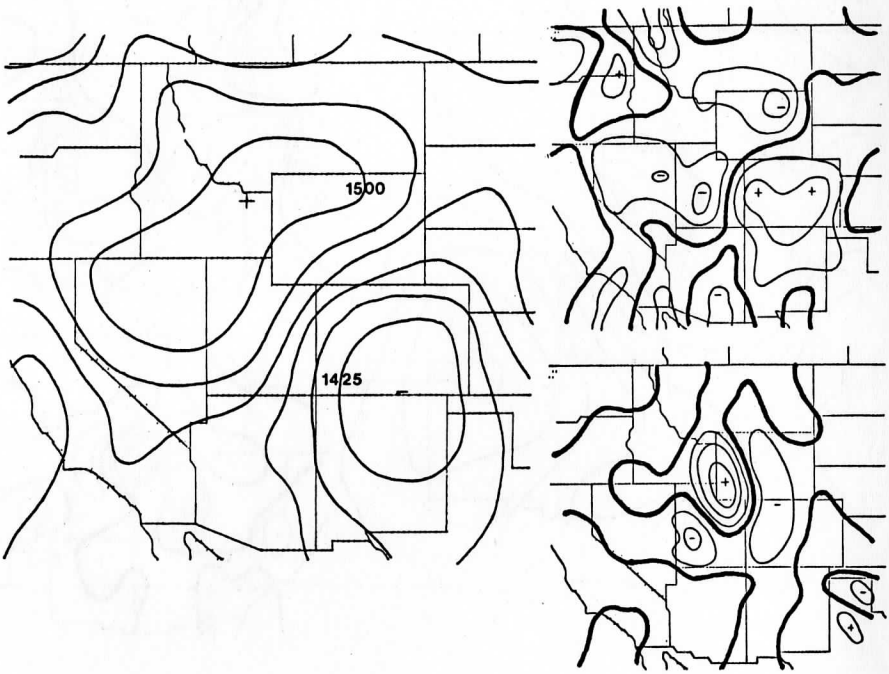

Figure V.17. Same as Figure V.11 for 12 GMT 15 April 1977 and 12-15 GMT 15 April 1977.

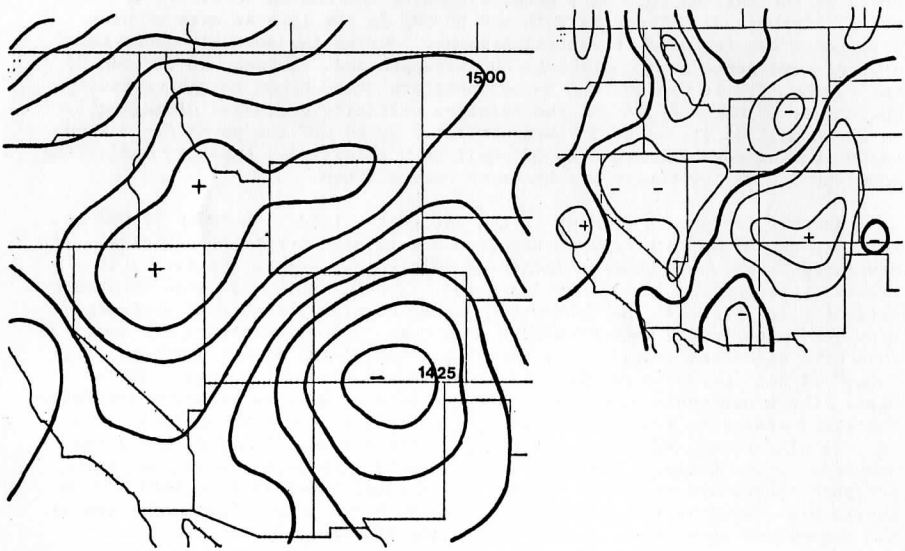

Figure V.18. Derived 850 mb height field and geostrophic relative vorticity (top right) for 15 GMT 15 April 1977. Contour intervals are the same as on Figure V.11.

correction type wind, are also equal.

Good qualitative agreement between divergence and local vorticity changes is seen in Figures V.11 through V.17. Strong divergence located in southwest Wyoming between 18 GMT and 21 GMT on 14 April 1977 suggested decreasing positive vorticity with time. Convergence existed generally to the east and south of the maximum vorticity area, signaling increasing vorticity in these areas. Between 21 GMT on the 14th and 00 GMT on the 15th an area of weak divergence was centered in central Arizona. During the next six hours this area of divergence moved northeast and strengthened. Between 03 GMT and 06 GMT on the 15th it was located in southeastern Utah, close to the vorticity maximum at 03 GMT. By 06 GMT the relative vorticity decreased dramatically to about half of its value 3 hours earlier. By 09 GMT the vorticity maximum had decreased more and the area of positive vorticity had expanded indicating that the 850 mb low center was becoming more diffuse.

Another feature is evident in the vorticity fields. Between 21 GMT on the 14th and 03 GMT on the 15th negative absolute geostrophic vorticity developed in northern Utah as indicated by strongly negative relative vorticity exceeding the local coriolis value. Usually this indicates incorrect data, but in this case the pronounced "nose" of high pressure in northern Utah was supported by data from many stations. Reduction errors are small in this area since the stations are normally close to the 850 mb surface. This "nose" of high pressure resulted in a very tight gradient across eastern Utah. The geostrophic wind shear produced strong negative relative vorticity. One might expect to find unbalanced motions such as inertial instabilities in this situation. With such strong gradients the accelerations are large compared to the Coriolis force and the underlying assumptions of quasi-geostrophic theory are no longer valid. It is significant that derived 850 mb charts are useful in identifying these areas, but a precise documentation of the associated ageostrophic winds are beyond the scope of this work.

VI. SUGGESTIONS FOR FORECAST APPLICATIONS AND FURTHER DEVELOPMENT

The major benefit of the derived 850 mb heights is that they can produce a pressure-gradient force much more representative over the elevated surface of the western United States than the sea-level pressure gradient. This in turn means that more accurate kinematic and dynamic fields can be derived from the pressure gradient.

Winds and wind forecasting are difficult over the western United States. Friction and local effects are so strong that the actual surface wind may seem to have little connection with the synoptic-scale pressure-gradient force. Many studies have been derived which use the difference in sea-level pressure between selected stations to forecast local wind and other variables. Such studies could be improved by using the more accurate pressure representation available from derived 850 mb heights.

Since the derived 850 mb height gradient is more representative of the

actual surface pressure gradient, it could be used to obtain a better first estimate of the surface wind. Once the height gradient is obtained other adjustments could be added to give a better estimate of local winds. First, since the actual earth's surface is rarely at 850 mb, the pressure-gradient force at 850 mb could be adjusted up or down via the thermal wind equation. The 850 mb potential temperature field would be used for this adjustment. Surface friction could then be added. This could be done by using a balanced Ekman spiral as mentioned at the end of Section IV or by other appropriate boundary layer methods. Thus a first estimate of the synoptic surface wind could be obtained from derived 850 mb fields. However, it should be noted that the agreement between these estimates and the observed wind may still not be very good. Local effects are often dominant in the western United States and must be accounted for before good agreement can be expected.

Because local effects are so important and the height of the earth's surface is so variable. The surface winds are often not representative of synoptic-scale dynamic processes. For example, the advection of scalar fields such as temperature or moisture by the observed surface winds over the western United States would probably not be representative of the actual synoptic-scale advections. The winds calculated from the derived 850 mb height field would be more representative of synoptic-scale processes and would be more helpful in diagnosing current weather. This same argument could be applied to vorticity, divergence, or deformation of the observed surface wind versus winds calculated from the derived 850 mb heights. These fields could be very useful in diagnostic work as will be mentioned subsequently.

Vorticity is very sensitive to the pressure field since it is the second spatial derivative of pressure. Slight changes in pressure are usually amplified in the vorticity pattern. Thus small perturbations barely detectable on a pressure map such as sea-level pressure are much more evident on a surface vorticity map. Small-scale upper-air features frequently produce only small fluctuations in surface-pressure fields. These fluctuations are noticeable in the vorticity patterns and can be tracked by using surface vorticity charts. Such features can become significant weather producers upon reaching areas favorable for cyclogenesis. A case in point is documented by the National Weather Service (1971) Central Region. The surface vorticity chart used in this case was produced from the Sangster geostrophic wind field discussed in Section I. Similar results should be expected from the derived 850 mb vorticity charts.

On a constant pressure surface the time rate of change of vorticity is related to the divergence times the absolute vorticity, ignoring friction and the tilting terms. For example a given divergence will produce twice the rate of vorticity change for an absolute vorticity of $20 \times 10^{-5}\ s^{-1}$ as compared to $10 \times 10^{-5}\ s^{-1}$. Thus 850 mb vorticity, in combination with the divergence field, provides an estimate of the short range change of vorticity (as mentioned already in the case study in Section V). This procedure may be useful in short range forecasting of low centers. An example of this potential application may be found in an informal study by the National

Weather Service (1975) Central Region.

A number of derived 850 mb fields are useful in frontal analysis. Potential temperature and geostrophic advection of potential temperature have already been mentioned in the case study in Section V. In addition the equivalent potential temperature (surface or derived 850 mb) has been shown to be very helpful in identifying different air masses over the western United States such as would be found at a frontal boundary (Mitchell, 1969). It could be readily calculated along with the other 850 mb fields.

Since the 850 mb surface is near the earth's surface over the western United States the vorticity pattern at the surface will be very similar to that at 850 mb. Theoretically the surface front coincides with the region of greatest cyclonic vorticity. This proved to be the general case in the examples studied; however, vorticity was not as powerful a delineator of frontal boundaries as the temperature related fields.

Deformation fields are rarely used today in routine analysis and forecasting. In combination with divergence they could be used to indicate frontogenesis/frontolysis. A frontgenetical formula is given in Saucier (1955, p. 365):

$$\text{Accumulation} = 1/2\left(\frac{\partial Q}{\partial n}\right)\left[\left|\text{def}_r \vec{V}\right| \cos 2\beta - \text{div } \vec{V}\right]$$

where Q is any scalar property, β is the angle between axis of dilation and Q lines, and n is the unit vector normal to Q lines pointing toward higher Q values. This formula shows that deformation and convergence both act to concentrate or relax gradients of scalar properties (e.g. temperature, moisture, etc.). Fronts somtimes can not be identified until they have existed for a number of hours. The frontogenetical function would allow the forecaster to anticipate their development.

Low level vertical motion may be inferred from derived 850 mb vorticity and divergence, assuming they are representative of those near the earth's surface. In the classical Ekman pumping case the frictional boundary layer produces a balanced ageostrophic wind component which has a maximum at the surface and decreases rapidly to the top of the boundary layer. This ageostrophic component produces convergence in areas of positive relative vorticity. Through continuity of mass considerations low level convergence cause upward vertical motion. Thus geostrophic vorticity with its frictionally induced convergence, as well as the convergence calculated from the frictionless 850 mb ageostrophic winds, may be used to indicate areas of upward vertical motion. This simple analysis may be further modified by including frictional effects on the isallobaric wind (Young, 1973) and the ageostrophic inertial-type wind (Mahrt, 1975). The net effect in these cases may be summarized as decreasing the vertical motion fields as estimated from frictionless theory.

Further adjustments could be incorporated to improve derived 850 mb

heights and temperatures. The key to better heights is a more accurate estimate of T_{mv}, the mean virtual temperature. There are three parts that make up T_{mv} estimates for the derived 850 mb chart, the surface temperature, the lapse rate, and the diurnal correction term.

The lapse rate assumed for all stations in this study was 1/2 the dry adiabatic lapse rate. While this seemed to work well for most of the stations, several had persistent inversion conditions, while a few had lapse conditions greater than 1/2 the dry adiabatic lapse rate. Instead of using just one assumed lapse rate and temperature correction, three would be better. Stations could be stratified into one of three lapse rate groups: normal (~5-7°C/km), strong (greater than 7°C/km), and weak (less than 5°C/km). Each one of these groups would have a temperature correction derived in a manner similar to that used in this study. This stratification could be accomplished a number of ways. For radiosonde observing stations below the 850 mb surface the process is straightforward. Mean lapse rates between the surface and 850 mb for morning and evening soundings would be calculated (potential use of the instantaneous observed vertical temperature profile is discussed later in this chapter). Suitable limits for each category would then be chosen. For stations where raob data is not available and stations above the 850 mb level the procedure would be more difficult. One approach might use the average difference between maximum and minimum temperatures. Stations that have persistent inversions should heat more rapidly during clear days since a smaller layer of air is being heated. This would have to be normalized for the amount of insolation available. This procedure assumes that a correlation exists between the maximum and minimum temperature spread and the vertical temperature profile in the boundary layer. This assumption could be tested against the raob stations where the vertical temperature profile is known. Another method for non-raob stations below the 850 mb level would involve collecting temperature data from aircraft flights and surrounding raob stations on the area.

In addition to stratifying stations according to lapse rate, the lapse rates should be varied at least 4 times a year to account for seasonal changes. New lapse rates and temperature corrections would be computed and the stations would be restratified.

The lapse rates and temperature corrections calculated by the above methods are designed to fit an average case. There may be times when the lapse rate is known to differ from the assumed lapse rate. For example, the presence of cumuliform clouds would imply at least an adiabatic lapse in the subcloud layer. Very poor visibility due to fog and haze might imply stable conditions in the boundary layer. In these cases the lapse rate could be adjusted to a more realistic value. Another example of this is the consistent error observed when a low at 850 mb was approaching raob stations below 850 mb. The computed heights were always higher than the raob heights, suggesting the lapse rate in the warmer air ahead of the low center. By adjusting the lapse rate in these special cases, better results would be obtained.

Radiosonde observed data could be incorporated at the available times to improve the derived 850 mb values. Raob data represents information in the vertical as well as the 850 mb level. T_{mv} could be calculated directly from raob data. A Cressman type analysis could be performed using the derived data as the initial guess and applying corrections calculated from raob data. These corrections would decrease with time until a new set of corrections could be calculated from a subsequent raob run.

Instead of using raob data as a correction to an assumed lapse rate, the observed vertical temperature profile could be the basis for calculating 850 mb heights. Raob data is available twice daily about 2-3 hours after the balloon release time. In order to use it for 12 hours (until the next raob), a correction as a function of time must be applied. This correction could be computed by using a boundary layer model. Changes in the vertical temperature profile predicted by the boundary layer model could be used directly or incorporated via a Model Output Statistics (MOS) approach (Glahn, et al., 1972). In the MOS approach, output from numerical models is used in a multiple stepwise regression equation to predict the desired parameter.

Editing of unrealistic results and recomputation is another method of improving the derived 850 mb fields. As mentioned in Section III unrealistic values of 850 mb height and potential temperature can result from abnormal surface temperatures, such as produced by strong radiational cooling over fresh snow. An error checking program similar to that used for heights could be applied to the potential temperature field. If a temperature fell outside of the prescribed range that datum could be edited out. A new 850 mb potential temperature would be calculated via a Cressman analysis scheme. The mean virtual temperature for the column, T_{mv}, would then be calculated by a prescribed function using the new 850 mb potential temperature, surface temperature, and the thickness of the layer. The function would be designed to give T_{mv} using an averaged vertical temperature profile for the given temperature difference between the surface and 850 mb.

Another method for improving derived 850 mb fields is to enlarge and improve the data base. At present AMOS stations are not decoded on the McIDAS system. Many of these stations are in areas where conventional data are lacking. Their incorporation would significantly improve the resolution in those areas. Most military stations were not available for use on the McIDAS system when this study was being done. Many military stations would duplicate civilian stations already available, but some are located in data sparse areas. The inclusion of these stations would further improve the resolution. Not all the stations with elevations above 715 m (see Figure V.3) should be used. Some stations are too high. For example Alamosa, Colorado at 2296 m would at times require more than 800 meters of reduction. The greater the reduction distance the greater the possible errors that may be introduced. While the choice of a limit is somewhat arbitrary, 700 m seems to be the highest value recommendable for the western United States. Most investigators recommend a maximum reduction distance of 600 m to 800 m. Elimination of these stations would decrease the chances for large errors.

Clearly, improvements can be made in the derived 850 mb system. Even so, the derived 850 mb fields give a much better approximation of the real surface synoptic fields than the reduced sea-level pressure map. In addition, the single 850 mb geopotential field is capable of giving many fields useful in diagnosis and short range forecasting. It is also capable of giving very good time and space resolution. Because only one field is involved, the derived 850 mb system is more convenient for representing the surface-pressure-gradient force over the western United States than the sigma (σ) coordinate system such as the Sangster chart. The 850 mb system does not require any smoothed representation of the earth's surface. It should be noted however that where the actual earth's surface can be well represented by a smoothed $\sigma = 1$ surface, the sigma system gives the most accurate results. This is the case for the area east of the Rocky Mountains in the United States.

REFERENCES

Bellamy, J.C., 1945: The Use of Pressure Altitude and Altimeter Corrections in Meteorology. J. of Meteor., 2, 1-79.

Bigelow, F.H., 1900-01: Report on the Barometry of the United States, Canada, and the West Indies. Report of the Chief of the Weather Bureau, Vol. II, Washington, D.C.

_____, 1940: The Circulation in Cyclones and Anticyclones with Precepts for Forecasting by Auxiliary Charts on the 3,500-foot and 10,000-foot Planes. Mon. Wea. Rev., 32, 212-216.

Cressman, G.P., 1959: An Operational Analysis System. Mon. Wea. Rev., 87, 367-374.

Ferrell, W., 1886: Report on Reduction of Barometric Pressure to Sea Level and Standard Gravity. Appendix 23 of the Annual Report of the Chief Signal Officer, U.S. War Dept., Washington, D.C.

Glahn, H.R., and D.A. Lowry, 1972: The Use of Model Output Statistics (MOS) in Objective Weather Forecasting. J. of Appl. Meteor., 11, 1203-1211.

Haltiner, G.J., 1971: Numerical Weather Prediction. New York, John Wiley & Sons, 317pp.

Harrison, L.P., 1957: Report on the Problem of "Reduction of Pressure." Report of the Working Group on Barometry to the World Meteorological Organization, Commission for Instruments and Methods of Observation (CIMO-II), Paris, 118pp.

_____, 1960: Climatic Atlases. Report to the 3rd Session of the Commission for Climatology of the W.M.O. London, 21pp.

_____, 1963: Manual of Barometry (WBAN). Government Printing Office, Washington, D.C.

_____, 1970: Reduction of Surface Pressure to Functions Useful in Analysis and Forecasting. Meteor. Monographs, 11, 121-136. (Note: comprehensive bibliography included.)

Jorgensen, D.L., A.F. Korte, and W.H. Klein, 1969: Charts Giving Station Precipitation in the Plateau States from 850- and 500-millibar Lows During Winter. Office of Systems Development, Techniques Development Laboratory Tech. Memo. 25, Silver Springs, MD. ESSA, Weather Bureau, 82pp. (Unpub. manuscript.)

List, R.J., 1968: Smithsonian Meteorological Tables, 6th edition, Washington, D.C., Smithsonian Institution, 527pp.

Little, D.M., and W.M. Vernon, 1934: Reduction of the Barometric Pressure over the Plateau to the 5,000 Foot Level. Mon. Wea. Rev., 62, 149-155.

Mahrt, L., 1975: The Influence of Momentum Advections on a Well-Mixed Layer. Quar. Jour. of the Royal Meteor. Soc., 101, 1-11.

Meisinger, C.L., 1922: The Preparation and Significance of Free-air Pressure Maps for the Central and Eastern United States. Mon. Wea. Rev., 50, 453-468.

National Weather Service, 1971: Some Rules for Frontal Wave Formation and Movement. Central Region Technical Attachment No. 71-18, Scientific Services Division, Kansas City, Missouri, 3pp. (Unpublished manuscript.)

_____, 1975: The Storm of January 10-11, 1975--Why so Intense? Central Region Technical Attachment No. 75-3, Scientific Services Division, Kansas City, Missouri, 5pp. (Unpublished manuscript.)

Phillips, N.A., 1957: A Coordinate System having Special Advantages for Numerical Forecasting. J. of Meteor., 14, 184-185.

Saucier, W.J., 1955: Principles of Meteorological Analysis, Chicago, University of Chicago Press, 438pp.

Sangster, W.E., 1960: A Method of Representing the Horizontal Pressure Force without Reduction of Station Pressures to Sea Level. J. of Meteor., 17, 166-176.

_____, 1967: Diurnal Surface Geostrophic Wind Variations over the Great Plains. Central Region Tech. Memo. 13, Kansas City, Missouri, ESSA, Weather Bureau, 16pp. (Unpublished manuscript.)

Snellman, L.W., 1977: Personal communication. As chief of the Scientific Services Division of the Western Region (headquarters Salt Lake City, Utah) it was Mr. Snellman's duty to determine the regional position on the question of discontinuing 850 mb synoptic reports.

World Meteorological Organization, 1964: Note on the Standardization of Pressure Reduction Methods in the International Network of Synoptic Stations. Tech. Note No. 61, WMO-No. 154. TP. 74, Geneva, Report of a Working Group of the Commission for Synoptic Meteorology, 40pp.

Young, J.A., 1973: A Theory for Isallobaric Air Flow in the Planetary Boundary Layer. J. Atmos. Sci., 30, 1584-1591.

_____, 1977: Class notes from Meteorology 611, Dynamics of Large Scale Motions. Dept. of Meteorology, University of Wisconsin-Madison.

APPENDIX 1: Use of the 1977 McIDAS Programs

In 1977, the software for the derived 850 mb chart was not part of the regular McIDAS software at the University of Wisconsin-Madison. It was considered experimental. Information concerning it was not found in the normal user's guide to McIDAS. This software was developed in collaboration with Mr. Tom Whittaker. It utilized many of the existing programs dealing with hourly surface observations (Service A), substituting derived 850 mb data for data reported on the Service A teletype circuit. The following description is written for 1977 users.

The first key-in, "ZZ", accesses the experimental 850 mb software. There are two basic routines, plotting and contouring. Contouring is specified by the three letter key-in "CON" immediately following "ZZ"; otherwise the program automatically defaults to the plotting routine. The next three letter key-in specifies the parameter to be plotted or contoured. Only two derived 850 mb parameters may be both plotted and contoured: the derived 850 mb height (HGT) and potential temperature (THA). The values for each available station are plotted at the appropriate location of the station on the map by the plotting routine. Other parameters such as wind (WND), potential temperature advection (AAD), vorticity (VOR), divergence (DIV), shearing deformation (DSH), and stretching deformation (DST) require computation of a gradient which means interpolating the derived data to grid points. This is done as part of the contouring program called up by the three letter key-in "CON" previously mentioned.

The next key-in is the date/time group. The date is the two digit day of the month; if it is less than 10, zero precedes the data (01, 02, etc.). The time is Greenwich meridian or international time (GMT). It is a four digit group. The first two digits are the hour, the last two are the minute; "00" is used following the hour to obtain the hourly report. In addition to

regular hourly reporting times, two other options are available via the date/time group: time averaging and time differencing. By specifying the minutes to be other than zero, an intermediate or time-averaged value of a parameter between the two adjacent hourly values is computed via linear interpolation. For example, if 1120 were the time key-in the value of any parameter would be one-third of the way between the 1100 and 1200 values.

In time differencing, the values of the given parameter for two specified hours (not necessarily adjacent) are computed and their difference is obtained. The date/time group specified first is subtracted from the second one. The two date/time key-ins (6 digits each) must be separated by the word "to". For instance the key-in "201100 to 201200" for the date/time group would calculate the one hour difference between 11 GMT and 12 GMT on the twentieth of the month in question. This technique is available for all parameters. This capability of time differencing is used for computing the isallobaric wind and its divergence. The height difference field for an appropriate time interval is used instead of the height field to calculate the isallobaric wind.

Time averaging for periods exceeding one hour is also possible. The same format as time differencing is used. The software is changed (4 cards are interchanged) so that the average is computed instead of the difference. This requires that the programmer interchange the appropriate cards and reload the entire software package into disc storage. The instances where use of time-averaged values may be advantageous have already been discussed in the body of the thesis.

The next key-in is used only when the contouring program is implemented. It specifies the interval to be used in contouring and the way the data are to be printed out. Normally this is a three digit group. With experimental software "ZZ" another digit precedes the usual three. It is used to distinguish between the geostrophic wind (0 or blank) and the inertial correction type wind (1). The next three digits are described in the McIDAS user's manual. The first of these three controls the type of output for the contouring program. Zero (0) or blank contours the field and prints maximum and minimum values at their map locations. Two (2) prints maximum and minimum values but does not contour. One (1) contours but does not print maximum or minimum values. Three (3) prints the grid point values. The final two digits are the contour interval. It ranges from 01 to 99. Leaving this group blank will cause the program to default to a predetermined value which depends upon the parameter requested.

The last four key-in groups control the output format of the line printer. They are described in the McIDAS user's manual. The first two specify the latitude and longitude of the northwest and southeast corners of the map background respectively. The backgrounds are mercator projections. The last two give the horizontal and vertical dimensions of the map. Since there is a maximum of 500 grid points for the contour program and it was decided to utilize one degree latitude/longitude spacing, the map background chosen was 50123 31099 10106 10058. The first two digits in the last two groups space

the printer horizontally from the left of the page and vertically from the top for the first line printed. The final three digits in the last two groups give horizontal and vertical size of the map. Rather than type these groups each time, frequently used map backgrounds can be specified by a single group of two or three letters. For example, maps centered on a state are specified using the two letter postal abbreviation. A special three letter code (XXX) was created for the map base used with the experimental 850 mb software. The following examples illustrate typical key-ins,

ZZ HGT 111500 to 111800 XXX.

The above command would cause the 3 hour height difference (or 3 hour time averaged heights) to be plotted at the respective stations.

ZZ CON VOR 111500 1050 XXX

This command would cause the vorticity of the ageostrophic inertial correction type wind to be contoured at an interval of 50 prescribed units (5×10^{-5} sec^{-1}), with maximum and minimum values printed at their locations.

LIST OF FIGURES

LIST OF TABLES

REPORTS AVAILABLE FROM

The University of Wisconsin Press *114 North Murray Street, Madison, Wisconsin 53715*

97024. Studies in Atmospheric Energetics Based on Aerospace Probings: Annual Report, 1966. 129 pages. 1967.

97026. Studies in Atmospheric Energetics Based on Aerospace Probings: Annual Report, 1968. 162 pages. 1969.

97027. Radiation Experiment in the Vicinity of Barbados: Final Report, NSF Grant Ga. 12603. 100 pages. 1970.

97028. The Study of Radiation in a Tropical Atmosphere: Final Report. 100 pages. 1970.

97029. The Educational and Social Uses of Communications Satellites: A Bibliography. 42 pages. 1970.

97030. Measurements from Satellite Platforms: Annual Scientific Report on NAS5-11542, 1968-69. 388 pages. 1970.

97031. A Pilot Study on the Application of Geosynchronous Meteorological Satellite Data to Very Short Range Terminal Forecasting. 113 pages. 1970.

97032. Studies of the Atmosphere Using Aerospace Probings: Annual Report 1969. 243 pages. 1970.

97033. Teleconferencing: A Bibliography. 42 pages. 1971.

97034. Legal and Political Aspects of Satellite Telecommunication: An Annotated Bibliography. 126 pages. 1971.

97035. Multidisciplinary Studies of the Social, Economic and Political Impact Resulting from Recent Advances in Satellite Meteorology: An Interim Report, Vol. 1. 459 pages. 1971.

97036. Multidisciplinary Studies of the Social, Economic and Political Impact Resulting from Recent Advances in Satellite Meteorology: An Interim Report, Vol. 2. 431 pages. 1971.

97037. Measurements from Satellite Platforms: Annual Scientific Report on NAS5-11542, 1969-70. 180 pages. 1971.

97038. Studies of the Atmosphere Using Aerospace Probings: Annual Report, 1970. 69 pages. 1971.

97041. Measurements from Satellite Platforms: Annual Scientific Report on NAS5-11542, 1970-71. 270 pages. 1972.

97042. Experiments in Medical Communications via the ATS-1 Satellite. 136 pages. 1972.

97043. Specifications for a Vertical Temperature and Moisture Sounder for the Synchronous Meteorological Satellites. 82 pages. 1972.

(continued from back cover)

97044. Scientific Requirements of Sea Surface Measurements for the GARP Tropical Experiment. 18 pages. 1972.

97045. Studies of the Atmosphere Using Aerospace Probings: Annual Report, 1971, Vol. II: Application Studies. 104 pages. 1972.

97046. Multidisciplinary Studies of the Social, Economic and Political Impact Resulting from Recent Advances in Satellite Meteorology: An Interim Report, Vol. 3. 252 pages. 1972.

97047. Multidisciplinary Studies of the Social, Economic and Political Impact Resulting from Recent Advances in Satellite Meteorology: An Interim Report, Vol. 4. 199 pages. 1972.

97048. Satellite Teleconferencing: An Annotated Bibliography. 130 pages. 1972.

97049. Measurements from Satellite Platforms: Annual Scientific Report on NAS5-11542, 1971-72. 228 pages. 1972.

97050. Synchronous Meteorological Satellite Sounder Specification: Final Report under NASA Contract NAS5-21607. 73 pages.

97051. Multidisciplinary Studies of the Social, Economic and Political Impact Resulting from Recent Advances in Satellite Meteorology: An Interim Report, Vol. 5. 290 pages. 1973.

97052. Measurements from Satellite Platforms: Annual Scientific Report on NAS5-21798, 1972-73. 331 pages. 1974.

97053. Visual Channel Data Analysis for Synchronous Meteorological Satellite: Scientific Report on NOAA/NESS Grant NG-26-72. 252 pages. 1974.

97054. Studies of the Atmosphere Using Aerospace Probes. Annual Report, 1973. 272 pages. 1974.

97055. Meteorological Measurements from Satellite Platforms: Annual Scientific Report on NAS5-21798, 1973-74. 97pages. 1975.

97056. Studies of the Atmosphere Using Aerospace Probes. Annual Report, 1974. 154 pages. 1975.

97057. Multidisciplinary Studies of the Social, Economic and Political Impact Resulting from Recent Advances in Satellite Meteorology: Final Report, Vol. 6. 100 pages.

97059. Studies of Soundings and Imaging Measurements. Final Scientific Report on NAS5-21798, 1974-1976. 273 pages. 1977.

97060. Studies of the Atmosphere Using Aerospace Probes. Annual Report, 1976. 238 pages.